Université de Montréal

# *Novel approaches to the synthesis and treatment of cathode materials for lithium-ion batteries*

par
Isadora Reis Rodrigues

Département de chimie
Faculté des arts et des sciences

Mémoire présenté à la Faculté des études supérieures
en vue de l'obtention du grade de
Maitrise (M.Sc)
en chimie

Juillet 2010

Université de Montréal
Faculté des arts et des sciences

Ce mémoire intitulé:

***Novel approaches to the synthesis and treatment of cathode materials for lithium-ion batteries***

Présenté par
Isadora Reis Rodrigues

a été évalué par le jury composé des personnes suivantes:

Président rapporteur: Pr. André L. Beauchamp (Université de Montréal)

Directeur de recherche: Pr. Dean MacNeil (Université de Montréal)

Membre du Jury: Pr. Dominic Rochefort (Université de Montréal)

# Résumé

Nous avons mis au point une approche novatrice pour la synthèse d'un matériau de cathode pour les piles lithium-ion basée sur la décomposition thermique de l'urée. Les hydroxydes de métal mixte ($Ni_xMn_xCo_{(1-2x)}(OH)_2$) ont été préparés ($x$ = 0.00 à 0.50) et subséquemment utilisés comme précurseurs à la préparation de l'oxyde de métal mixte ($LiNi_xMn_xCo_{(1-2x)}O_2$). Ces matériaux, ainsi que le phosphate de fer lithié ($LiFePO_4$), sont pressentis comme matériaux de cathode commerciaux pour la prochaine génération de piles lithium-ion. Nous avons également développé un nouveau traitement post-synthèse afin d'améliorer la morphologie des hydroxydes.

L'originalité de l'approche basée sur la décomposition thermique de l'urée réside dans l'utilisation inédite des hydroxydes comme précurseurs à la préparation d'oxydes de lithium mixtes par l'intermédiaire d'une technique de précipitation uniforme. De plus, nous proposons de nouvelles techniques de traitement s'adressant aux méthodes de synthèses traditionnelles. Les résultats obtenus par ces deux méthodes sont résumés dans deux articles soumis à des revues scientifiques.

Tous les matériaux produits lors de cette recherche ont été analysés par diffraction des rayons X (DRX), microscope électronique à balayage (MEB), analyse thermique gravimétrique (ATG) et ont été caractérisés électrochimiquement. La performance électrochimique (nombre de cycles vs capacité) des matériaux de cathode a été conduite en mode galvanostatique.

***Mots clés*** : Pile lithium-ion, matériau de cathode, nouveaux approches de synthèses et traitements des hydroxydes de métaux mixte et phosphate de fer lithié.

# Abstract

We have developed a novel approach to the synthesis of cathode materials for lithium-ion batteries, based on the thermal decomposition of urea. Mixed metal hydroxides ($Ni_xMn_xCo_{(1-2x)}(OH)_2$), $x$ = 0.00 to 0.50, were prepared and subsequently used as precursor for lithiated mixed metal oxide ($LiNi_xMn_xCo_{(1-2x)}O_2$). These materials along with lithium iron phosphate ($LiFePO_4$) are being considered as cathode materials for the next generation of lithium-ion batteries. We have also developed new post-synthetic treatments on the hydroxides in order to enhance the morphology, which would result in improved electrode properties.

The novelty of this thesis is that for the first time mixed metal hydroxides for use as precursors for lithium mixed oxides have been prepared via a uniform precipitation technique from solution. In addition, we have proposed new treatments techniques towards the more traditional synthesis method for mixed metal hydroxides. The results obtained from these two methods are summarized within two articles that were recently submitted to peer-reviewed journals.

Within this thesis, all materials were analyzed with X-ray diffraction (XRD), scanning electron microscopy (SEM), thermal gravimetric analysis (TGA) and electrochemical measurements. The electrochemical performance (capacity *vs* cycle number) of the cathode materials were tested galvanostatically.

***Keywords:*** Lithium-ion battery, cathode material, novel synthetic approaches and treatments for mixed metal hydroxides and lithium iron phosphate.

# Table of Contents:

**Résumé** ..... iii
**Abstract** ..... v
**Table of Contents** ..... vii
**List of Tables** ..... x
**List of Figures** ..... xi
**List of Abbreviations** ..... xvii
**Preface** ..... xix
**Acknowledgement** ..... xx

**Chapter 1** Introduction ..... 1
1.1 General Introduction ..... 1
1.1.1 Layered compounds ..... 9
1.1.2 Olivine compounds ..... 11
1.2 Motivation and Objectives ..... 12
1.3 References ..... 14

**Chapter 2** Experimental Procedures ..... 16
2.1 Synthesis and post-synthetic treatments ..... 16
2.1.1 Traditional co-precipitation of $Ni_xMn_xCo_{(1-2x)}(OH)_2$ and hydrothermal and micro-wave assisted hydrothermal post-synthetic treatments ..... 18
2.1.2 Co-precipitation of $Ni_xMn_xCo_{(1-2x)}(OH)_2$ based on the thermal decomposition of urea ..... 20
2.1.3 Synthesis of $LiNi_xMn_xCo_{(1-2x)}O_2$ ..... 22
2.1.4 Hydrothermal synthesis of $LiFePO_4$ ..... 23
2.2 Characterization ..... 25

2.2.1 Powder X-ray diffraction (PXRD) ..... 25
2.2.2 Scanning electron microscopy (SEM) ..... 30
2.2.3 Thermo-gravimetric analyses (TGA) ..... 32
2.2.4 Electrochemical analyses ..... 33
2.3 References ..... 38

**Chapter 3** Post-synthetic treatments on $Ni_xMn_xCo_{(1-2x)}(OH)_2$ for the preparation of lithium metal oxides ..... 40
Abstract ..... 40
3.1 Introduction ..... 42
3.2 Experimental ..... 44
3.2.1 Preparation ..... 44
3.2.2 Characterization ..... 46
3.3 Results and Discussion ..... 47
3.3.1 Mixed metal hydroxides ..... 47
3.3.2 Lithium mixed metal oxides ..... 59
3.4 Conclusion ..... 67
3.5 References ..... 68

**Chapter 4** A novel co-precipitation method towards the synthesis of $Ni_xMn_xCo_{(1-2x)}(OH)_2$ for the preparation of lithium metal oxides ..... 70
Abstract ..... 70
4.1 Introduction ..... 72
4.2 Experimental ..... 76
4.2.1 Preparation ..... 76
4.2.2 Characterization ..... 77
4.3 Results and Discussion ..... 79
4.3.1 Co-precipitation of mixed metal hydroxides based on the thermal decomposition of urea ..... 79
4.3.2 Lithium mixed metal oxides ..... 95
4.4 Conclusion ..... 104

4.5 References ..... 106

**Chapter 5** Synthesis of lithium iron phosphate based on the thermal decomposition of urea ..... 108

5.1 Introduction ..... 108

5.2 Results ..... 111

5.2.1 Hydrothermal synthesis of $LiFePO_4$ – as described in the literature ..... 111

5.2.2 Hydrothermal synthesis of $LiFePO_4$ – assisted by the thermal decomposition of urea ..... 112

5.2.3 "*in situ*" carbon coating attempt ..... 115

5.2.4 Electrochemical Analyses of $LiFePO_4$ ..... 118

5.3 Conclusion ..... 121

5.4 References ..... 122

**Chapter 6** Conclusion and Perspectives ..... 124

6.1 Conclusion ..... 124

6.2 Perspectives ..... 127

6.3 References ..... 129

**Appendix** ..... 130

Appendix A Rietveld analysis for $Ni_xMn_xCo_{(1-2x)}(OH)_2$ prepared by the traditional co-precipitation method and hydrothermal treated for 5 hours 130

Appendix B Rietveld analysis for $LiNi_xMn_xCo_{(1-2x)}O_2$ prepared from hydroxides synthesized using the traditional co-precipitation reaction and post-synthetic treatments ..... 133

Appendix C Rietveld analysis for $LiNi_xMn_xCo_{(1-2x)}O_2$ prepared from the hydroxide synthesized using the thermal decomposition of urea ..... 136

# List of Tables:

**Table 3.1.** Lattice parameters, unit cell volume and amount of oxyhydroxide phase present in $Ni_xMn_xCo_{(1-2x)}(OH)_2$ after post-synthetic hydrothermal treatment for 5 hours. ..... 55

**Table 3.2.** Lattice parameters and cell unit volume of $LiNi_xMn_xCo_{(1-2x)}O_2$, indexed using the R3m space group. ..... 61

**Table 4.1.** Amount (%) of nitrogen, carbon and hydrogen in samples prepared by hydrothermal precipitation. ..... 88

**Table 4.2.** Lattice parameters and cell unit volume of $LiNi_xMn_xCo_{(1-2x)}O_2$, indexed using the R3m space group. ..... 99

**Table 5.1.** EDX quantitative elemental analyses of both, black and green precipitates obtained during the synthesis of $LiFePO_4$ using iron gluconate precursor..... 118

**Table A.1.** Miller indexes for Bragg peaks for $Co(OH)_2$ and CoOOH..... 135

**Table A.2.** Miller indexes for Bragg peaks for $LiCoO_2$. ..... 135

# List of Figures:

**Figure 1.1.** Representation of a basic electrochemical cell during discharge. ....2

**Figure 1.2.** Representation of a commercial cylindrical lithium-ion battery [2]. 6

**Figure 1.3.** Representation of a typical lithium-ion battery during discharge [7]. .....7

**Figure 1.4.** Structure of (a) $LiCoO_2$ (layers of $CoO_6$ octahedral, in blue, with intercalated lithium in yellow) and (b) $LiFePO_4$ ($FeO_6$ octahedra, in red, $PO_4$ tetrahedra in purple and intercalated lithium in green) [5]...9

**Figure 2.1.** Hydrothermal autoclaves. Simple autoclave without any adapters (a) and with a few gas/pressure and stirring adapters (b). .....17

**Figure 2.2.** Micro-wave equipment and turntable used for the micro-wave assisted hydrothermal technique. .....18

**Figure 2.3.** Derivation of the Bragg's law.....25

**Figure 2.4.** Schematic representation of a powder X-ray diffractometer [12]. .27

**Figure 2.5.** Schematic representation and a photo of a scanning electron microscope [14].....31

**Figure 2.6.** Representation of a typical laboratory 2032 test battery (coin cell). .....34

**Figure 2.7.** Charge and discharge profiles for the two different current rates (5 and 30 mA $g^{-1}$) applied to the tests with $LiNi_xMn_xCo_{(1-2x)}O_2$. .....36

**Figure 3.1.** XRD profiles of $Ni_xMn_xCo_{(1-2x)}(OH)_2$. (bottom black line = as prepared by co-precipitation; middle red line = after 5 hours hydrothermal, top blue line = after microwave assisted post-synthetic hydrothermal treatment and the green lines in the x = 0.00 quadrant is a representation of the Bragg peaks, with indicated Miller indices, for $Co(OH)_2$ that can be used as a reference.....49

**Figure 3.2.** XRD profiles of $Ni_xMn_xCo_{(1-2x)}(OH)_2$ demonstrating the development of the $Ni_xMn_xCo_{(1-2x)}OOH$ structure after post-synthetic hydrothermal treatment for 24 hours. ..... 52

**Figure 3.3.** TGA measurements (15 °C/ min, dry air) for $Ni_xMn_xCo_{(1-2x)}(OH)_2$ as prepared by traditional co-precipitation (a) and after post-synthetic hydrothermal treatment (b). ..... 53

**Figure 3.4.** SEM images of $Ni_xMn_xCo_{(1-2x)}(OH)_2$ (x = 0.15) (a) as prepared by co-precipitation, (b) after hydrothermal and (c) after microwave assisted post-synthetic hydrothermal treatment. ..... 56

**Figure 3.5.** SEM images of $Ni_xMn_xCo_{(1-2x)}(OH)_2$ (x = 0.00) submitted to a) 5 hours and b) 24 hours of post-synthetic hydrothermal treatment.... 57

**Figure 3.6.** SEM images of $Ni_xMn_xCo_{(1-2x)}(OH)_2$ as prepared by co-precipitation for the indicated concentration of *x*. ..... 58

**Figure 3.7.** XRD profiles of $LiNi_xMn_xCo_{(1-2x)}O_2$. (bottom black line = precursor hydroxide as prepared by co-precipitation; middle red line = precursor after hydrothermal (5 hours), top blue line = after microwave assisted hydrothermal treatment and the green lines in the $x = 0.00$ quadrant is a representation of the Bragg peaks, with indicated Miller indices, for $LiCoO_2$ that can be used as a reference. ..... 60

**Figure 3.8.** SEM images of $LiNi_xMn_xCo_{(1-2x)}O_2$ ($x = 0.15$) synthesized from the hydroxide precursors (a) as prepared by co-precipitation, (b) after 5 hr hydrothermal and (c) after microwave assisted post-synthetic hydrothermal treatment. ..... 62

**Figure 3.9.** Capacity vs cycle number for $LiNi_xCo_{(1-2x)}Mn_xO_2$ charged to 4.2V. The hydroxides precursors were as-prepared by co-precipitation (▲red), after hydrothermal (x black) and after microwave assisted post-synthetic hydrothermal treatment (+ blue). The charge-discharge curves consist of 5 cycles at a rate of 5 mA $g^{-1}$ followed by 50 cycles at 30 mA $g^{-1}$. ..... 64

**Figure 3.10.** Capacity vs cycle number for $LiNi_xCo_{(1-2x)}Mn_xO_2$ charged to 4.5V. The hydroxides precursors were as-prepared by co-precipitation (▲red), after hydrothermal (x black) and after microwave assisted post-synthetic hydrothermal treatment (+ blue). The charge-discharge curves consist of 45 cycles at a rate of 30 mA $g^{-1}$. .....66

**Figure 4.1.** XRD profiles of $Ni_xMn_xCo_{(1-2x)}(OH)_2$, synthesis based on urea decomposition for the indicated value of x. (bottom black line = under hydrothermal conditions; middle red line = microwave assisted hydrothermal and top blue line = reflux). .....81

**Figure 4.2.** XRD profiles of $Ni_xMn_xCo_{(1-2x)}(OH)_2$ synthesized using the decomposition of urea under hydrothermal conditions for 24 hours. .....82

**Figure 4.3.** TGA measurements (15 °C/min) for $Ni_xMn_xCo_{(1-2x)}(OH)_2$ synthesized using the decomposition of urea via the hydrothermal method (top red line $x$ = 0.00; bottom blue line x = 0.50). .....84

**Figure 4.4.** XRD profiles of $Ni_xMn_xCo_{(1-2x)}(OH)_2$ synthesized using the decomposition of urea via hydrothermal conditions after heating to 500°C in He. .....84

**Figure 4.5.** TGA measurements (15 °C/min) for $Ni_xMn_xCo_{(1-2x)}(OH)_2$ synthesized using the decomposition of urea via the hydrothermal method (top red line); and synthesized by the traditional co-precipitation method (bottom blue line) ($x$ = 0.00). .....86

**Figure 4.6.** SEM images of $Ni_xMn_xCo_{(1-2x)}(OH)_2$ synthesized using the decomposition of urea via the hydrothermal method. .....89

**Figure 4.7.** SEM images of $Ni_xMn_xCo_{(1-2x)}(OH)_2$ synthesized using the decomposition of urea under microwave assisted hydrothermal conditions. .....90

**Figure 4.8.** SEM images of $Ni_xMn_xCo_{(1-2x)}(OH)_2$ synthesized using the decomposition of urea under reflux conditions. .....91

**Figure 4.9.** Comparison of particle size and morphology for $Ni_xMn_xCo_{(1-2x)}(OH)_2$. (a) Prepared under hydrothermal conditions;

(b) microwave assisted hydrothermal conditions and (c) reflux conditions. Left column scale bar of 5 μm and right column of 30 μm, $x = 0.30$. ..... 93

**Figure 4.10.** Photograph of the solutions containing $Ni_xMn_xCo_{(1-2x)}(OH)_2$ ($x$ = 0.00 to 0.50) prepared under reflux conditions without any atmospheric controls in a) and in (b) for $Ni_xMn_xCo_{(1-2x)}(OH)_2$ ($x$ = 0.30) synthesized using reflux conditions under a purge of argon... 95

**Figure 4.11.** XRD profiles of $LiNi_xMn_xCo_{(1-2x)}O_2$. (bottom black line = from precursor prepared under hydrothermal conditions; middle red line = from precursor prepared under microwave assisted hydrothermal conditions, top blue line = from precursor prepared under reflux conditions and the green lines in the $x = 0.00$ quadrant is a representation of the Bragg peaks, with indicated Miller indices, for $LiCoO_2$ that can be used as a reference. ..... 96

**Figure 4.12.** SEM images of $LiNi_xMn_xCo_{(1-2x)}O_2$ ($x = 0.30$) prepared with hydroxide precursors (a) prepared under hydrothermal conditions, (b) microwave assisted hydrothermal conditions and (c) reflux conditions. Left column scale bar of 5 μm and right column of 30 μm. ..... 100

**Figure 4.13.** Capacity vs cycle number for $LiNi_xMn_xCo_{(1-2x)}O_2$ ($x = 0.15$) charged to 4.2V. Comparison of different methods used to achieve the required temperature to decompose urea. Hydrothermal condition (□ black); microwave assisted hydrothermal (+ red) and reflux (x blue). The charge-discharge curves consist of 5 cycles at a rate of 5 mA $g^{-1}$ followed by 50 cycles at 30 mA $g^{-1}$. ..... 101

**Figure 4.14.** Comparison of the capacity vs cycle number for $LiNi_xMn_xCo_{(1-2x)}O_2$ charged to 4.2V with hydroxides precursors prepared from the co-precipitation under hydrothermal conditions for the decomposition of urea (● black) to hydroxides prepared using the traditional co-precipitation method (+ green). The charge-discharge

curves consist of 5 cycles at a rate of 5 mA $g^{-1}$ followed by 50 cycles at 30 mA $g^{-1}$ ..... 103

**Figure 5.1.** XRD profile of $LiFePO_4$ synthesized by the traditional hydrothermal method (red) and the green lines indicate the reference spectra of $LiFePO_4$ ..... 112

**Figure 5.2.** XRD profile of $LiFePO_4$ synthesized under hydrothermal conditions using the thermal decomposition of urea (blue), under micro-wave assisted hydrothermal condition (black) with the green lines indicating the reference spectra of $LiFePO_4$. ..... 113

**Figure 5.3.** SEM images of $LiFePO_4$ synthesized using the thermal decomposition of urea under hydrothermal conditions. ..... 114

**Figure 5.4.** XRD profile of $LiFePO_4$ synthesized using the thermal decomposition of urea and iron gluconate as precursor. ..... 116

**Figure 5.5.** SEM images of $LiFePO_4$ synthesized with iron gluconate. The black precipitate (a) and green precipitate (b). ..... 117

**Figure 5.6.** Measured capacity of $LiFePO_4$ synthesized using the thermal decomposition of urea, and iron gluconate. ..... 120

**Figure A.1.** Rietveld refinement for $Ni_xMn_xCo_{(1-2x)}(OH)_2$ ($x$ =0.00) obtained after the hydrothermal post-synthetic treatment for 5 hours. Observed intensities: blue line; calculated intensities: red line; blue vertical bars: angular positions of Bragg reflections for $Co(OH)_2$; black vertical bars : angular positions of Bragg reflections for CoOOH. 131

**Figure A.2.** Rietveld refinement plots for $LiNi_xMn_xCo_{1-2x}O_2$ ($x$ = 0.05): blue line for observed reflections, red line for calculated reflections based on the $LiCoO_2$ structure, grey line is the difference between the observed and the calculated reflections, and blue vertical lines are the Bragg positions for reference $LiCoO_2$. ..... 134

**Figure A.3.** Rietveld refinement plots for $LiNi_xMn_xCo_{(1-2x)}O_2$ ($x$ = 0.05): blue line for observed reflections, red line for calculated reflections based on the $LiCoO_2$ structure, grey line is the difference between the

observed and the calculated reflections, and blue vertical lines are the Bragg positions). ..... 137

# List of Abbreviations:

Ah - Ampere-hour

*a* - Crystallographic lattice constant

*c* - Crystallographic lattice constant

d - Separation of the planes of atoms in a crystal

*E* - Cell voltage

*e* - Electron charge

EC - Ethylene carbonate

EV - Electric vehicles

EDX - Energy dispersive X-ray spectroscopy

DEC - Diethyl carbonate

*F*- Faraday constant

$\Delta G$ - Gibbs free energy

*i* - Current

$LiCoO_2$ - Lithium cobalt oxide

$LiPF_6$ - Lithium hexafluorophosphate

$LiNi_xMn_xCo_{(1-2x)}O_2$ - Lithiated mixed metal oxide

$LiFePO_4$ - Lithium iron phosphate

n - Path length difference

$Ni_xMn_xCo_{(1-2x)}(OH)_2$ - Mixed metal hydroxide

$Ni_xMn_xCo_{(1-2x)}OOH$ - Mixed metal oxyhydroxide

NMP - n-methyl pyrroldinone

P - Power

PVDF - Polyvinylidene difluoride

$Q_T$ - Theoretical capacity

$Q_m$ - Measured capacity

Rb - Bragg factor

Rwp - Weighted profile factor

SEM - Scanning Electron Microscopy

TGA - Thermogravimetric Analysis

V - Voltage

$V$ - Crystallographic unit cell volume

x - Theoretical number of moles

$x$ - Stoichiometric indices

XRD - X-ray diffraction

Wh - Watt-hour

$\lambda$ - Wavelength

$\Theta$ - Incident angle

# Preface

This thesis consists of two chapters composed of articles submitted to peer-reviewed journals and one other chapter containing non published results. The articles were prepared by the author under supervision of Dr. MacNeil. The major experimental parts were performed by the author. Dr. Joseph Wontcheu, post-doctoral fellow in Dr. MacNeil's laboratory, aided with the analysis of X-ray diffraction data.

The above mentioned articles are:

Chapter 3: Post-synthetic treatments on $Ni_xMn_xCo_{(1-2x)}(OH)_2$ for the preparation of lithium metal oxides (submitted to Journal of Solid State Electrochemistry).

Chapter 4: A novel co-precipitation method towards the synthesis of $Ni_xMn_xCo_{(1-2x)}(OH)_2$ for the preparation of lithium metal oxides (submitted to Journal of Power Sources).

# Acknowledgement

I would first like to thank my supervisor, Dr. Dean MacNeil, who encouraged me during this work even during the more difficult moments. I feel very fortunate to have had the chance to work with him.

I would also like to thank every member of Dr. MacNeil's laboratory. I greatly enjoyed working with the entire team. Special thanks are due, in particular, to Serge Lavallée and Nathalie Ravet, who were there in the beginning of this work, great friends in addition to shearing their knowledge about lithium-ion battery electrochemistry with me. Thanks to Dr. Joseph Wontcheu who collaborated with me on the work presented here, especially the X-ray diffraction experiments, and who also contributed to the preparation of the articles in which we will publish our results. I would also like express my enormous gratitude to everybody from the administration of the University of Montréal chemistry department.

Finally, a special thanks to my family and friends who in same way, supported this experience.

# Chapter 1

# Introduction

## *1.1 General Introduction*

A battery is a group of interconnected electrochemical cells that converts stored chemical energy into electricity. A battery has two main functions: to act as a portable source of electric power and to store energy originating from an external source [1-2]. They are very complex devices that involve numerous aspects of science, such as chemistry and physics, tackling aspects such as thermodynamics, kinetics and transport phenomena. Consequently, the study of any battery system is a very challenging process [3].

Figure 1.1 represents a basic electrochemical cell. In a simplified way, a battery is composed of two electrodes: the cathode (or positive electrode), the anode (or negative electrode) and an electrolyte that spans the two electrodes. The cathode is the electrode associated with the reduction reaction, while the anode is the electrode associated with the oxidation reaction. The electrolyte provides ionic mobility between the two electrodes that are physically separated from one another [2]. Normally, the term battery is used to refer to a series of

interconnected electrochemical cells, but it is now commonly accepted as the designation of a single electrochemical cell [4].

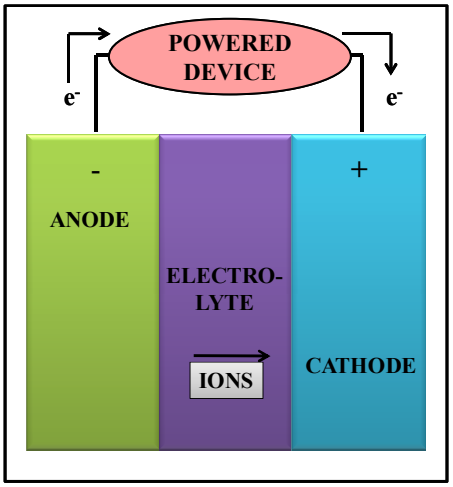


***Figure 1.1:*** *Representation of a basic electrochemical cell during discharge.*

Many chemical compounds can exist in more than one oxidation state. These compounds can either donate or accept electrons in a series of reduction-oxidation (redox) reactions. This electron transfer ability is ideal when they are employed as components for the electrodes of batteries [5]. An example of a redox reaction within a battery is:

$$A^{x+}_{(aq)} + B^{y+}_{(aq)} \rightarrow A^{(x+1)+}_{(aq)} + B^{(y-1)+}_{(aq)},$$

where, (Anode) $A^{x+}_{(aq)} - ne^- \rightarrow A^{(x+n)+}_{(aq)}$,

and (Cathode) $B^{y+}_{(aq)} + ne^- \rightarrow B^{(y-n)+}_{(aq)}$.

The first modern concept for a battery was reported by Alessandro Volta in the beginning of the 19th century [4]. Since then, the technological development in battery science has improved constantly, although at a much slower pace when compared to the electronic industry [4-6]. Currently, the increasing demand for mobile electronic products, the environmental concerns with greenhouse gas emissions and the impact of our dependence on foreign fossil fuels, has encouraged research into alternative and renewable energy sources. Batteries will be an integral part of any solution for these important technology hurdles [4-5, 7]. More recently, the transportation industry has spearheaded the need for better battery technologies in order to initiate a revolution in transportation methods, namely EVs (electric vehicles) [7-8].

The current battery market for high end portable electronics is based on a rechargeable lithium-ion technology, due to its large energy density, higher voltage and longer life time compared to other battery systems [4, 9]. In rechargeable (or secondary) batteries, the redox reactions within an electrode are reversible. At the end of discharge, when the stored energy inside the battery is depleted, the application of an external current in the opposite direction (by a charging system) can recharge the battery. In rechargeable batteries this charge/discharge process can be repeated numerous times without the destruction of the electrode material. Contrary to this, primary batteries do not partake in reversible oxidation-reduction reactions and thus cannot be recharged [1-3].

A very judicious choice of electrode material is necessary towards the success of a rechargeable battery. Each specific application requires an appropriate material selection process. The performance of a battery can be evaluated by numerous properties, such as its electrochemical specific capacity (mAh $g^{-1}$), cell voltage (V), energy density (WhK $g^{-1}$) and electrical power (WK $g^{-1}$). The electrochemical capacity of a battery is given by the number of electrons exchanged during the redox reaction and its molecular weight, while a batteries voltage is determined by the difference between the chemical potential of the two redox reactions (anode and the cathode) [2]. The theoretical capacity ($Q_T$) of a cell can be calculated as:

$$Q_T = x(nF) , \tag{1.1}$$

where x is the theoretical number of moles associated with the complete electrochemical reaction within the cell, $n$ is the number of electrons involved in the redox reaction and $F$ is Faraday's constant (96490 C $mol^{-1}$). In reality, the measured capacity ($Q_m$) of a cell is always lower than $Q_T$. The theoretical specific capacity of a cell is defined by the theoretical capacity divided by the total mass of the cell. The theoretical energy available for a reaction involving the transfer of 1 mol of electrons is given by:

$$\Delta G = - nFE_{cell} , \tag{1.2}$$

where $E_{cell}$ is the voltage of the cell. Energy ($\Delta G$) is commonly expressed by watt hour (W.h) in the electrochemical literature. The power (P) delivered by a battery during the electrochemical reaction is given by the product of the current delivered by the battery and its cell voltage:

$$P = iE_{cell}\,, \tag{1.3}$$

where $i$ is current flowing through the system. As mentioned above, rechargeable lithium-ion batteries are the most widely used power source in high-end portable electronics. They are one of the best options for the development and widespread use of electrical vehicles. This popularity is because lithium-ion batteries have a large energy density and high cell voltage compared to other electrochemical storage devices. In addition, numerous compounds have proven to be successful electrodes for use under specific conditions [5, 10]. The lithium-ion battery was first commercialized by SONY in 1991 using a lithiated cobalt oxide ($LiCoO_2$) as the cathode material and a carbon anode (Figure 1.2) [11]. The battery was assembled in a jellyroll fashion using a microporous polymer sheet as a separator between the electrodes to inhibit an electrochemical short circuit within the cell. The electrode roll was then placed into a metallic case and filled with electrolyte prior to sealing the case with a top [11].

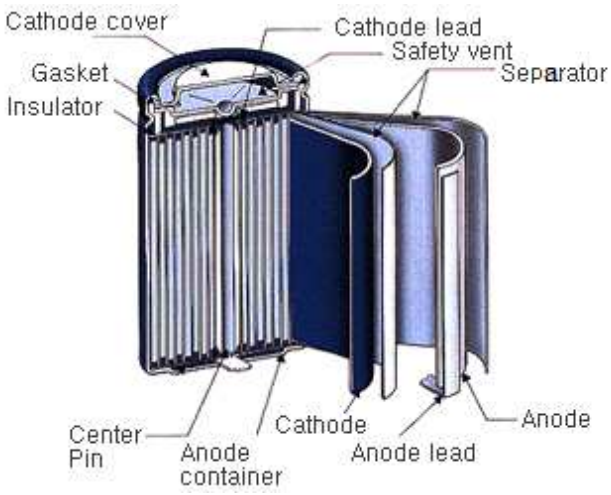


***Figure 1.2:*** *Representation of a commercial cylindrical lithium-ion battery [2].*

Today, the basic composition of a lithium ion battery has not changed dramatically from the original design. Typically, a common commercial lithium-ion battery is composed of a graphite anode, a $LiCoO_2$ cathode, an electrolyte composed of a lithium salt (ex.: $LiPF_6$) dissolved in an organic solvent and a polymeric separator. Figure 1.3 shows the operation of a typical lithium-ion battery. Upon discharge, the "so called" cathode material stores $Li^+$ cations from the electrolyte and electrons from the external circuit, resulting in the reduction of the oxidation state of the transition metal ions within the cathode material [5, 7]. The anode, during discharge, acts releasing $Li^+$ cations into the electrolyte and electrons to the external circuit. Lithium ions are transported by the electrolyte while electrons flow through the external circuit. The reactions of the anode and cathode electrodes are represented below:

(Full discharge reaction) $Li_xC_{6(s)} + Li_{(1-x)}CoO_2 \rightarrow C_6 + LiCoO_2$ ,

(Anode reaction) $Li_xC_{6\,(s)} \rightarrow xLi^+ + 6C_{(s)} + xe^-$ ,

(Cathode reaction) $xLi^+ + Li_{(1-x)}CoO_2 + xe^- \rightarrow LiCoO_2$ .

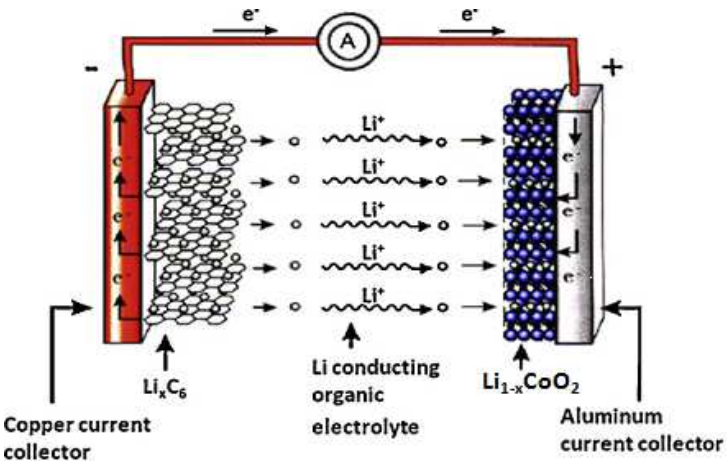


***Figure 1.3:*** *Representation of a typical lithium-ion battery during discharge [from 7].*

On charge the reaction shown above are reversed and the necessary energy for the reaction comes from the external charger. Whittingham [5] has summarized the general requirements for successful use of a cathode material in rechargeable lithium batteries. These are highlighted as followed:

- the material must be composed of a reducible/oxidizable ion;
- the material must be thermally and chemically stable;
- the material must be environmentally benign and obtained at an affordable cost;
- the material must have good ionic and electronic conductivity;

- the material must react reversibly with lithium;
- and the material must present high voltage, capacity and energy density.

Intercalation compounds are structures that do not undergo a dramatic structural change upon the insertion of a guest species. Therefore they represent the ideal type of material for use as an electrode material in rechargeable batteries. As lithium is continuously inserted and removed from the structure, the host will only see a small change of its structure, which should provide long life to the host for the numerous electrochemical reactions in which they will partake during its life time [5]. The research and commercialization of cathode materials for lithium-ion batteries have focused essentially on two classes of intercalation materials. The first are layered compounds, exemplified by $LiTiS_2$, $LiCoO_2$, and more recently $LiMn_xNi_xCo_{(1-2x)}O_2$ (Figure 1.4a). While compounds within the second class have a more open structure and are exemplified by $MnO_2$, vanadium oxides and more recently $LiFePO_4$ (Figure 1.4b) [5]. In the study presented here, we will be concerned with the preparation of two cathode materials from these groups; namely $LiFePO_4$ and $LiMn_xNi_xCo_{(1-2x)}O_2$.

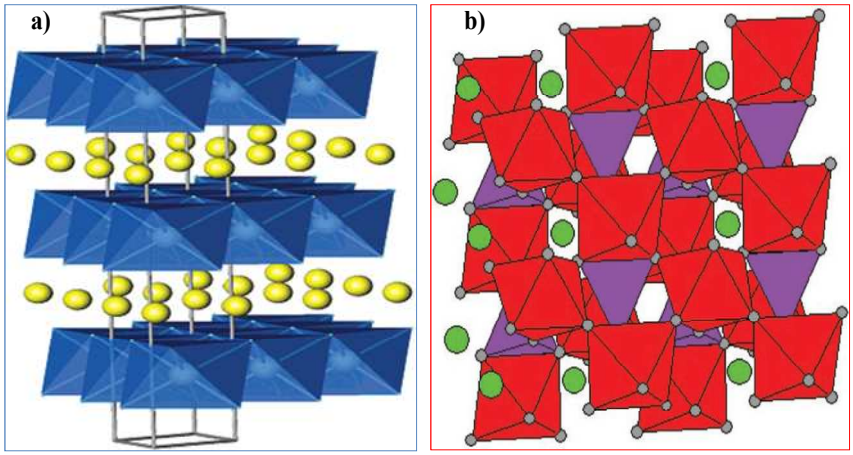


***Figure 1.4:*** *Structure of (a) $LiCoO_2$ (layers of $CoO_6$ octahedral, in blue, with intercalated lithium in yellow) and (b) $LiFePO_4$ ($FeO_6$ octahedra, in red, $PO_4$ tetrahedra in purple and intercalated lithium in green) [from 5].*

### 1.1.1 Layered compounds

$LiCoO_2$ has been the most widely used cathode material for rechargeable lithium-ion batteries due to its ease of fabrication, high energy density and excellent cycle life. Nonetheless, it presents elevated production costs due to the use of expensive cobalt metal, in addition, a number of incidents have raised concerns about its safety [12-14]. Several alternatives have been reported, such as the partial replacement of cobalt by nickel and/or manganese. These $LiNi_xMn_xCo_{(1-2x)}O_2$ material, as with $LiCoO_2$, have a hexagonal structure ($\alpha$-$NaFeO_2$), indexed on the $R\bar{3}m$ crystallographic space group. They can be regarded as a substitution of $Ni^{2+}$ and $Mn^{4+}$ into the $Co^{3+}$ position [15]. In 2001 the groups of Ohzuku [15] and Dahn [16] demonstrated that $LiNi_xMn_xCo_{(1-2x)}O_2$

was capable of delivering a stable capacity of ~ 160 mAh $g^{-1}$ under a current density of 40 mAh $g^{-1}$. Generally, it is cycled between the fully lithiated discharge state (~ 3.0 V *vs* $Li/Li^+$) and a partially delithiated charge state (~ 4.2 V vs $Li/Li^+$). The performance of these materials is dependent upon their structure, composition, synthesis method and voltage [17-20]. Mixed metal hydroxides, $Ni_xMn_xCo_{(1-2x)}(OH)_2$, are typically used as the precursors in the preparation of $LiNi_xMn_xCo_{(1-2x)}O_2$. These hydroxides are traditionally synthesized through a co-precipitation method that consists of precipitating a mixture of metal salts rapidly within a basic solution [16, 21]. The hydroxides are subsequently oxidized by air in the presence of a lithium salt at elevated temperatures to form the electrochemical active lithium metal oxide. The traditional co-precipitation method usually leads to a material with a small particle size. Morphology and particle size have a large effect on the performance of these cathode materials, as they are important parameters towards the creation of dense electrodes [18]. These properties are strongly affected by the nature of the hydroxide precursor. In spite of numerous works, $LiNi_xMn_xCo_{(1-2x)}O_2$ still requires further investigation in order to improve electrochemical performance, as well as its thermal and chemical stability.

### 1.1.2 Olivine compounds

Since its discovery as an electrode material in 1997, much attention has been paid to lithium iron phosphate ($LiFePO_4$) for the replacement of $LiCoO_2$ as electrode material in commercial Li-ion batteries [22]. One of the main advantages for $LiFePO_4$ is that it is a natural mineral (triphylite) composed of elements that are abundant, inexpensive and environmentally benign. The electrochemical active $LiFePO_4$ presents an orthorhombic structure based on the *Pnma* crystallographic space group with $FeO_6$ octhaedra and $PO_4$ tetrahedra [22]. This structure provides a one-dimensional tunnel where $Li^+$ can migrate. The discharge potential of $LiFePO_4$ is ~ 3.5 V (vs $Li/Li^+$) providing a specific theoretical capacity of 170 mAh $g^{-1}$ [5, 22-24]. A major issue toward the development of $LiFePO_4$ is its low electronic conductivity (~ $10^{-9}$ S/cm) at room temperature. The low electronic conductivity limits the ability of the material to deliver high capacity at elevated discharge rates. Ravet *et al.* have demonstrated that a surface coating of a conductive carbon layer on $LiFePO_4$ can significantly improve the electrochemical performance increasing the conductivity of the material [25].

## *1.2 Motivation and Objectives*

In this master's thesis, we were interested in investigating novel synthetic approaches and treatments for the preparation of cathode materials used in lithium-ion batteries. The main results are grouped in two articles that are presented in chapter 3 and 4 and a chapter containing unpublished data. The first article describes two new post-synthetic treatments to enhance the particle size of mixed metal hydroxides (precursors for the electrochemical active lithiated mixed metal oxides). These treatments led to an increase in the tap density of the material and this should lead to an electrode with higher density. This is an important issue to commercial lithium-ion battery manufacturers since it leads to batteries high higher energy density. In addition, this is the first time that a post-synthetic treatment in solution has been shown as traditionally, the treatments on the hydroxides are performed after isolation and drying of the product. These approach leads to a simplification of the manufacturing process which could bring about savings to the manufacturing costs of lithium-ion batteries.

The second article describes a novel synthetic approach to the precipitation of mixed metal hydroxides based on the thermal decomposition of urea. The decomposition of urea creates the required basic chemical

environment for the precipitation of hydroxides. Traditionally the synthesis of mixed metal hydroxides is carried out at room temperature. The synthesis shown here is at higher temperatures, which allow for a more homogenous precipitation method and the possibility of increasing the particle density of mixed metal hydroxides. Finally, chapter 5 reports on the results obtained with the synthesis of lithium iron phosphate using the thermal decomposition of urea that was introduced in chapter 4.

The specific objectives of this thesis were:

- to develop a novel synthetic approach that can be used for the preparation of lithium iron phosphate and mixed metal hydroxides,

- to develop different post-synthetic treatments to enhance the properties of hydroxides;

- to characterize $LiFePO_4$, mixed metal hydroxides and oxides materials with X-ray diffraction, scanning electron microscopy (SEM), thermal and other chemical analysis tools such as thermogravimetry (TGA) and elemental analysis;

- and to evaluate $LiFePO_4$ and $LiNi_xMn_xCo_{(1-2x)}O_2$ materials as cathode materials in lithium-ion batteries by electrochemical analysis.

## *1.3 References:*


**1.** Winter, M.; Brodd, R. J. *Chem. Rev*. **2004,** 104, 4245.

**2.** Vincent, C. A.; Scrosati, B. *Modern Batteries* **1997**, John Wiley & Sons Inc., New York.

**3.** Linden, D. *Handbook of Batteries*. McGraw-Hill, Inc.: New York, **1995**.

**4.** Palacin, M. R. *Chem. Soc. Rev.* **2009,** 38, 2565.

**5.** Whittingham, M. S. *Chem. Rev.* **2004,** 104, 4271.

**6.** Armand, M.; Tarascon, J.-M. *Nature* **2008**, 451, 452.

**7.** Scrosati, B.; Garche, J. *J. Power Sources* **2001,** 195, 2419.

**8.** Li, H.; Wang, Z.; Chen, L.; Huang, X. *Adv. Mater.* **2009**, 21, 4593.

**9.** Kang, K.; Meng, Y. S.; Bréger, J.; Grey, C. P., Ceder, G. *Science* **2006**, 311, 977.

**10.** Goodenough, J. B.; Kim, Y. *Chem. Mater.* **2010**, 22, 587.

**11.** Nagaura, T.; Tozawa, K. *Prog. Batteries Solar Cells* **1990**, 9, 209.

**12.** Amatucci, G. G.; Tarascon, J.-M.; Klein, L., C. *Solid State lonics* **1996,** 83, 167.

**13.** Numata, K.; Sakaki, C.; Yamanaka, S. *Chem. Lett.* **1997**, 26, 725.

**14.** Liu, Z.; Yu, A.; Lee, J.Y. *J Power Sources* **1999**, 81-82, 416.

**15.** Ohzuku, T.; Makimura, Y. *Chem. Lett.* **2001**, 30, 744.

**16.** Lu, Z.; MacNeil, D. D.; Dahn, J. R. *Electrochem. Solid State Lett.* **2001**, *4*, A191.

**17.** Jouanneau, S.; Eberman, K. W.; Krause, L. J.; Dahn, J. R. *J. Electrochem. Soc.* **2003,** 150, A1637.

**18.** Barkhouse, D. A. R.; Dahn, J. R. *J. Electrochem. Soc* **2005**, 152, A746.

**19.** Zhao, X.; Zhou, F.; Dahn, J. R. *J. Electrochem. Soc.* **2008,** 155, A642.

**20.** van Bommel, A.; Dahn, J. R. *J. Electrochem. Soc*. **2009,** 156, A362.

**21.** Lu, Z.; MacNeil, D. D.; Dahn, J. R. *Electrochem. Solid-State Lett.* **2001,** 12, A200.

**22.** Padhi, A. K.; Nanjundaswamy, K. S.; Goodenough, J. B. *J. Electrochem. Soc.* **1997**, 144, 1188.

**23.** Zaghib, K.; Striebel, K.; Guerfi, A.; Shim, J.; Armand, M.; Gauthier, M. *Electrochim. Acta* **2004**, 50, 263.

**24.** Whittingham, M. S.; Song, Y.; Lutta, S.; Zavalij, P. Y.; Chernova, N. A. *J. Mater.Chem.* **2005**, 15, 3362.

**25.** Ravet, N.; Chouinard, Y.; Magnan, J.-F.; Besner, S.; Gauthier, M.; Armand, M. *J. Power Sources* **2001**, 97-98, 503.

# Chapter 2

# Experimental Procedures

## *2.1 Synthesis and post-synthetic treatments*

The experimental work of this thesis concentrated on the synthesis of cathode material for lithium-ion batteries using a hydrothermal synthetic method. The hydrothermal synthetic method uses an aqueous solution of dissolved precursors and elevated temperature/pressure for the preparation of crystalline materials [1]. This method is common throughout geology as most minerals within the earth's crust are grown under hydrothermal conditions; triphylite (composed mainly of $LiFePO_4$) is an example. Here, we used the hydrothermal method as a post-synthetic treatment on mixed metal hydroxides obtained by the traditional co-precipitation method (chapter 3) as well as to the synthesis of mixed metal hydroxides (chapter 4) and $LiFePO_4$ (chapter 5). Figure 2.1 shows two different types of autoclaves used for the hydrothermal synthesis. The auto-clave in Figure 2.1a is a simplified model and the one in Figure 2.1b is a more sophisticated auto-clave equipped with pressure display and inlets to control the atmosphere inside the container.

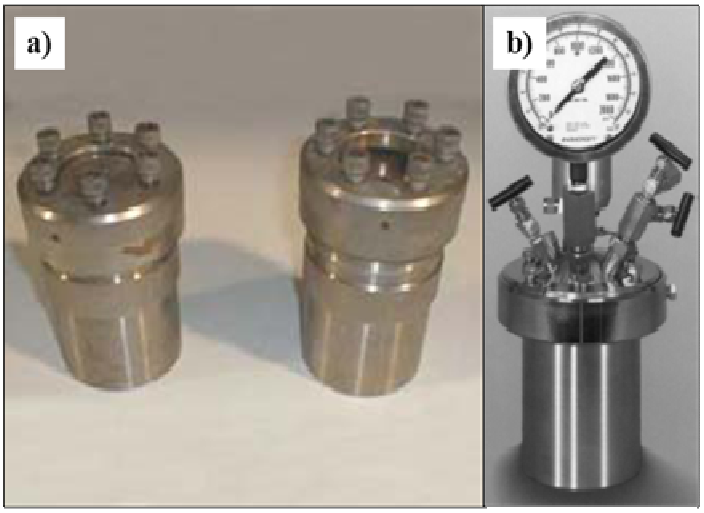


***Figure 2.1:*** *Hydrothermal autoclaves. Simple autoclave without any adapters (a) and with a few gas/pressure and stirring adapters (b).*

During the course of this thesis a micro-wave assisted hydrothermal method was also investigated for the synthesis and post-synthetic treatments. The microwave assisted method would significantly reduce the reaction time required, which would provide a significant amount of energy savings to the synthesis. Figure 2.2 shows the micro-wave equipment used during this investigation [2].


***Figure 2.2:*** *Micro-wave equipment and turntable used for the micro-wave assisted hydrothermal technique.*

### 2.1.1 Traditional co-precipitation of $Ni_xMn_xCo_{(1-2x)}(OH)_2$ and hydrothermal and micro-wave assisted hydrothermal post-synthetic treatments

As mentioned in the chapter 1, mixed metal oxides have been successfully used as a cathode material in lithium-ion batteries. Mixed metal hydroxides are the typically precursors in the synthesis of these oxides. The hydroxides are traditionally prepared by a co-precipitation method that leads to a material with a small particle size. Generally hydroxides with a small particle size tend to generate oxides with low tap density and thus electrodes of low density. In the literature multiple strategies have been reported to increase the particle size and density of these hydroxides [3-7]. Here, we proposed two

different post-synthetic heat treatments with the goal of increasing the particle size of mixed metal hydroxides and ultimately increase the performance of the oxides prepared with these treated hydroxides. Chapter 3 of this thesis will report in detail these post-synthetic treatments.

The synthesis of mixed metal hydroxides ($Ni_xMn_xCo_{(1-2x)}(OH)_2$; $x$ = 0.00, 0.05, 0.15, 0.30, 0.45 and 0.50), were performed through a co-precipitation method that consists of precipitating a mixture of metal salts within a basic solution [8]. Nitrate salts of Co, Ni and Mn were chosen as the metal sources ($Co(NO_3)_2.6H_2O$ (98%), $Ni(NO_3)_2.6H_2O$ (98%), $Mn(NO_3)_2.6H_2O$ (98%)) while $LiOH.H_2O$ (98%) (Aldrich) was used to create the alkaline medium for the precipitation. All solutions were prepared in distilled and degassed water. A solution containing the mixed metal nitrates with the desired stoichiometries (0.4 M) was slowly dropped into a stirred basic solution of LiOH (1.2 M) using a pump delivering the metal solution at ~ 3 mL/min. During the precipitation the atmosphere was controlled with Ar to prevent the oxidation of the precipitating hydroxides. After delivering the metal solution and rinsing with water to ensure complete delivery of all metal salts, three different post-synthetic routes were developed. In the first route the hydroxides were isolated directly from the co-precipitation after rinsing with distilled water and these samples were used as standard hydroxides for the study of the post-synthetic treatments. The second route consisted of a post-synthetic hydrothermal treatment in which the aqueous solution containing the hydroxides was transferred into a Teflon container and

placed within a sealed digestive vessel (Parr). The vessel was then placed in an oven at 180 °C for 5 or 24 hours. In the third route a microwave assisted hydrothermal treatment was applied. Here, the solution was sealed in closed Teflon liners, which were placed in a turntable for uniform heating within a microwave digestion system (MARS5, CEM). The system operated at a frequency of 2.45 GHz and a power of 1200 W. The temperature of the microwave was ramped rapidly to 180 °C and kept under these hydrothermal conditions for 15 min. In all cases the precipitate after treatment was rinsed several times with distilled water and dried overnight under dry air. Micro-wave assisted hydrothermal experiments were performed at the Laboratory of Combinatory Chemistry within the Université de Montréal.

### 2.1.2 Co-precipitation of $Ni_xMn_xCo_{(1-2x)}(OH)_2$ based on the thermal decomposition of urea

With the same goal of increasing the particle size of the mixed metal hydroxides, a novel precipitation approach was developed. This novel precipitation method was based on the thermal decomposition of urea. As urea decomposes the pH of its solution increases and it results in the precipitation of the hydroxides from solution. The precipitation of hydroxides from urea decomposition takes place from a solution containing metal salts at temperatures

higher than 90 °C. Chapter 4 reports in detail the precipitation of mixed metal hydroxides with the thermal decomposition of urea.

The same series of hydroxides mentioned in section 2.1.1 ($Ni_xMn_xCo_{(1-2x)}(OH)_2$; $x$ = 0.00, 0.05, 0.15, 0.30, 0.45 and 0.50) were prepared using $Co(NO_3)_2.6H_2O$ (98%), $Ni(NO_3)_2.6H_2O$ (98%), $Mn(NO_3)_2.6H_2O$ (98%) and the alkaline medium was obtained with the thermal decomposition of urea ($NH_2CONH_2$ Aldrich). All solutions were prepared in distilled and degassed water. An aqueous solution containing the mixed metal salts with the desired stoichiometry (0.4 M) and $NH_2CONH_2$ (1.2 M) was prepared and stirred for several minutes. The initial pH value was ~ 5. Three different routes were developed to achieve the temperature for the thermal decomposition of urea and subsequent precipitation of the hydroxides. The first route consisted of a hydrothermal treatment in which the aqueous solution of the metal salts and urea was transferred into a Teflon container and placed within a sealed digestive vessel (Parr). The vessel was then placed in an oven at 180 °C for 5 hours. In the second route a microwave assisted hydrothermal treatment was applied. Here, the solution was sealed in closed Teflon liners, which were placed in a turntable for uniform heating within a microwave digestion system (MARS5, CEM). The system operated at a frequency of 2.45 GHz and a power of 1200 W. The temperature of the microwave was ramped rapidly to 180 °C and kept under these hydrothermal conditions for 15 min. For the third route the aqueous solution was heated under reflux conditions at 100 °C for 5h. The pH at the end

of all of these reactions was ~ 7. A traditional co-precipitation reaction was also prepared for comparison by following the methods described in section 2.1.1. In all cases the precipitate was rinsed several times with distilled water and dried overnight under dry air.

### 2.1.3 Synthesis of $LiNi_xMn_xCo_{(1-2x)}O_2$

The mixed metal hydroxides prepared in sections 2.1.1 and 2.1.2 were used in the synthesis of the lithiated mixed metal oxides. As already mentioned these oxides are electrochemical active and can be used as cathode materials in lithium-ion batteries.

Final oxides ($LiNi_xMn_xCo_{(1-2x)}O_2$; $x$ = 0.00, 0.05, 0.15, 0.30, 0.45 and 0.50), were prepared by mixing the precursors hydroxides with an excess (3%) amount of LiOH ($LiOH.H_2O$, 98% Aldrich). The oxidation of the hydroxides was performed in two different heating steps. Initially, a uniform mixture of the hydroxides with LiOH was pelletized and heated at 500 °C for 3 h in air to eliminate all sample's humidity. The pellet was grounded, pelletized again and heated at 900 °C for 3 h in air. In the second heating step, the oxidation of the hydroxide into oxide, by the presence of the atmospheric $O_2$, take place and we have the formation of lithiated mixed metal oxides. Both heating steps are followed by a quench cooling (between large copper plates). A fast cooling is

necessary to stabilize the high temperature structure of the obtained oxide and thus ensuring that all metal ions are locked into the ideal layered structure.

### 2.1.4 Hydrothermal synthesis of $LiFePO_4$

During the course of this thesis, we synthesized lithium iron phosphate ($LiFePO_4$) and these samples were tested as cathode material for lithium ion batteries. A hydrothermal method was used for their synthesis using precursors never before tested in the literature. Chapter 5 will report in detail the hydrothermal synthesis of $LiFePO_4$ used in the thesis.

$LiFePO_4$ was prepared using iron sulfate ($FeSO_4.7H_2O$) (98%) or iron gluconate ($OHCH_2[CH(OH)]_4CO_2)_2Fe.2H_2O$) as iron sources. Lithium hydroxide ($LiOH.H_2O$) or lithium dihydrogen phosphate, ($LiH_2PO_4$) as lithium sources and phosphoric acid, $H_3PO_4$ (98%) was used (when needed) as the phosphate source. When $LiH_2PO_4$ was the lithium source, solutions also contained urea ($NH_2CONH_2$) to initiate the precipitation. All solutions were prepared using distilled water. In a standard experiment, a 3:1:1 ratio of Li:Fe:P ($LiOH:FeSO_4:H_3PO_4$) was used at a concentration of 22 g/L in water using ascorbic acid as a reducing agent for iron [9-10]. The auto-clave (125 mL Parr reactor) was filled with 90 mL of the solution, sealed and then heated at 180 °C for 5 hours. The synthesis of $LiFePO_4$ based on the thermal decomposition of

urea was performed by modifying the standard hydrothermal synthetic conditions using a 20% excess of urea with respect to iron and $LiH_2PO_4$ instead of LiOH. $LiH_2PO_4$, $FeSO_4$ and $NH_2CONH_2$, in a molar ratio of 1:1:1.2, were combined in water and heated to 180 °C for 5 hours. For both synthetic methods the resultant precipitate was isolated and washed with a large amount of water, followed by drying under vacuum for 3 hours. The micro-wave assisted hydrothermal method was also used to determine the effect that a different heating method and reaction time would have on the obtained $LiFePO_4$. The same solutions, as described previously, were used in the microwave reaction but the samples were sealed in closed Teflon liners, which were placed in a turntable for uniform heating within a microwave digestion system (MARS5, CEM). The system operated at a frequency of 2.45 GHz and a power of 1200 W. The temperature of the microwave was initially ramped rapidly to 180 °C and kept under these hydrothermal conditions for 15 min. The precipitate was washed and dried as before.

$LiFePO_4$ has a very low electronic conductivity and to overcome this difficulty as well as to maximize the electrochemical performance of the $LiFePO_4$ a carbon coating is necessary. The formation of a carbon coating, consisted of adding an aqueous solution containing 5% of β-lactose to the as-synthesized $LiFePO_4$ followed by the evaporation of the solvent overnight. The resultant powder was then heated at 700 °C for 3 hours under an $N_2$ atmosphere to decompose the lactose into a conductive carbonaceous material.

## *2.2 Characterization*

### 2.2.1 Powder X-ray diffraction (PXRD)

In 1912, Max von Laue suggested that crystalline substances act as three-dimensional diffraction gratings for x-ray since they have wavelengths similar to the spacing of atomic planes in a crystal. If we consider a plane of atoms as a mirror, and a crystal as a stack of these atomic planes with a separation of length d (Figure 2.3), the path-length difference of the two rays can be described as:

$$AB + BC = 2d \sin\theta \,, \tag{2.1}$$

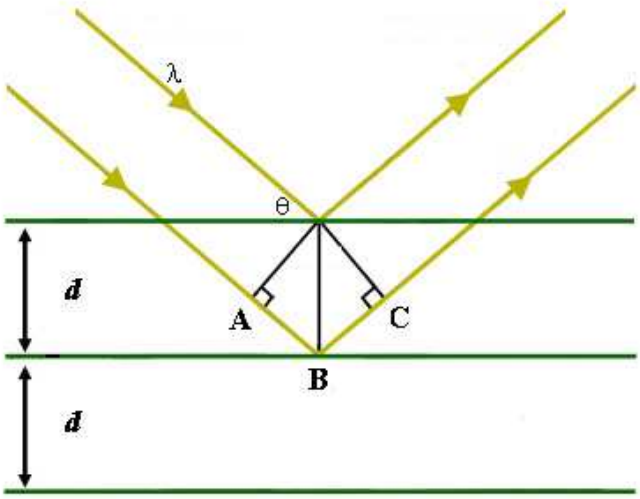


***Figure 2.3:*** *Derivation of the Bragg's law.*

where θ is the incident angle, AB and BC are the length between point A and B and between point B and C, respectively. When the path-length is an integral multiple of wavelengths, λ, (AB + BC = nλ), the reflected waves are in phase and interfere constructively. Thus constructive interference will be observed when Bragg law ($n\lambda = 2d\sin\theta$; where n = 1, 2, 3…) is respected [11]. Finally, diffraction is observed when the angle θ satisfies Bragg's law. By scanning the sample through a range of 2θ angles, all possible diffraction directions of the lattice should be attained due to the random orientation of the powdered material. Figure 2.4 shows a schematic representation of a powder X-ray diffractometer. The diffractometer consists of: the X-rays source or the X-ray tube; optics elements for the incident beam, that will condition the beam before it is focussed on the sample; a goniometer that holds and moves the sample stage, various optics, and a detector that will count the X-rays diffracted by the sample.

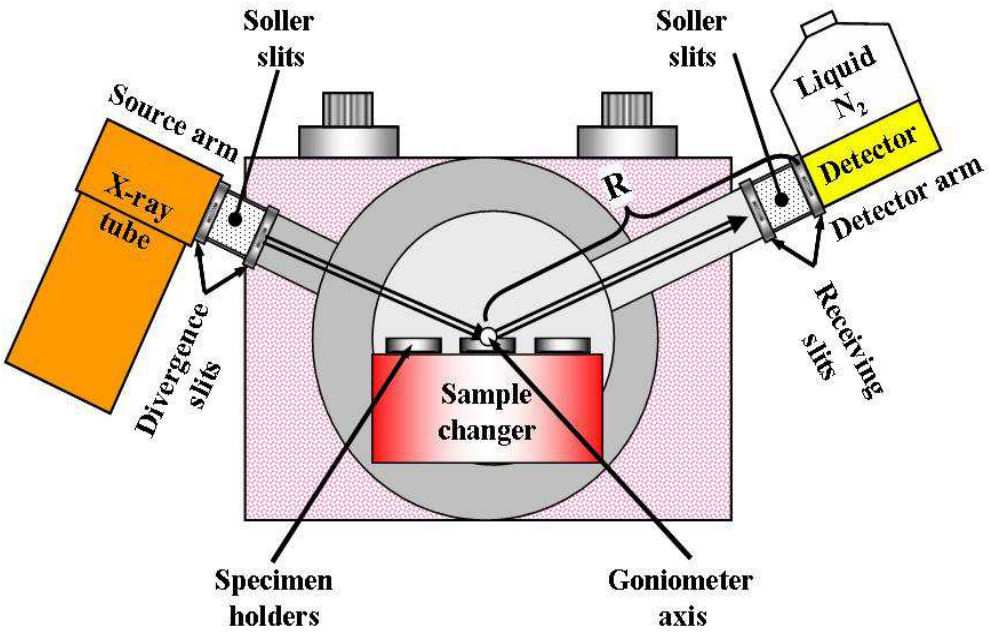


***Figure 2.4:*** *Schematic representation of a powder X-ray diffractometer [12].*

The crystalline phase of the samples and unit cell parameters were characterized by powder X-ray diffraction (XRD, Bruker D8 Advance) using Cu Kα radiation, the scan was performed with a step size of 0.025° and step time of 15 s in the diffraction angle range of 2 θ from 15 to 60 or 80° (where, 2 θ is the sum of the angles between the X-ray source and the sample and the sample and the detector). For mixed metal hydroxides and oxides the region of interest is between the diffraction angle of 15 and 60°, since the main Bragg diffraction peaks for these samples occur in this region. For $LiFePO_4$ the main Bragg peaks that will characterize the sample appear between a 2θ of 15 to 80° (the diffraction peaks of a compound can only be observed at angles (2θ) in which the Bragg's law is respected for a specific crystalline structure, this is the reason

they are called Bragg peaks). Typical sample preparation involved thorough grinding of the sample using a pestle and an agate mortar. When necessary, structural refinement was achieved by the Rietveld refinement method.

**Rietveld refinement**

The single crystal X-ray diffraction is a highly accurate technique for the determination of the atomic structure of solid compounds. In a single crystal X-ray diffraction the whole crystal is diffracted as the diffractometer operate in a three dimensional position. However, the production of single crystals is not a simple task for many materials. As a result, powder X-ray diffraction is a very important technique. In powder diffraction only a small fraction of the crystals (powder may contains many crystals) are correctly oriented to diffract at one time and the diffractometer is one dimensional (see Figure 2.4). The diffraction pattern from polycrystalline powders can be described as a one-dimensional projection of the three-dimensional diffraction data that result in partial or complete overlapping of some diffraction peaks. The Rietveld method is used to resolve the overlap of peaks [12].

In the Rietveld method of analysis, the powder diffraction data of the crystal structure is refined by fitting the observed diffraction pattern to a calculated diffraction pattern. The diffraction pattern of a compound can be

calculated when the space group symmetry, unit cell dimensions, type of atoms, relative coordinates of atoms in the unit cell, atomic site occupancies and the atomic displacement parameters are known [13]. The fitting is the most accurate procedure resulting in observed peak positions, full widths at half maximum, and integrated intensities of individual Bragg reflections. It is based on the minimization of the difference between observed and calculated diffraction patterns using a non-linear least squares technique. The refinement is achieved in two steps, the pattern matching and full Rietveld. Lattice parameters are refined during the pattern matching. The refinement continues by taking into account a structural hypothesis, then the relative atomic coordinates of each atom in the compound are introduced, the site occupation factor, the temperature coefficient (isotropic and anisotropic), while setting an initially lattice parameters values to those refined at the pattern matching. At the end of the refinement all these parameters are refined once. The agreement between experimental and calculated diffractograms for the hypothesis of the structural consideration is judged by the reliability factors: the weighted profile factor ($R_{WP}$) (measures the similarity between the calculated and experimental diffraction patterns) and the Bragg factor ($R_B$) (measures the agreement between the intensities of a calculated diffraction pattern of a compound and those measured experimentally).

The structure of the mixed metal hydroxides and oxides (reported in chapter 3 and 4) of this thesis has been determined from the refinement of the diffraction patterns of the X-rays by Rietveld method. More detailed examples are shown in the Appendixes A, B and C. All X-ray diffraction experiments

within this thesis were performed at the X-Ray Diffraction Laboratory of the chemistry department of Université de Montréal.

### 2.2.2 Scanning electron microscopy (SEM)

SEM is an analytical technique that can give information on the morphology and chemical composition of a sample. In this technique, a focalized electrons beam of high energy is used. Figure 2.5 shows a schematic representation and a photo of a scanning electron microscope. In the left side of this figure, we can see the microscope column, sample chamber, and vacuum system and in the right side the computer, monitor, and controls of the instrument. The “electron gun” is the source of the electrons beam. The condenser lenses control the diameter and focus of the beam. The electrons beam focused on the sample is either absorbed or scattered, from this interaction between the sample and electrons, a signal is generated, detected and electronically processed to produce an image. The electron beam is scanned over the entire surface of the sample. The resultant image contains information about the sample's surface morphology [11, 14-15].

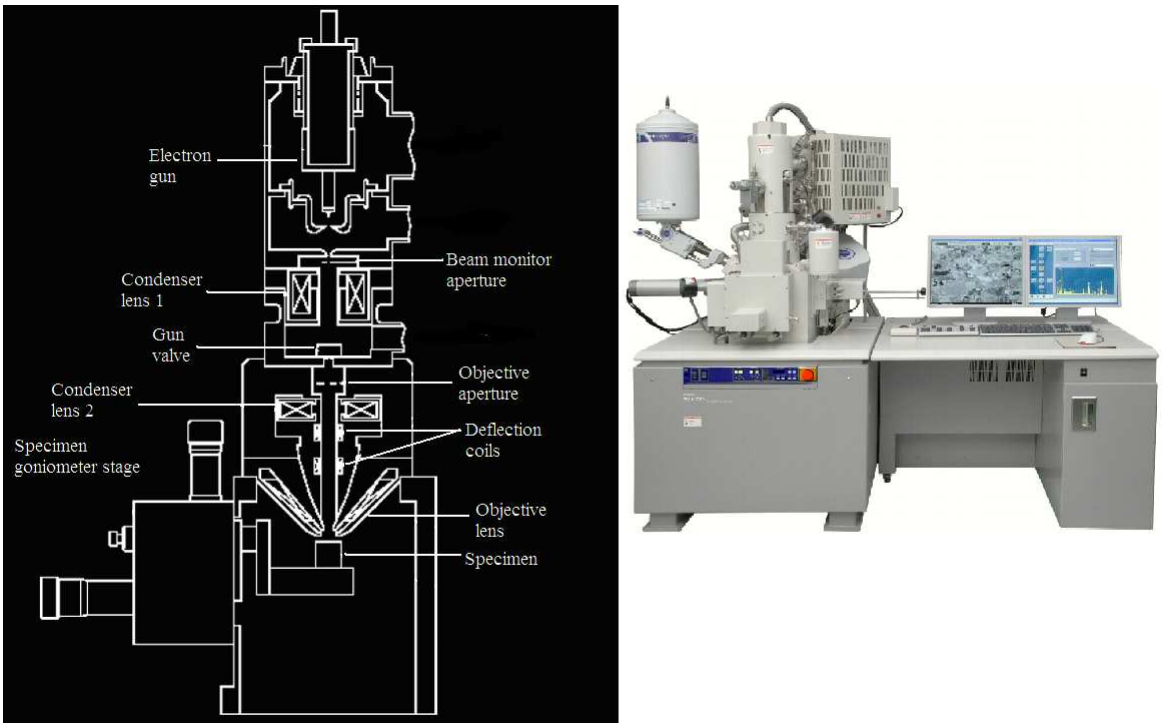


***Figure 2.5:*** *Schematic representation and a photo of a scanning electron microscope [14].*

The bulk of the SEM data of this thesis was collected on a Hitachi S-4300 microscope and the elemental quantitative composition analysis was done in a microscope equipped with an energy dispersive X-ray spectrometer (EDX) (EAS 1108, Fisions Instruments). EDX is an elemental quantitative micro analytical technique that uses the characteristic spectrum of X-rays emitted by a sample after excitation of high-energy electrons to obtain information about the elemental composition. When samples are bombarded by the electrons beam of the SEM, electrons are ejected from the atoms on the sample's surface. A resulting electron vacancy will be filled by an electron from a higher energy shell in the atom, and an X-ray will be emitted to balance the energy difference

between these two electrons. The EDX detector measures the emitted X-rays versus their energy. The energy of the X-ray is characteristic of the element from which it was emitted. A spectrum of the energy versus relative counts of the detected X-rays is obtained can be evaluated for qualitative and quantitative analysis of the elements present in the sample surface [11, 14-15]. Operating conditions on our microscope were 10 kV with a working distance of around 15mm. Experiments were performed at the Laboratory of Micro Fabrication of the École Polytechnique de Montréal.

### 2.2.3 Thermo-gravimetric analyses (TGA)

TGA is a technique that determines the changes in a sample's weight in relation to the temperature and time, while a sample is subjected to a controlled temperature ramp program. Generally this technique can be very useful to investigate the thermal stability of a material, or to investigate its behavior in different atmospheres. In a typical TGA analysis, the sample under study is placed in a small inert crucible, which is attached to a microbalance of high precision within a furnace. The analysis is performed by gradually increasing the temperature of the furnace and the change in the sample weight is recorded. In this thesis, the technique was performed to evaluate the behavior of mixed metal hydroxides exposed to dry air (comparison between samples prepared by the traditional co-precipitation method and after hydrothermal post-synthetic

treatment) as well as to estimate the amount of intercalated water and/or ions into the hydroxides samples (prepared by the thermal decomposition of urea). The measurements were performed under a flowing He or dry air gas with a TA Instrument thermogravimetric analyser (SDT600) at 15 °C/min from room temperature to 500 °C. A typical experiment used about 20-50 mg of sample for analysis.

### 2.2.4 Electrochemical analyses

$LiFePO_4$ and $LiNi_xMn_xCo_{(1-2x)}O_2$ were being prepared for testing as cathode materials in lithium-ion batteries. The electrochemical evaluations of these samples, consisted of combining the active material ($LiFePO_4$ or $LiNi_xMn_xCo_{(1-2x)}O_2$) with 10% of a conductive carbon (Super-P Li, Timcal), and 10% polyvinylidene difluoride (PVDF) (Aldrich), 5.5% in N-methylpyrroldinone (NMP) (Aldrich) with an excess of NMP added to make a slurry. The slurry (with 80% of active material) was then deposited on a carbon coated Al foil (used as current collector during the electrochemical tests) using a doctor blade. The solution of PVDF was used as a binder so that the electroactive material would maintain connection to the current collect over repeated charge/discharge cycles. The carbon was used to ensure that each active particle in the electrode would be connected electrochemically to the current collector. The slurry was then dried at 70 °C and electrodes 13 mm in

diameter were cut for cell assembly in a standard laboratory test battery (2032 coin-cell hardware (Hohsen), where 2032 signifies dimension of 20 mm in diameter and height of 32 mm) (Figure 2.6) using a single lithium metal foil as both counter and reference electrode and a Celgard 2200 as the separator between the two electrodes. Cells were assembled in an argon-filled glove box using 1M of $LiPF_6$ salt dissolved in a mixture of solvents (ethylene carbonate (EC)/ diethyl carbonate (DEC) (3:1 by vol)) as electrolyte (UBE).

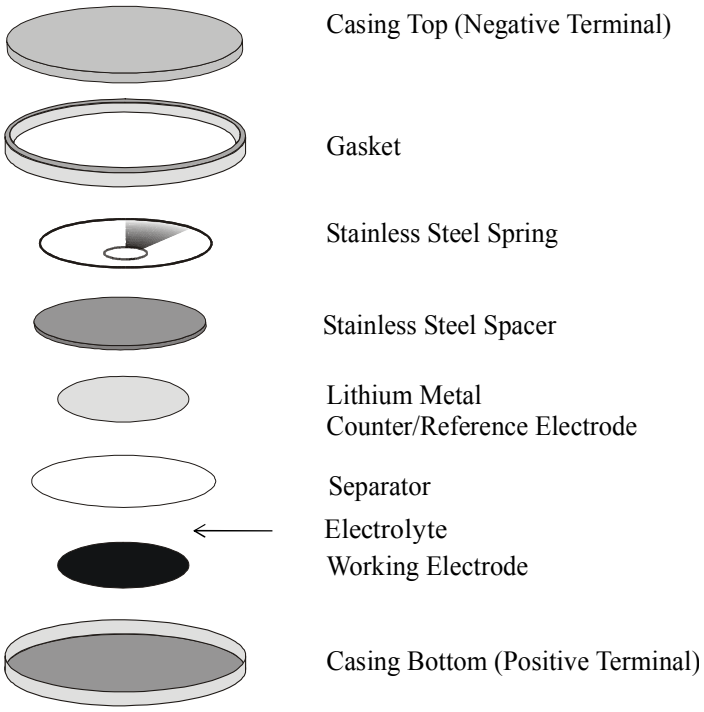


***Figure 2.6:*** *Representation of a typical laboratory 2032 test battery (coin cell).*

The electrochemical evaluations of the $LiNi_xMn_xCo_{(1-2x)}O_2$ samples were performed by charging and discharging the cells between 2.2 and 4.2 V. The

voltage window of the test was chosen based on the voltage of the redox couples ($Ni^{3+/4+}$, $Mn^{3+/4+}$, $Co^{3+/4+}$) *vs* $Li/Li^{+}$. This was approximately 4 V. To obtain higher capacities from $LiNi_xMn_xCo_{(1-2x)}O_2$, tests with a higher cutoff voltage were performed, as this would oxidize the higher stability metal. Two different current rates were used for our electrochemical evaluations. In the beginning of the tests, the current was 5 mA $g^{-1}$ (applied current of 5 mA per 1 g of $LiNi_xMn_xCo_{(1-2x)}O_2$) and this was subsequently increased to 30 mA $g^{-1}$. Figure 2.7 shows the profile of time *vs* potential obtained with the two different current rates used. The smaller current rate provide quasi-equilibrium conditions which would lead to optimal test conditions and values as high as possible for capacity. Higher current rates allow faster charge and discharge cycles such that it is possible to evaluate the stability of the material over a shorter period of time or an extended cycle life. Here, the cycle life is the total number of cycles of charge and discharge that the material can perform before the capacity falls to values that are no longer useful. All mixed metal oxides samples were tested at 30°C on a BT-2000 electrochemical station (Arbin).

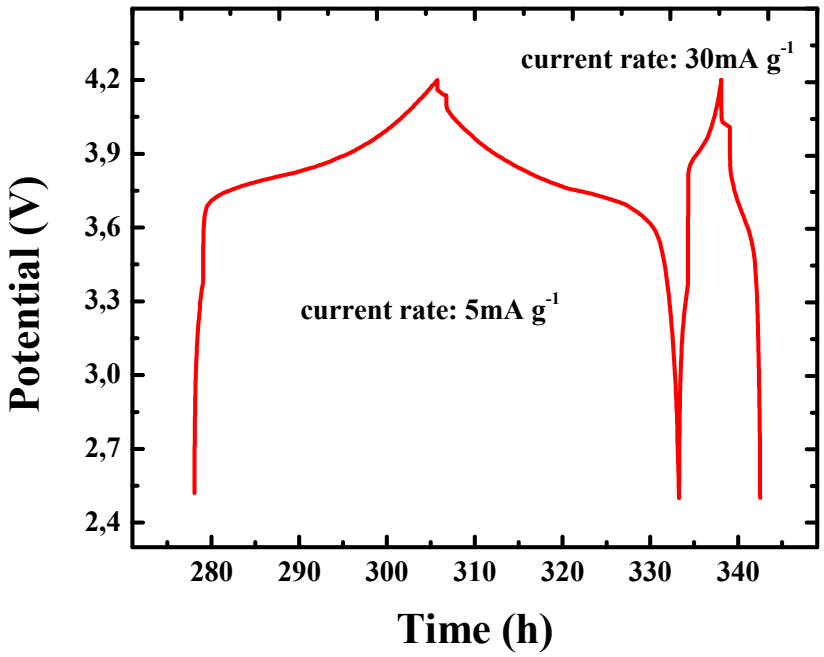


***Figure 2.7**: Charge and discharge profiles for the two different current rates (5 and 30 mA $g^{-1}$) applied to the tests with $LiNi_xMn_xCo_{(1-2x)}O_2$.*

When $LiFePO_4$ was used as the cathode material in the electrochemical tests, the cells were charged and discharged between 2.2 and 4.0 V (redox voltage $Fe^{2+}/Fe^{3+}$ *vs* $Li/Li^+$ of ~ 3.4V) at a current rate of 14 mA $g^{-1}$. The current rate was chosen to theoretically perform a complete cycle of charge/discharge over 24 hours. All tests performed with $LiFePO_4$ were done on a VMP station (Biologic, France) at room temperature.

The results can be expressed in a number of ways. One method is to express the amount of extracted (charge) or inserted (discharge) electron during the lifetime of the experiment. The number of electrons extracted/inserted is mathematically converted into capacity. The capacity is generally expressed in mAh $g^{-1}$, where an ampere (A) is a unit for the amount of electricity current flowing through a circuit. One ampere is the same as one coulomb (C) of electric charge (where one electron = 1,60 x $10^{-19}$ C) flowing past any point per second, 1 mAh $g^{-1}$ is equal to a current of one ampere flowing for one hour per grams of the active material in the electrode been tested (here the cathode).

## *2.3 References:*


**1.** Byrappa, K.; Yoshimura, M. *Handbook of hydrothermal technology* **2001**, William Andrew Publishing, New York.

**2.** CEM Corporation, *MARS Operation Manuel* **2004**.

**3.** Jouanneau, S.; Eberman, K. W.; Krause, L. J.; Dahn, J. R. *J. Electrochem. Soc.* **2003**, 150, A1637.

**4.** Barkhouse, D. A. R.; Dahn, J. R. *J. Electrochem. Soc.* **2005**, 152, A746.

**5.** Yabuuchi N, Koyama N, Ohzuku T. *J. Electrochem. Soc.* **2005**, 152, A1434.

**6.** Zhao, X.; Zhou, F.; Dahn, J. R. *J. Electrochem. Soc.* **2008**, 155, A642.

**7.** van Bommel, A.; Dahn, J. R. *J. Electrochem. Soc.* **2009**, 156, A362.

**8.** Lu, Z.; MacNeil, D. D.; Dahn, J. R. *Electrochem. Solid-State Lett.* **2001**, 12, A200.

**9.** Franger, S.; Le Cras, F.; Bourbon, C.; Rouault, H. *J. Power Sources* **2003**, 119–121, 252.

**10.** Ellis, B.; Wang, H. K.; Makahnouk, W. R. M.; Nazar, L. F. *J. Mater. Chem.* **2007**, 17, 3248.

**11.** Atkins, P. W.; De Paula J. Physical Chemistry, 2nd Ed., **2004**, De Boeck, Bruxelle.

**12.** Chen, J. *The hydrothermal synthesis and characterization of olivine compounds for the electrochemical applications*; Binghamton, graduate school of Binghamton University, **2001**.

**13.** Abinati, A.; Willis T. M.; *J. Appl. Cryst.* **1982**, 15, 374.

**14.** Hafner, B. *Scanning Electron Microscopy Primer*; University of Minnesota, **2007.**

**15.** Perrin, M. *Microscopie électronique à balayage et microanalyse*; C.M.E.B.A. Université de Rennes 1.

# Chapter 3

# Post-synthetic treatments on $Ni_xMn_xCo_{1-2x}(OH)_2$ for the preparation of lithium metal oxides

***I. Rodrigues, J. Wontcheu, D. D. MacNeil***

*Chapter 3 consists of an article submitted to the Journal of Solid State Electrochemistry. The article was prepared by the author under supervision of Dr. MacNeil and Dr. Joseph Wontcheu, post-doctoral fellow in Dr. MacNeil's laboratory aided with the analysis of X-ray diffraction data.*

## *Abstract*

*A series of hydroxides $Ni_xMn_xCo_{(1-2x)}(OH)_2$ for x = 0.00 to 0.50 were prepared. These hydroxides were used as the precursors in the synthesis of electrochemical active lithiated mixed metal oxides, $LiNi_xMn_xCo_{(1-2x)}O_2$. The traditional co-precipitation method was used to synthesize the hydroxides and*

*the effect of different post-synthetic treatments was tested. The solutions after co-precipitation of the hydroxides were heated under hydrothermal or microwave assisted hydrothermal conditions at 180 °C. All samples were analyzed with X-ray diffraction (XRD), scanning electron microscopy (SEM) and electrochemical measurements. We observed that the hydroxides undergo oxidation to an oxyhydroxide phase as the stoichiometry varies during their synthesis and with post-synthetic treatments. As the Ni and Mn concentration increases in the sample, a mixture of the hydroxide and oxyhydroxide phase is obtained. SEM images show that the hydroxide particles after post-synthetic treatment participate in a small sintering effect, while XRD measurements show an increase in crystallinity and reduced turbostratic disorder. In an extended hydrothermal treatment of 24 hours, SEM images showed a significant increase of particle size. The oxides synthesized from these precursors demonstrate similar electrochemical performance with one another. The* $LiNi_xMn_xCo_{(1-2x)}O_2$ *prepared with the hydroxides precursors after the post-synthetic hydrothermal treatment exhibited a discharge capacity of roughly 120 mAh* $g^{-1}$ *at a discharge rate of 30 mA* $g^{-1}$ *when charge–discharged galvanostatically to 4.2 V.*

## *3.1 Introduction*

$LiCoO_2$ has been the most widely used cathode material for rechargeable lithium-ion batteries due to its ease of fabrication, high energy density and excellent cycle life. However, it presents elevated production costs due to the use of expensive and rare cobalt metal, in addition, a number of incidents have raised concerns about its safety [1-3]. There have been numerous reports on lithium mixed metals oxides ($LiNi_xMn_xCo_{(1-2x)}O_2$) as an emerging commercial cathode material for the replacement of $LiCoO_2$ [3-10]. One of the difficulties presented by these mixed metal oxides is the low particle density obtained by the traditional synthesis method. The precursors to the oxides, mixed metal hydroxides ($Ni_xMn_xCo_{(1-2x)}(OH)_2$), are typically prepared through a co-precipitation method that consists of precipitating a mixture of metal salts within a basic solution [5]. This precipitation typically leads to a material with a small particle size and low tap density. In the second reaction step, the hydroxides are subsequently oxidized by air in the presence of a lithium salt at high temperatures to form the lithium metal oxide [3-11]. Multiple strategies during the co-precipitation of the hydroxides as well as during their oxidation have been pursued, including novel synthetic procedures, cation substitutions, and metal doping [12-16]. Typically, the low tap density of the resultant oxide can be traced back to the low density of the precursor hydroxide and thus some researchers have focused on improving the properties of the precursor hydroxide, which should result in an improved oxide [13-14]. Lithium mixed

metal oxides ($LiNi_xLi_{(1/3-2x/3)}Mn_{(2/3-x/3)}O_2$) with a substantial increase particle size (and higher packing density) were obtained by heating the isolated hydroxides precursors ($Ni_xMn_{(1-x)}(OH)_2$) directly after precipitation [13]. These precursors after heat treatment resulted in denser oxides compared to non-treated hydroxide precursors. The higher packing density of the oxide leads to more dense electrode films and a battery with more energy density compared to a battery using oxides from a non-treated hydroxide precursor.

In this report, we will describe the effect of two different post-synthetic treatment methods on the precursor hydroxides towards the morphology and electrochemical performance of the resultant oxides. The first method consists of a hydrothermal treatment within an auto-clave at 180 °C for 5 hours (or 24 hours). The second method is a microwave assisted hydrothermal procedure at 180 °C for 15 minutes. Each hydroxide was subjected to these treatments in solution immediately after co-precipitation. This is the first time that a post-synthetic treatment on these mixed metal hydroxides precursors in solution has been reported. The method proposed here prevents the necessity of two distinct steps, to isolate and dry the precipitate, as well as, it adds pressure as a variable to benefit of the treatment. Previous treatments on the hydroxides were performed after isolation and drying of the product. The particle size and morphology of the samples as-prepared by co-precipitation and after the various treatments were compared. We obtained a significant increase in the primary

particle size with the hydrothermal treatment within 24 hours at hydrothermal heating.

Some authors have suggested that the presence of an oxyhydroxide ($Ni_xMn_xCo_{(1-2x)}OOH$) phase, in addition to the hydroxide phase, is visible when samples are exposed to air or elevated temperatures during their synthesis [16,17]. Here, we observed a change in the degree of oxidation of the hydroxides with a change in stoichiometry and with the post-synthetic treatments. As the value of *x* in $Ni_xMn_xCo_{(1-2x)}(OH)_2$ becomes larger the sample has a tendency of oxidizing into oxyhydroxides. The extent of oxidation is also affected by the treatments under hydrothermal conditions, where an increase in hydrothermal treatment leads to an increase in the amount of the oxyhydroxide phase. Another interesting feature is that the crystallinity of the hydroxide or oxyhydroxide increases as the sample is submitted to post-synthetic treatment.

## *3.2 Experimental*

### 3.2.1 Preparation

$Co(NO_3)_2.6H_2O$ (98%), $Ni(NO_3)_2.6H_2O$ (98%), $Mn(NO_3)_2.6H_2O$ (98%) and $LiOH.H_2O$ (98%) (Aldrich) were used as starting materials and all solutions

were prepared in distilled and degassed water. $Ni_xMn_xCo_{(1-2x)}(OH)_2$ ($x$ = 0.00, 0.05, 0.15, 0.30, 0.45 and 0.50) were first prepared by the co-precipitation method [5]. A solution containing the mixed metal nitrates with the desired stoichiometries (0.4 M) was slowly dropped into a stirred basic solution of LiOH (1.2 M) using a pump delivering the metal solution at ~ 3 mL/min. After delivering the metal solution and rinsing with water to ensure complete delivery of all metal salts, three different routes were developed for the subsequent preparation of the lithium metal oxide. The first route used the hydroxides isolated directly from the co-precipitation after rinsing with distilled water. The second route consisted of a post-synthetic hydrothermal treatment in which the aqueous solution containing the hydroxides was transferred into a Teflon container and placed within a sealed digestive vessel (Parr). The vessel was then placed in an oven at 180 °C for 5 or 24 hours. In the third route a microwave assisted hydrothermal treatment was applied. Here, the solution was sealed in closed Teflon liners, which were placed in a turntable for uniform heating within a microwave digestion system (MARS5, CEM). The system operated at a frequency of 2.45 GHz and a power of 1200 W. The temperature of the microwave was ramped rapidly to 180 °C and kept under these hydrothermal conditions for 15 min. In all cases the precipitate after treatment was rinsed several times with distilled water and dried overnight under dry air. The final lithiated oxide, $LiNi_xMn_xCo_{(1-2x)}O_2$, was prepared by mixing the precursors hydroxides with an excess (3%) amount of LiOH. After pelletizing the solid mixture it was heated in air at 500 °C for 3 h, ground, a new pellet formed and

heated at 900 °C for 3 h followed by a quench cooling (between large copper plates).

### 3.2.2 Characterization

The crystalline phases of samples were determined by an X-ray diffractometer (XRD, Bruker D8 Advance) using Cu Kα radiation with a step size of 0.025° and step time of 15 s in a range of 15 to 60°. Scanning Electron Micrographs (SEM) were carried out on a Hitachi S-4300 microscope. Thermogravimetric analysis (TGA) measurements were performed under a flowing atmosphere of dry air with a TA Instrument thermogravimetric analyser (SDT600) at 15 °C/min from room temperature to 500 °C. Electrochemical evaluations were performed by combining the oxide with 10% of a conductive carbon (Super-P Li, Timcal) and 10% polyvinylidene difluoride (PVDF, 5.5% in N-methylpyrroldinone (NMP)) with an excess of NMP to make a slurry. The slurry (80% active) was then deposited on a carbon coated Al foil using a doctor blade. The slurry was then dried at 70 °C and electrodes 13 mm in diameter were cut for cell assembly in standard 2032 coin-cell hardware (Hohsen) using a single lithium metal foil as both counter and reference electrode and a Celgard 2200 separator. Cells were assembled in an argon-filled glove box using 1M $LiPF_6$ in ethylene carbonate (EC)/ diethyl carbonate (DEC) (3:1 by vol) electrolyte (UBE). Electrochemical evaluations were performed by charging and

discharging between 2.2 and 4.2 V (or 4.5 V) using a current rate of 5 mA $g^{-1}$ for the first 5 cycles and a current of 30 mA $g^{-1}$for the next 50 cycles at 30 °C on a BT-2000 electrochemical station (Arbin).

## *3.3 Results and Discussion*

### 3.3.1 Mixed metal hydroxides

A full range of $Ni_xMn_xCo_{(1-2x)}(OH)_2$ hydroxides ($x$ = 0 to 0.50) were prepared by the traditional co-precipitation method [5] and then subjected to two different post-synthetic treatments at 180 °C. Heating the isolated hydroxides at an elevated temperature has been previously shown to be an efficient method towards more dense hydroxide particles [13]. The post-synthetic treatments carried out in this work, are unique in that for the first time the heating step is applied to the hydroxides while maintained within the synthetic solution without isolation and drying of the product. These treatments have the additional benefit of high pressure, which presents an additional variable that could lead to an improved material.

Figure 3.1 shows the X-ray diffraction pattern of all samples within the series $Ni_xMn_xCo_{(1-2x)}(OH)_2$ ($x$ = 0.00 to 0.50) before and after the two post-

synthetic treatments. Consider initially the non-treated sample (black line in Figure 3.1). It is clear that as Ni and Mn are introduced into the sample (increasing $x$) that there is a change in diffraction pattern. As Ni and Mn are introduced in the series, the pristine $CdI_2$ structure becomes unstable and the development of a turbostratic phase contributes to the change in the diffraction pattern as reported by Jouanneau *et al*. [11]. The turbostratic disorder consists of either random rotations or translations of the crystalline planes within the $Ni_xMn_xCo_{(1-2x)}(OH)_2$ structure. The effect of the turbostratic disorder on the diffraction profile is significant as the Bragg peaks become more diffuse and decrease significantly in intensity.

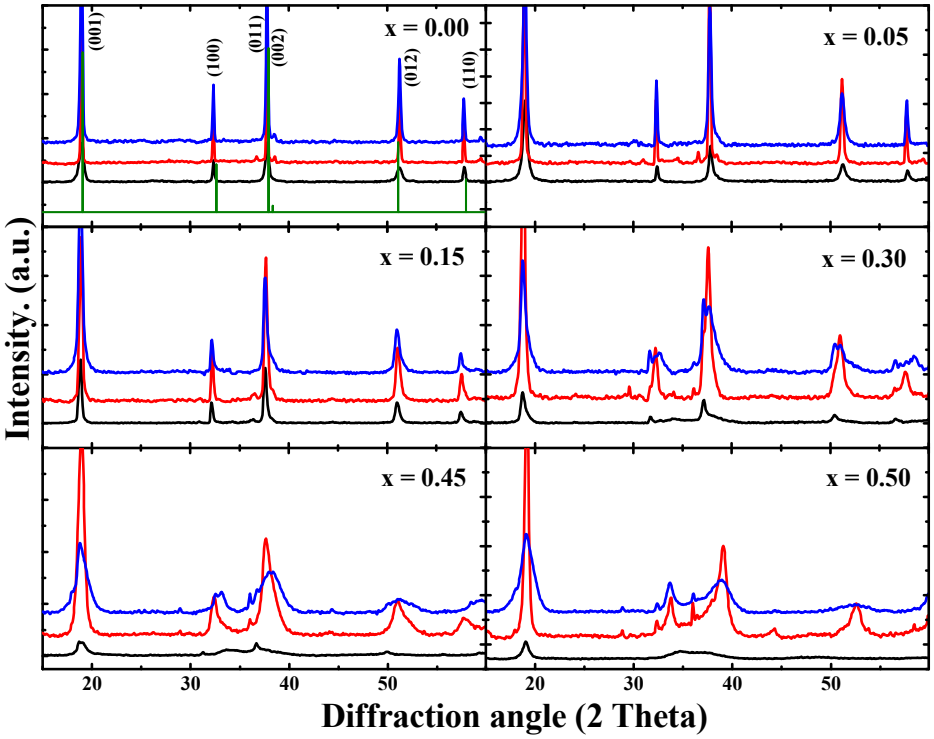


***Figure 3.1:*** *XRD profiles of $Ni_xMn_xCo_{(1-2x)}(OH)_2$. (bottom black line = as prepared by co-precipitation; middle red line = after 5 hours hydrothermal, top blue line = after microwave assisted post-synthetic hydrothermal treatment and the green lines in the x = 0.00 quadrant is a representation of the Bragg peaks, with indicated Miller indices, for $Co(OH)_2$ that can be used as a reference.*

The development of the turbostratic phase seems to favors the oxidation of the samples into oxyhydroxides. This change in diffraction profile towards broad Bragg peaks with lower intensities as well as the appearance of new peaks at lower diffraction angles can be attributed to the oxidation of the sample into oxyhydroxides [16]. Kosova *et al*. described an increase in oxidation state of hydroxide samples with increasing Mn/Co content [18], they showed that the

interslab distance of samples with high content of Mn increases as a result of the intercalation of anions and water to compensate positive charge added with $Mn^{3+}$ /$Mn^{4+}$ leading to samples with very low cristalinity. Interestingly, this change is also seen from the difference in colour between the samples. Immediately after synthesis, the samples with a high value of *x* were light pink in colour. After rinsing with distilled water a colour change to light brown was observed. van Bommel *et al.* attributed this colour change to an oxidative process upon heating these hydroxides in air [16]. The samples containing a low concentration of Ni and Mn (low value of *x*), do not demonstrate a colour change, maintaining their pink colour throughout the rinsing procedure, leading to non-oxidized samples. Thus, there is an increase in the possibility of oxidation of the hydroxide as the amount of Ni and Mn is increased in the hydroxides [16-17]:

$$2\ Ni_xMn_xCo_{(1-2x)}(OH)_2 + ½\ O_2 + \rightarrow 2\ Ni_xMn_xCo_{(1-2x)}OOH + H_2O.$$

The oxyhydroxide phase is present in some of the samples as-prepared via co-precipitation, as well as after the two post-synthetic treatments. As the samples are treated at higher temperature during the post-synthetic treatment, the Bragg peaks became sharper and more intense indicating a more well defined oxyhydroxide phase. The exposure to elevated temperatures eliminates the structural defects that are readily apparent at lower temperatures and cause broadening of the diffraction pattern. As time at elevated temperature increases (microwave compared to traditional hydrothermal), there is an increase in the

development of the oxyhydroxide phase. This is clearly shown in Figure 3.1 where more intense and well-defined Bragg peaks are observed for the hydrothermally treated samples (red line in Figure 3.1) compared to samples treated with the microwave (blue line in Figure 3.1). This improvement in crystallinity at elevated temperature is also apparent with the non oxidized hydroxide samples (low values of $x$ in $Ni_xMn_xCo_{(1-2x)}(OH)_2$). The crystallinity of the product improves with the time spent at elevated temperatures, since those treated hydrothermally (5 hours at 180 °C) demonstrate an improved crystalline structure compared to those treated under microwave radiation (15 min at 180 °C).

Figure 3.2 shows the XRD diffraction patterns of samples hydrothermally treated for 24 hours ($x$ = 0.00, 0.45 and 0.50). We can clearly see a well defined diffraction at ~ 35°, this peak originates from the oxyhydroxide phase [17]. Two other small peaks at ~ 28 and 44° are also visible and these are related to the oxyhydroxide phase. If we compare the XRD pattern shown in Figure 3.1 and 3.2 of the sample with $x$ = 0.00, we observe a pure single phase hydroxide sample in Figure 3.1 for the sample as prepared by the traditional co-precipitation, while after hydrothermal treatment for 24 hours (Figure 3.2) a small peak at a diffraction angle of ~ 35° is observed indicating the oxidation of some of the sample to an oxyhydroxide phase. A similar trend is observed for the other hydroxide samples and it is possible to conclude that the hydrothermal treatment favors the oxidation of the hydroxides samples into oxyhydroxides.

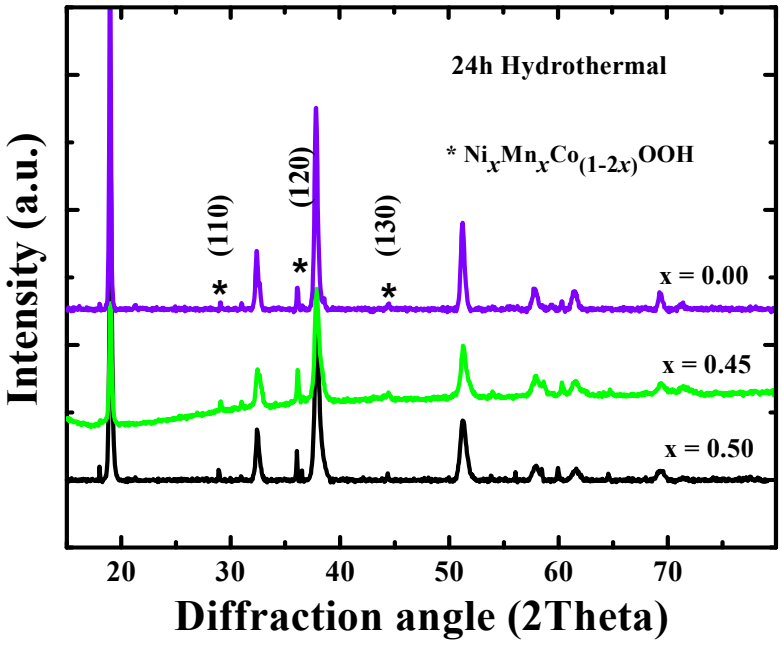


***Figure 3.2:*** *XRD profiles of $Ni_xMn_xCo_{(1-2x)}(OH)_2$ demonstrating the development of the $Ni_xMn_xCo_{(1-2x)}OOH$ structure after post-synthetic hydrothermal treatment for 24 hours.*

The amount of oxidation within these samples can be explored via thermogravimetric experiments [11]. TGA on all samples were performed under a flowing atmosphere of dry air and the weight loss for each sample was compared. It is expected that more oxidized samples will demonstrate a lower weight loss due to the sample already being partially oxidized. For clarity, we present only the TGA results for the sample as prepared by the traditional co-precipitation and after the hydrothermal treatment (5 hours) with $x$ = 0.30 in Figure 3.3. The TGA profile can be separated into two different regions. The first includes the mass loss by each sample up to 250 °C and is attributed to the

release of absorbed water in the material. The mass loss above 250°C can be attributed mainly to the oxidation of samples into the oxide phase and the decomposition of interlayer ions contained within the structure of hydroxides. Sample as prepared by co-precipitation had a mass loss of roughly 8% above 250 °C, while the same sample but hydrothermally treated after synthesis had mass loss of only roughly 4%. This decrease in mass loss after hydrothermal treatment supports our view that the hydroxides oxidizes to an oxyhydroxide phase during post-synthetic hydrothermal treatment and this was supported by our XRD investigation described previously (Figures 3.1 and 3.2).

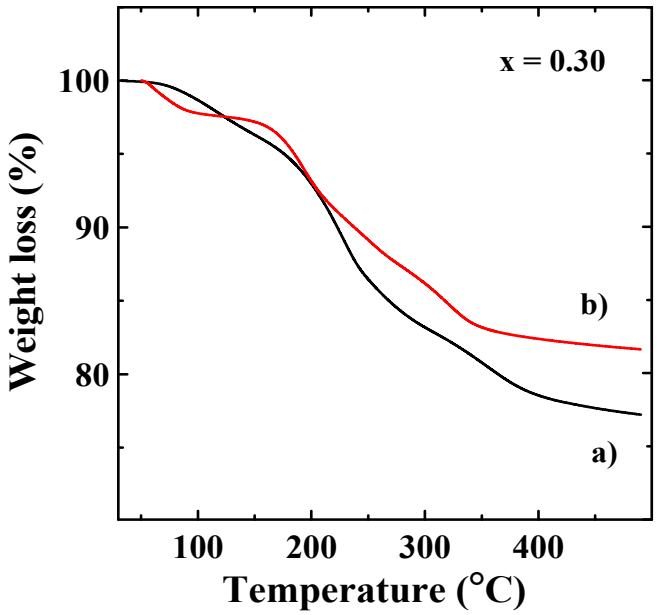


***Figure 3.3:*** *TGA measurements (15 °C/ min, dry air) for $Ni_xMn_xCo_{(1-2x)}(OH)_2$ as prepared by traditional co-precipitation (a) and after post-synthetic 5 hours hydrothermal treatment (b).*

The structure refinement was carried out by a Rietveld analysis [19-22] using the integrated powder diffraction software TOPAS version 3.0. [23].

Careful analysis of the powder pattern revealed the presence of both a hydroxide phase and an oxyhydroxide phase, therefore a two phase Rietveld refinement was performed. The background of the experimental data was interpolated linearly between selected points. The shape of the reflections was modeled with a pseudo-Voigt function. Preferred orientation was treated using March's function. The atomic coordinates of the oxygen atoms were refined without constraint. The starting values for the atomic positions were those of the $Co(OH)_2$ structure, in space group P-3m1 (N° 164) [24] and the CoOOH structure, in the space group $P6_3/mmc$ (N° 194) [25]. There were no corrections performed for absorption. The lattice parameters obtained for the samples synthesised after hydrothermal treatment (5 hours) which demonstrate both hydroxide and oxyhydroxide characteristics are presented in Table 3.1. The results of Table 3.1 agree with the results described above in that the amount of oxyhydroxide phase increases as the Ni/Co content of the sample increases. The theoretical lattice parameters for the oxyhydroxide phase ($Ni_xMn_xCo_{(1-2x)}OOH$), *a* (Å) = 3.09 and *b* (Å) = 4.61), are lower than that of the hydroxide phase ($Ni_xMn_xCo_{(1-2x)}(OH)_2$), *a* (Å) = 3.22 and *b* (Å) = 4.70) [16-17]. Based on these values and the data obtained on the Table 3.1, as well as the XRD profiles on Figure 3.1, we can deduce that lattice parameters are reduced, compared to the literature mainly because of the formation of the oxyhydroxide phase in some of our samples. As seen in Table 3.1, the amount of the oxyhydroxide phase increases with *x* values.

***Table 3.1:*** *Lattice parameters, unit cell volume and amount of oxyhydroxide phase present in* $Ni_xMn_xCo_{(1-2x)}(OH)_2$ *after post-synthetic hydrothermal treatment for 5 hours.*

| $Ni_xMn_xCo_{(1-2x)}(OH)_2$ | *x* | *a* (Å) | *c* (Å) | V ($Å^3$) | Oxyhydroxide phase (%) |
|---|---|---|---|---|---|
| Hydrothermal | 0.00 | 3.279 | 4.716 | 41.57 | 0.15 |
| | 0.05 | 3.244 | 4.711 | 41.25 | 3.75 |
| | 0.15 | 3.214 | 4.685 | 41.03 | 3.77 |
| | 0.30 | 3.193 | 4.680 | 40.94 | 6.03 |
| | 0.45 | 3.188 | 4.678 | 40.86 | 7.22 |
| | 0.50 | 3.181 | 4.651 | 40.70 | 8.35 |

Scanning electron microscopy (SEM) was used to determine the effect of post-synthetic treatments on the particle size and morphology of each of the samples. While the morphology of all the samples is similar, an increase in particle size with post-synthetic treatment is visible. Figure 3.4 demonstrates a small sintering effect after high temperature treatment. Comparing particles size from Figure 3.4a, as-prepared by co-precipitation, to Figure 3.4b and 3.4c after post-treatment, we can see that Figure 3.4b, (hydrothermally treated sample) has slightly larger particles.

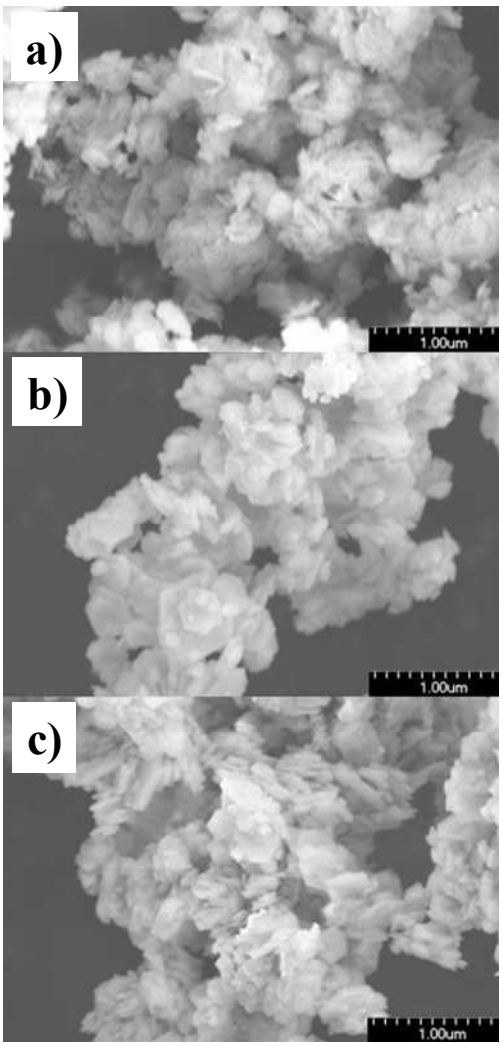


***Figure 3.4:*** *SEM images of $Ni_xMn_xCo_{(1-2x)}(OH)_2$ (x = 0.15) (a) as prepared by co-precipitation, (b) after hydrothermal and (c) after microwave assisted post-synthetic hydrothermal treatment.*

The sintering effect at elevated temperatures is not uncommon and leads to an increase in crystallinity, readily apparent in the diffraction profiles shown in Figure 3.1. As the sample sinters the disorder within the structure is relieved and there is the development of more well defined Bragg reflections (see Figure 3.1). This development in Bragg reflections increases as the sintering or time at

elevated temperature increases. The particle sintering effect under extended hydrothermal treatment is seen clearly when a sample ($x = 0.00$) is treated under hydrothermal conditions for 24 hours. Figure 3.5 presents a comparison of this sample with the sample treated for 5 hours. This increase in the primary particle size of the precursor should result in an increase in the particle density of the posterior oxide.

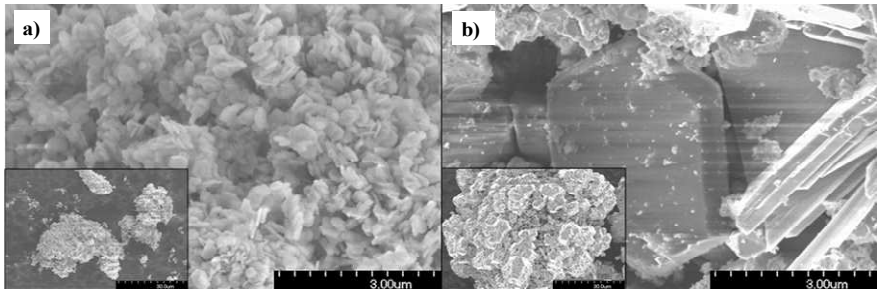


***Figure 3.5:*** *SEM images of $Ni_xMn_xCo_{(1-2x)}(OH)_2$ (x = 0.00) submitted to a) 5 hours and b) 24 hours of post-synthetic hydrothermal treatment.*

Figure 3.6 demonstrates the effect of Ni and Mn concentration on the particles size of the hydroxides prepared by co-precipitation before any post-synthetic treatment. As the Ni and Mn content within the sample increases ($x \rightarrow 0.50$), the particle size demonstrates a significant decrease. This can be attributed to the turbostratic disorder present [11] in samples with high content of Ni and Mn. The random rotations and translations lead to less growth of the particle as disorder causes a decrease in the ability to build upon the lattice of the particle. The X-ray diffraction patterns (Figure 3.1) gives small broad peaks, which is indicative of turbostratic disorder, are visible as $x$ increases to 0.50. In the macroscopic scale, this disorder tends to produce a sample with small particle

size. We have shown SEM images related to the samples as-prepared by co-precipitation only, but the same trend is observed for both post-synthetic treated hydroxides.

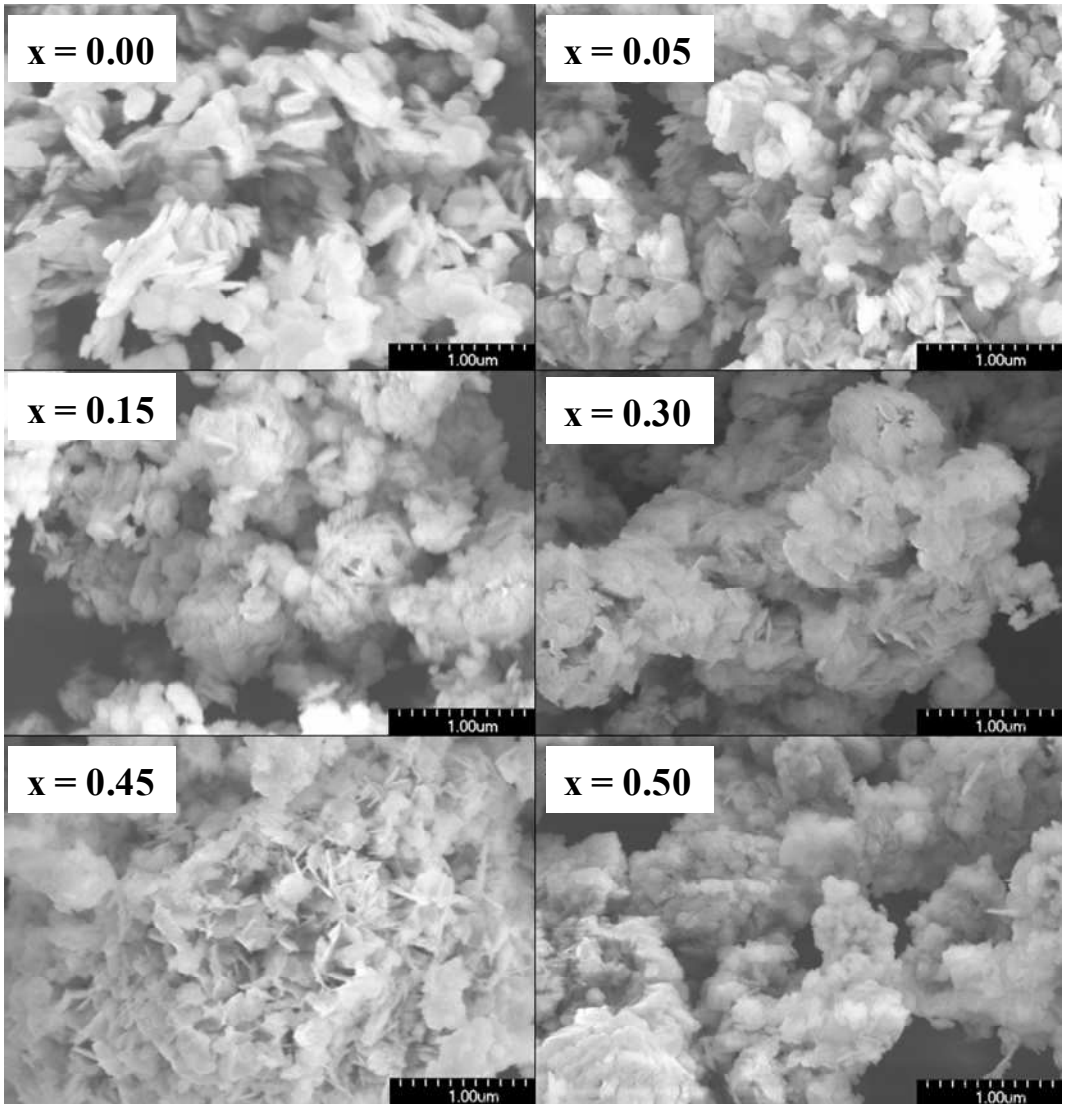


***Figure 3.6:*** *SEM images of $Ni_xMn_xCo_{(1-2x)}(OH)_2$ as prepared by co-precipitation for the indicated concentration of x.*

### 3.3.2 Lithium mixed metal oxides

For application within lithium-ion batteries, these mixed metal hydroxides need to be oxidized into lithiated oxides. It has been found that the morphology of the precursor hydroxide has a significant effect on the ability to produce the optimal dense, spherical lithiated oxides [13-16]. Thus, it is important to fully investigate various synthesis and treatment methods on the hydroxides such that one can obtain dense oxides. These dense oxides will produce dense electrodes for use in lithium-ion batteries. The lithiated oxides were prepared by reacting the precursor hydroxides with a slight excess of LiOH (3%) in air at 500 °C for 3 hours followed by 900 °C for 3 hours with quench cooling for each step. Figure 3.7 shows the XRD patterns of the oxides produced from the various hydroxide precursors described above. The heat treatments imposed to the hydroxides precursors do not seem to affect the structure or crystalinity of the oxides as Figure 3.7 shows a similar pattern for all samples. For $LiNi_xMn_xCo_{(1-2x)}O_2$ ($x$ = 0.05) prepared from precursors without post-synthetic treatment there is an additional peak around 45° that seems to be related to development of an oxide impurity. Nevertheless, there is a smooth shift of the Bragg peaks as a function of the Ni and Mn content.

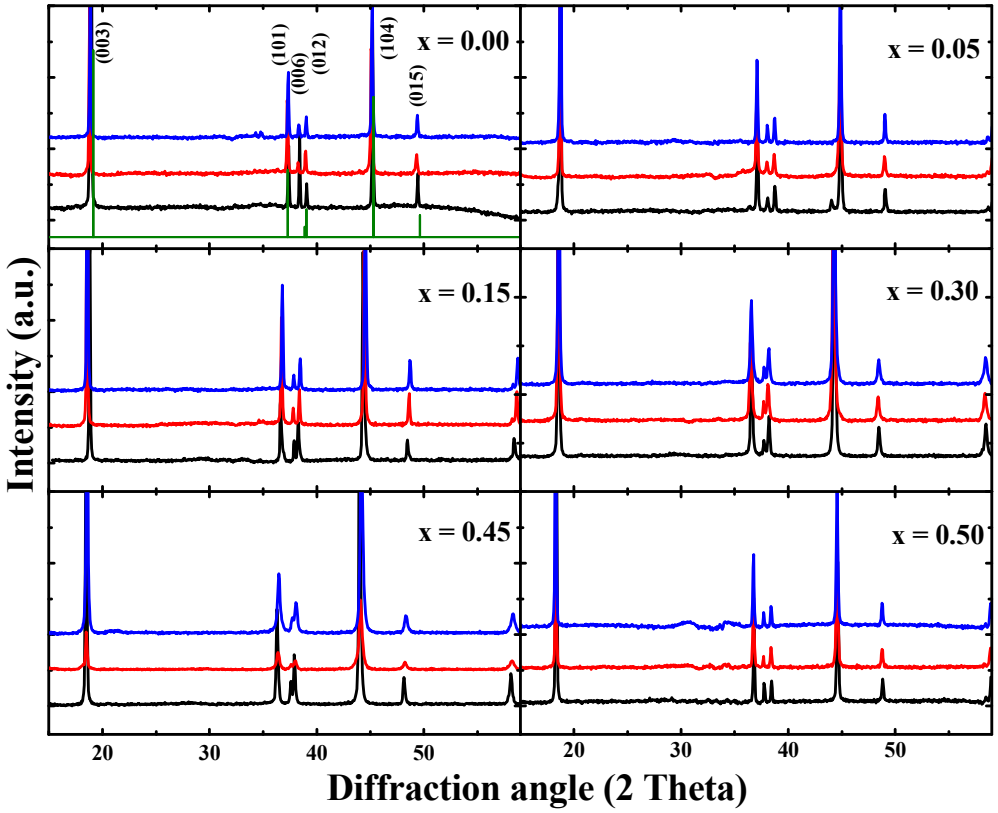


***Figure 3.7:*** *XRD profiles of $LiNi_xMn_xCo_{(1-2x)}O_2$. (bottom black line = precursor hydroxide as prepared by co-precipitation; middle red line = precursor after hydrothermal (5 hours), top blue line = after microwave assisted hydrothermal treatment and the green lines in the x = 0.00 quadrant is a representation of the Bragg peaks, with indicated Miller indices, for $LiCoO_2$ that can be used as a reference.*

As expected and depicted in Table 3.2, there is an increase in both the *a* and *c* lattice parameters with increasing Ni and Mn concentration.

***Table 3.2:*** *Lattice parameters and cell unit volume of $LiNi_xMn_xCo_{(1-2x)}O_2$, indexed using the $R\bar{3}m$ space group.*

| | $x$ in $LiNi_xMn_xCo_{(1-2x)}O_2$ | $a$ (Å) | $c$ (Å) | V (Å$^3$) |
|---|---|---|---|---|
| Co-precipitation | 0.00 | 2.885 | 14.250 | 101.45 |
| | 0.05 | 2.863 | 14.250 | 101.03 |
| | 0.15 | 2.891 | 14.301 | 102.53 |
| | 0.30 | 2.881 | 14.329 | 102.45 |
| | 0.45 | 2.890 | 14.327 | 102.47 |
| | 0.50 | 2.894 | 14.305 | 102.55 |
| Hydrothermal | 0.00 | 2.891 | 14.239 | 101.55 |
| | 0.05 | 2.885 | 14.271 | 101.97 |
| | 0.15 | 2.885 | 14.277 | 101.96 |
| | 0.30 | 2.887 | 14.281 | 102.05 |
| | 0.45 | 2.890 | 14.290 | 102.11 |
| | 0.50 | 2.901 | 14.300 | 102.54 |
| Microwave | 0.00 | 2.872 | 14.268 | 101.96 |
| | 0.05 | 2.879 | 14.280 | 101.99 |
| | 0.15 | 2.890 | 14.293 | 102.01 |
| | 0.30 | 2.895 | 14.302 | 102.11 |
| | 0.45 | 2.899 | 14.311 | 102.25 |
| | 0.50 | 2.900 | 14.320 | 102.40 |

Figure 3.8 shows SEM images of the $LiNi_xMn_xCo_{(1-2x)}O_2$ prepared from hydroxide precursors either as-prepared by co-precipitation (Figure 3.8a), hydrothermal treated for 5 hours (Figure 3.8b) or microwave hydrothermal treated (Figure 3.8c). Each sample had a Ni and Mn concentration of 0.15

($x$ = 0.15) and this figure can be compared with that of the hydroxide sample, previously presented in Figure 3.4.

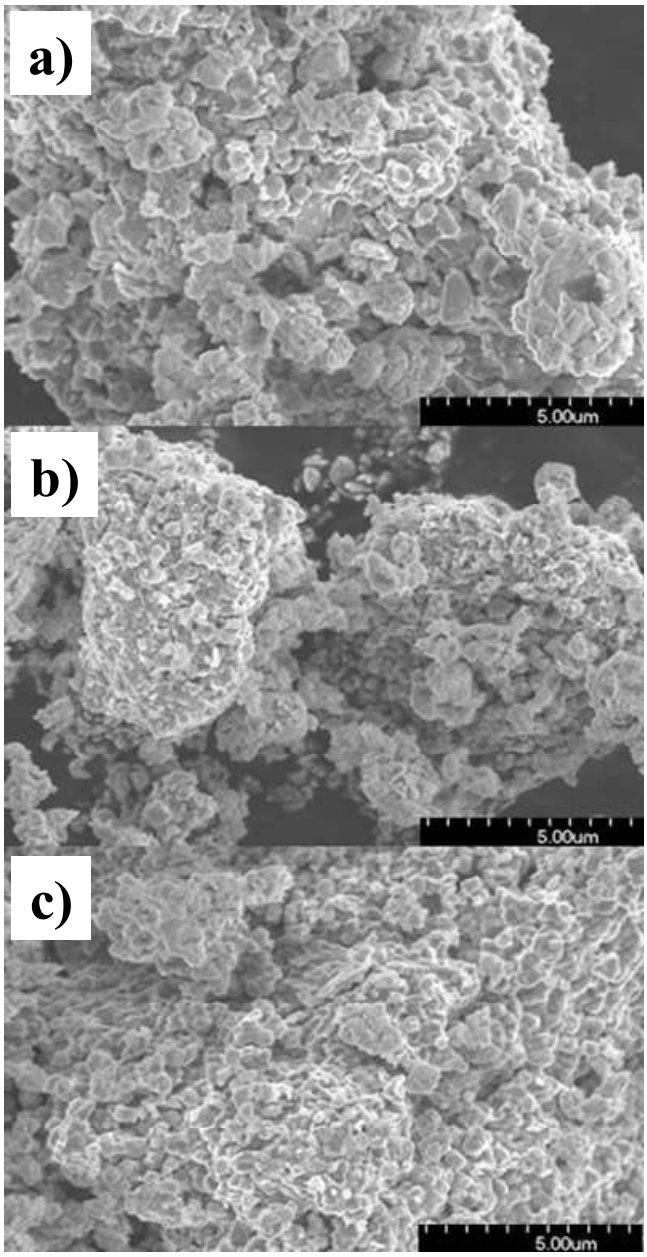


***Figure 3.8:*** *SEM images of $LiNi_xMn_xCo_{(1-2x)}O_2$ (x = 0.15) synthesized from the hydroxide precursors (a) as prepared by co-precipitation, (b) after 5 hr hydrothermal and (c) after microwave assisted post-synthetic hydrothermal treatment.*

While the particle size of the precursor hydroxides showed a small increase with post-synthetic treatment at high temperature, the particle size of all oxides, regardless of the particle size of the precursor, are similar and this is in contrast to previous reports [13]. It should be noted here that the differences seen with the main hydroxide precursors (except for the hydrothermal treatment for 24 hours) in this report are much smaller than reported previously and would be difficult to discern after the high temperature exposure required for oxide formation.

The capacity retention (capacity *versus* cycle number) for the electrodes of all oxides cycled at 30 $^{o}$C between 2.2 and 4.2 V are showed in Figure 3.9. The first five cycles were charged at a rate of 5 mA $g^{-1}$, while the remaining cycles were charged at a rate of 30 mA $g^{-1}$. All samples, except $LiCoO_2$, present good capacity retention.

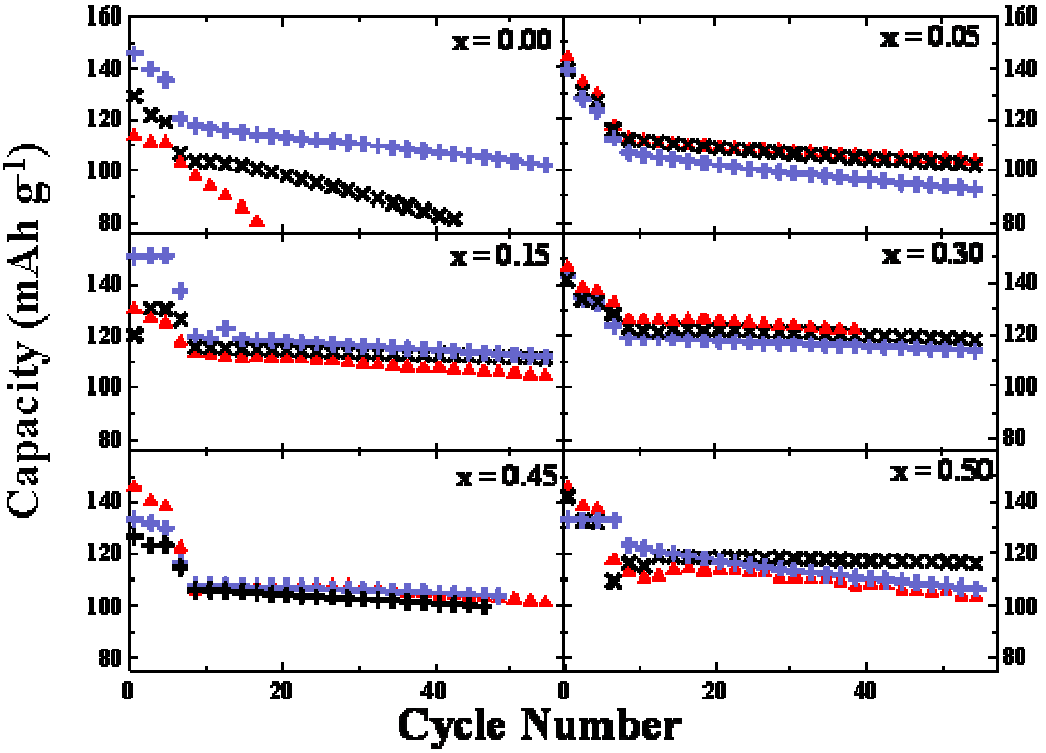


***Figure 3.9:*** *Capacity vs cycle number for $LiNi_xMn_xCo_{(1-2x)}O_2$ charged to 4.2V. The hydroxides precursors were as-prepared by co-precipitation (▲red), after hydrothermal (x black) and after microwave assisted post-synthetic hydrothermal treatment (+ blue). The charge-discharge curves consist of 5 cycles at a rate of 5 mA $g^{-1}$ followed by 50 cycles at 30 mA $g^{-1}$.*

The capacity of $LiCoO_2$ cycled at 4.2 V decreases drastically with increasing cycle number. This characteristic is typical of $LiCoO_2$ prepared via hydroxides from co-precipitation and has been readily observed in the literature [6-12]. Interestingly, the $LiCoO_2$ samples prepared from hydroxides that were subjected to a post-synthetic treatment demonstrate improved capacity retention, although commercial material (not shown) demonstrates superior capacity retention ability. This improvement is likely due to the increased crystallinity

and loss of turbostratic disorder observed for the $Co(OH)_2$ sample after high temperature post-synthetic treatment. The range in capacity values (between 150 and 90 mAh $g^{-1}$) presented in Figure 3.9 are within the values that have been presented previously in the literature for the same series. Figure 3.10 presents the electrochemical performance of the whole series but using an upper cut-off potential of 4.5 V. The series charged to 4.5 V demonstrated an increase in capacity of about 20 mAh $g^{-1}$ for each sample. Interestingly, the capacity retention is better for the $LiCoO_2$ sample when cycled to 4.5 V when compared to 4.2 V and this could be due to a better surface decomposition layer at 4.5 V that eliminates parasitic side reactions. Ultimately, the post-synthetic treatment experiments on the mixed metal hydroxides do not result in a large change in electrochemical performance as compared to the non-treated samples except for the $LiCoO_2$ sample prepared under co-precipitation conditions.

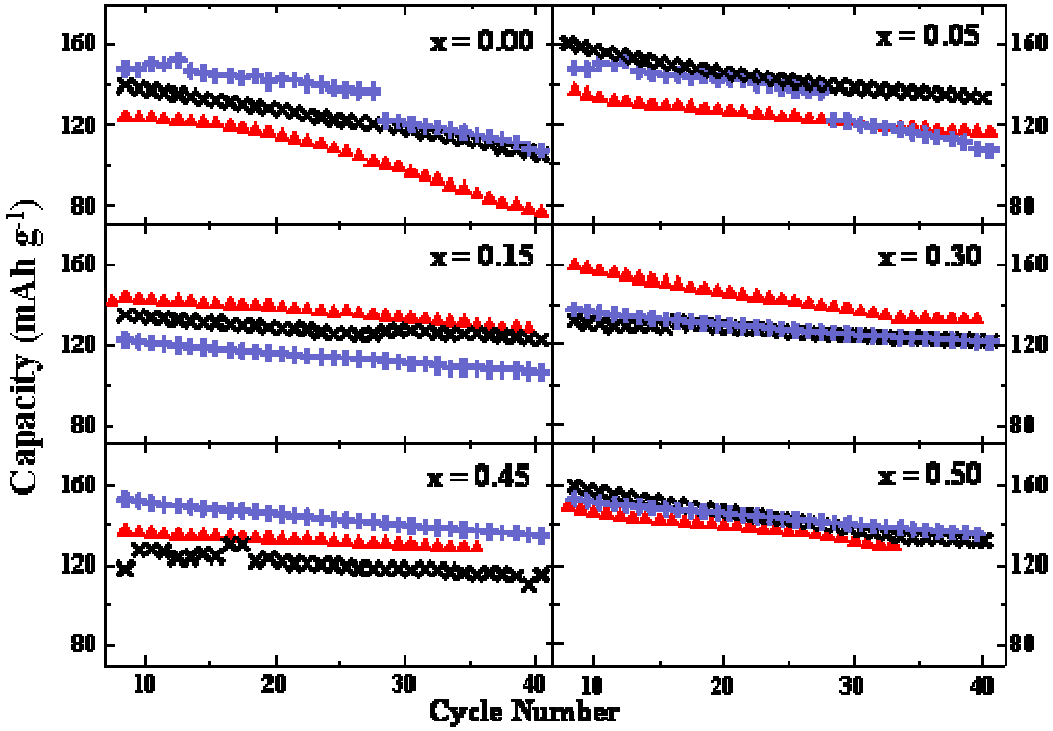


***Figure 3.10:*** *Capacity vs cycle number for $LiNi_xMn_xCo_{(1-2x)}O_2$ charged to 4.5V. The hydroxides precursors were as-prepared by co-precipitation (▲red), after hydrothermal (x black) and after microwave assisted post-synthetic hydrothermal treatment (+ blue). The charge-discharge curves consist of 45 cycles at a rate of 30 mA $g^{-1}$.*

## *3.4 Conclusion*

We have demonstrated two different post-synthetic treatments on $Ni_xMn_xCo_{(1-2x)}(OH)_2$, *via* hydrothermal and microwave assisted hydrothermal techniques, with the goal of producing more dense hydroxides. These treatments are performed in solution right after the co-precipitation step and have been found to increase the crystallinity and particle size of the samples as compared to the non-treated samples. The samples containing higher concentrations of Ni and Mn demonstrate an increase in the amount of oxyhydroxide phase present in the sample and the degree of oxidation is increased with treatment at elevated temperature. Unfortunately, the small increase in particle size seen in the hydroxides do not result in a large change in the particle size of the oxides synthesized using the treated hydroxides. The electrochemical performance of the oxides produced at high temperature from the treated hydroxides ($LiNi_xMn_xCo_{(1-2x)}O_2$) demonstrate a capacity and capacity retention with increasing cycle number similar to those reported previously in the literature. Interestingly, $LiCoO_2$ prepared from the treated $Co(OH)_2$ samples demonstrate improved capacity retention as compared to those as-prepared by co-precipitation.

## *3.5 References*


**1.** Amatucci, G. G.; Tarascon, J-M.; Klein, L. C. *Solid State Ionics* **1996**, 83, 167.

**2.** Numata, K.; Sakaki, C.; Yamanaka, S. *Chem. Lett.* **1997**, 26, 725.

**3.** Liu, Z.; Yu, A.; Lee, J. Y. *J. Power Sources* **1999**, 81-82, 416.

**4.** Lu, Z.; MacNeil, D. D.; Dahn, J. R. *Electrochem. Solid-State Lett.* **2001**, 11, A191.

**5.** Lu, Z.; MacNeil, D. D.; Dahn, J. R. *Electrochem. Solid-State Lett.* **2001**, 12, A200.

**6.** MacNeil, D. D.; Lu, Z.; Dahn, J. R. *J. Electrochem. Soc.* **2002**, 149, A1332.

**7.** Yoshizawa, H.; Ohzuku, T. *J. Power Sources.* **2007,** 174, 813.

**8.** Paulsen, J. M.; Dahn, J. R. *J. Electrochem. Soc.* **2000**, 147, 2478.

**9.** Yabuuchi, N.; Ohzuku, T. *J. Power Sources* **2005** 146, 636.

**10.** Ohzuku, T.; Makimura, Y. *Chem. Lett.* **2001**, 30, 642.

**11.** Jouanneau, S.; Dahn, J. R. *Chem. Mater.* **2003**, 15, 495.

**12.** Jouanneau, S.; Eberman, K. W.; Krause, L. J.; Dahn, J. R. *J. Electrochem. Soc.* **2003**, 150, A1637.

**13.** Barkhouse, D. A. R.; Dahn, J. R. *J. Electrochem. Soc.* **2005**, 152, A746.

**14.** Yabuuchi N, Koyama N, Ohzuku T. *J. Electrochem. Soc.* **2005**, 152, A1434.

**15.** Zhao, X.; Zhou, F.; Dahn, J. R. *J. Electrochem. Soc.* **2008**, 155, A642.

**16.** van Bommel, A.; Dahn, J. R. *J. Electrochem. Soc.* **2009**, 156, A362.

**17.** Butel, M.; Gautier, L.; Delmas, C. *Solid State Ionics* **1999**,122, 271.

**18.** Kosova, N. V.; Devyatkina, E. T.; Kaichev, V. V. *J. Power Sources* **2007**, 174, 735.

**19.** Rietveld, H. M. *J. Appl. Crystallogr.* **1967**, 22, 151.

**20.** Rietveld, H. M. *J. Appl. Crystallogr.* **1969**, 2, 65.

**21.** Wiles, D. B.; Young, R. A. *J. Appl. Crystallogr.* 1981, 14, 149.

**22.** Hill, R. J.; Howard, C. J. *J. Appl. Crystallogr.* **1985**, 18, 173.

**23.** Pertlik, F.; *Monatshefte fuer Chemie und verwandte Teile anderer Wissenschaften* **1978**, 109.

**24.** Deliens, M.; Goethals, H. *Mineralogical Magazine* **1973**, 39, 152.

# Chapter 4

# A novel co-precipitation method towards the synthesis of $Ni_xMn_xCo_{(1-2x)}(OH)_2$ for the preparation of lithium metal oxides

***I. Rodrigues, J. Wontcheu, D. D. MacNeil***

*Chapter 4 consists of an article submitted to the Journal of Power Sources. The article was prepared by the author under supervision of Dr. MacNeil and Dr. Joseph Wontcheu, post-doctoral fellow in Dr. MacNeil's laboratory aided with the analysis of X-ray diffraction data.*

## *Abstract*

*A series of mixed metal hydroxide ($Ni_xMn_xCo_{(1-2x)}(OH)_2$) precursors for the preparation of lithiated mixed metal oxides ($LiNi_xMn_xCo_{(1-2x)}O_2$) were prepared using a novel co-precipitation approach based on the thermal decomposition of urea. Three different methods were used to achieve the*

*temperature required to decompose urea and subsequently precipitate the hydroxides. The first two methods consisted of either a hydrothermal or microwave assisted hydrothermal synthesis at 180 °C and elevated pressures. The final method was an aqueous reflux at 100 °C. A complete series (x = 0.00 to 0.50) was prepared for each method and a full structural (XRD, TGA, SEM) and electrochemical characterization was performed before and after converting the materials to lithiated metal oxides ($LiNi_xMn_xCo_{(1-2x)}O_2$). We observed the formation of a very complex structure after the co-precipitation of the hydroxides. SEM images demonstrate that the morphology and particle size of the hydroxide particles varies significantly from x = 0.00 to 0.50 under hydrothermal condition. There is also a significant change in particle morphology as the urea decomposition method is varied. The XRD profiles of the oxides synthesized from these hydroxide precursors all demonstrated phase pure oxides that provided good electrochemical performance.*

## *4.1 Introduction*

Rechargeable lithium-ion batteries are the main power source for most high-end portable electronic devices. Currently, many of the major lithium-ion battery manufacturers use $LiCoO_2$ as the positive electrode material due to its ease of fabrication, high energy density and excellent cycle life. However there has been a push to replace $LiCoO_2$ because of its elevated production costs and safety concerns about its reactivity [1-4]. A major research direction has been to partially substitute the Co in $LiCoO_2$ with transition metals such as Ni and Mn. These so-called mixed metal oxides have been able to provide cathode materials with high capacity, good capacity retention, and lower production costs [4-9]. They have also started to appear as the cathode material in commercial cells [10].

Mixed metal hydroxides ($Ni_xMn_xCo_{(1-2x)}(OH)_2$) are used as precursors to the electrochemical active lithiated mixed metal oxides ($LiNi_xMn_xCo_{(1-2x)}O_2$). One of the difficulties presented by these hydroxides is the low particle density obtained by the traditional synthesis method [8, 11]. If one were able to produce more dense materials this would lead directly to denser electrode films and a battery with more energy. The typical synthesis method used consists of the co-precipitation of a mixture of metal salts within a basic solution [6]. There are numerous articles which have reported on various strategies to increase particle density during the co-precipitation of the hydroxides, such as novel synthetic

procedures, cation substitutions, metal doping, or modifications to the synthetic procedure during the oxidation to the electrochemically active lithiated material [1, 8, 12-13].

In our previous work, we applied different post-synthetic treatments to mixed metal hydroxides obtained by the traditional co-precipitation method [14]. In the present article, we will report a novel synthetic approach to the co-precipitation of the mixed metal hydroxides, $Ni_xMn_xCo_{(1-2x)}(OH)_2$. The approach is based on the thermal decomposition of urea at elevated temperature. As the urea decomposes the pH of the solution increases and it results in the precipitation of the hydroxides from solution. In the traditional co-precipitation method, hydroxides are immediately precipitated when mixed with the basic solution, the precipitation from urea decomposition will take place when the solution containing the metal salts and urea achieve a temperature higher than 90 °C. Thus, all precursors are in the solution state at room temperature and this could lead to a more homogenous precipitation of $Ni_xMn_xCo_{(1-2x)}(OH)_2$ compared to the traditional technique. Moreover, the elevated temperature and increased pressure represent additional parameters not available to the traditional method that could improve the morphology of product and increase the density of the final oxide. This could lead to increased energy density of cathode electrodes.

The traditional co-precipitation method (rapid introduction of a solution of mixed metals into a solution of high pH) results in the rapid saturation of hydroxide once the precipitating agent ($OH^-$) is readily consumed in the solution. Even in an excess of hydroxide, this typically results in a solution containing a wide particle size distribution and particles with low tap density [15, 16]. The thermal decomposition of urea (reaction scheme below) takes place at temperatures greater than 90 °C [15-19].

$$NH_2CONH_2 + H_2O \xrightarrow{\Delta} 2\,NH_3 + CO_2 \quad ,$$

it represents an alternative precipitation route that has not been investigated for mixed metal hydroxides as precursors to lithiated oxides and it could result in a more homogenous precipitation with the possibility to obtain a smaller particle size distribution, since the nucleation step can be separated from particle growth. In the traditional co-precipitation method, the saturation of the precipitating agent is achieved rapidly. It leads to the continuous nucleation, growth and aggregation of particles, resulting in a precipitate with a wide size distribution [15].

The decomposition of urea was previously demonstrated to be a successful precipitation route to metal carbonates [15], various hydroxide phases [16, 18] and, recently, Recham *et al.* used urea decomposition for the hydrothermal synthesis of $LiFePO_4$ [19]. The main difficulty with the

hydroxides, which were prepared previously utilizing the thermal decomposition of urea, is the complex phase that is obtained from the resultant product. The layered structure of these hydroxides favors the intercalation of ions and molecules within their structure. As a result, the structural analyses of the metal hydroxides prepared using this method is more complex than the traditional co-precipitation method. Dixit *et al.* have reported on the synthesis of Co and Ni hydroxides from the decomposition of urea for application as electrode material in alkaline secondary batteries. In their work, it was found that the structure of the synthesized α-hydroxides contained many intercalated $NH_3$ molecules [18].

Three different techniques were used in this investigation to achieve the required temperature for urea decomposition: hydrothermal, microwave assisted hydrothermal and reflux. These routes provide a large range of parameters, such as temperature, pressure, atmosphere, pH and reagents concentration that can be tuned during the synthesis of the hydroxides. The varieties of parameters that can be tuned represent an advantage over traditional methods towards the preparation of more dense particles. In this report, the first method for the synthesis of the hydroxides involved applying a hydrothermal treatment within an auto-clave at 180 °C for 5 hours. The second method used a microwave assisted hydrothermal procedure at 180 °C for 15 minutes and, for the third, the solutions were set to reflux at 100 °C for 5 hours. All hydroxides were prepared in a range of stoichiometry from $x$ = 0.00 to 0.50 in $Ni_xMn_xCo_{(1-x)}(OH)_2$. The particle size and morphology were compared to samples prepared by the

traditional co-precipitation method. The oxidation of the hydroxide by air in the presence of a lithium salt produced a phase pure lithium metal oxide sample with the as-expected $R\bar{3}m$ structure.

## *4.2 Experimental*

### 4.2.1 Preparation

$Co(NO_3)_2.6H_2O$ (98%), $Ni(NO_3)_2.6H_2O$ (98%), $Mn(NO_3)_2.6H_2O$ (98%), $NH_2CONH_2$, and $LiOH.H_2O$ (98%) (Aldrich) were used as starting materials and all solutions were prepared in distilled and degassed water. $Ni_xMn_xCo_{(1-2x)}(OH)_2$ ($x$ = 0.00, 0.05, 0.15, 0.30, 0.45 and 0.50) were prepared by a precipitation method based on the thermal decomposition of urea. An aqueous solution containing the mix metal salts with the desired stoichiometry (0.4 M) and $NH_2CONH_2$ (1.2 M) was prepared and stirred for several minutes. The initial pH value was ~ 5. Three different routes were developed to achieve the temperature for the thermal decomposition of urea and subsequent precipitation of the hydroxides. The first route consisted of a hydrothermal treatment in which the aqueous solution of the metal salts and urea was transferred into a Teflon container and placed within a sealed digestive vessel (Parr). The vessel was then placed in an oven at 180 °C for 5 hours. In the second route a microwave assisted hydrothermal treatment was applied. Here, the solution was sealed in

closed Teflon liners, which were placed in a turntable for uniform heating within a microwave digestion system (MARS5, CEM). The system operated at a frequency of 2.45 GHz and a power of 1200 W. The temperature of the microwave was ramped rapidly to 180 °C and kept under these hydrothermal conditions for 15 min. For the third route the aqueous solution was heated under reflux conditions at 100 °C for 5h. The pH at the end of all of these reactions was ~ 7. A traditional co-precipitation reaction was also prepared for comparison by following methods described previously in the literature (metal solution dripped slowly into a solution of high pH) [7, 13]. In all cases the precipitate was rinsed several times with distilled water and dried overnight under dry air. The final lithiated oxide, $LiNi_xMn_xCo_{(1-2x)}O_2$, was prepared by mixing the dry hydroxide precursors with an excess (3%) amount of LiOH. After pelletizing, it was heated in air at 500 °C for 3 h, ground, a new pellet formed, and then heated at 900 °C for 3 h followed by a quench cooling (between large copper plates).

### 4.2.2 Characterization

The crystalline phases of samples were determined by X-ray diffraction (XRD, Bruker D8 Advance) using Cu Kα radiation with a step size of 0.025° and step time of 15 s in the range of 15 to 60° or 20 to 80°. The lattice parameters were refined through Rietveld analysis using the integrated X-ray

powder diffraction software package TOPAS Version 3.0. An elemental analysis was carried out on all samples (EAS 1108, Fisions Instruments).

Scanning Electron Micrographs (SEM) were carried out on a Hitachi S-4300 microscope. TGA measurements were performed under a flowing He gas with a TA Instrument thermogravimetric analyser (SDT600) at 15 °C/min from room temperature to 500 °C. Electrochemical evaluations on the lithium metal oxide were performed by combining the oxide with 10% of a conductive carbon (Super-P Li, Timcal) and 10% polyvinylidene difluoride (PVDF, 5.5% in N-methylpyrroldinone (NMP)) with an excess of NMP to make a slurry. The slurry (80% active) was deposited on a carbon coated Al foil using a doctor blade. The slurry was then dried at 70 °C and electrodes 13 mm in diameter were cut for cell assembly in standard 2032 coin-cell hardware (Hohsen) using a single lithium metal foil as both counter and reference electrode and a Celgard 2200 separator. Cells were assembled in an argon-filled glove box using 1M $LiPF_6$ in ethylene carbonate (EC)/ diethyl carbonate (DEC) (3:1 by vol) electrolyte (UBE). Electrochemical evaluations were performed by charging and discharging between 2.2 and 4.2 V using a current rate of 5 mA $g^{-1}$ for the first 5 cycles and a current of 30 mA $g^{-1}$ for the next 50 cycles at 30 °C on a BT-2000 electrochemical station (Arbin).

## *4.3 Results and Discussion*

### 4.3.1 Co-precipitation of mixed metal hydroxides based on the thermal decomposition of urea

A solution, which contains urea ($NH_2CONH_2$) at room temperature, has a pH value of about 5. An increase in the pH of the solution is observed at elevated temperature as urea begins its decomposition near 90 °C [19]. Urea decomposes yielding $NH_3$ into the reaction medium and the pH of the solution increases. Here, the elevated temperature was achieved through three different heating methods and then applied towards the synthesis of $Ni_xMn_xCo_{(1-2x)}(OH)_2$ hydroxides with a stoichiometry of $x = 0.00$ to 0.50.

Figure 4.1 shows the X-ray diffraction pattern of all hydroxides obtained with the three different precipitation techniques. We can observe the formation of numerous Bragg diffraction peaks that cannot be indexed with the theoretical pattern expected and demonstrated previously in the literature for $Ni_xMn_xCo_{(1-2x)}(OH)_2$. This difference is related to the layered structure of the hydroxide and the nature of the urea decomposition. As urea decomposes at elevated temperature it produces numerous ions and molecules (products include $CNO^-$, HNCO, $CO_2$, $HCO_3^-$, $NH_4^+$ and $NH_3$) [15-17]. This complex decomposition scenario can cause the precipitation of metals in forms other than hydroxides or the incorporation of these various ions within the interlayer spacing of the hydroxide. In any event, we can see interesting features from the

XRD patterns shown in Figure 4.1. If we consider the hydrothermally precipitated material (black lines in Figure 4.1), there is the loss of several peaks as $x$ values increase over 0.05. When the concentration of Ni and Mn are higher than Co ($x \geq 0.30$) all peaks seem to be split in two. In general, the crystallinity of the material improves with the time spent at elevated temperatures. In Figure 4.1, the more intense and well-defined peaks are obtained from the hydrothermally precipitated samples (black line in Figure 4.1) compared to samples precipitated with the assistance of microwave (red line in Figure 4.1). It is even clearer when compared to samples prepared under reflux (blue line in Figure 4.1). The complicated diffraction pattern and numerous structural possibilities of these samples have hindered their complete structural characterization. For the sake of simplicity, the samples will continue to be named hydroxides for the remainder of the manuscript although they are likely to contain a mixture of hydroxides with various intercalated species.

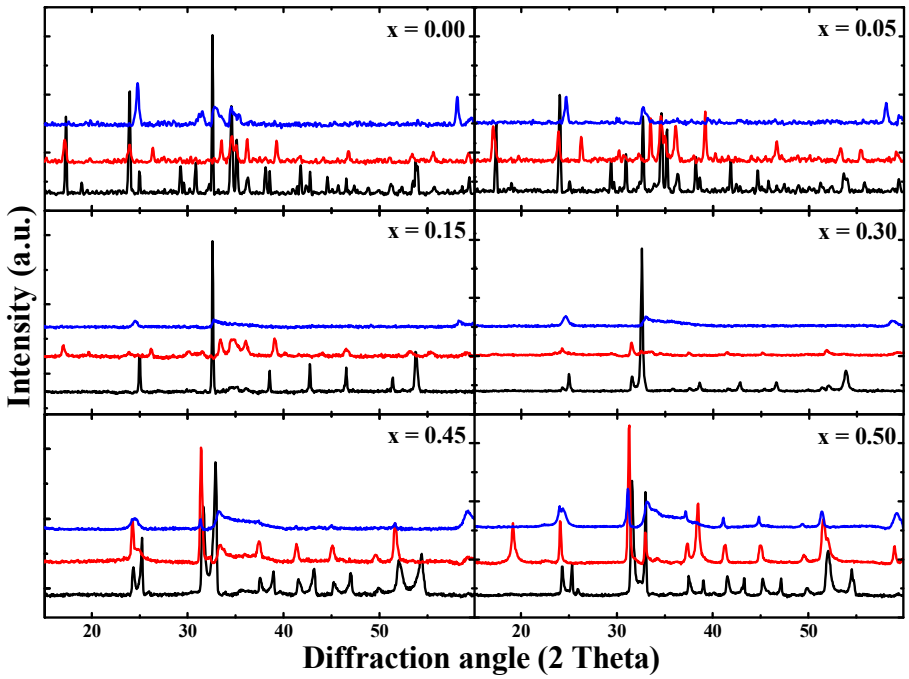


***Figure 4.1**: XRD profiles of $Ni_xMn_xCo_{(1-2x)}(OH)_2$, synthesis based on urea decomposition for the indicated value of x. (bottom black line = under hydrothermal conditions; middle red line = microwave assisted hydrothermal and top blue line = reflux).*

We believe that prolonged exposure to elevated temperatures eliminates structural defects that are readily apparent at shorter reaction times, thus hydrothermal syntheses were performed with a longer reaction time of 24 hours. Figure 4.2 shows the XRD diffraction pattern obtained from samples with $x$ = 0.00, 0.30 and 0.50 when reacted under hydrothermal conditions for 24 hours. These can be compared to those shown in Figure 4.1 where the synthesis took place over 5 hours. As the samples are exposed to elevated temperature for longer periods of time, several of the Bragg peaks disappeared, while others

become more well defined, indicating a reduction in defects as compared to the samples in Figure 4.1.

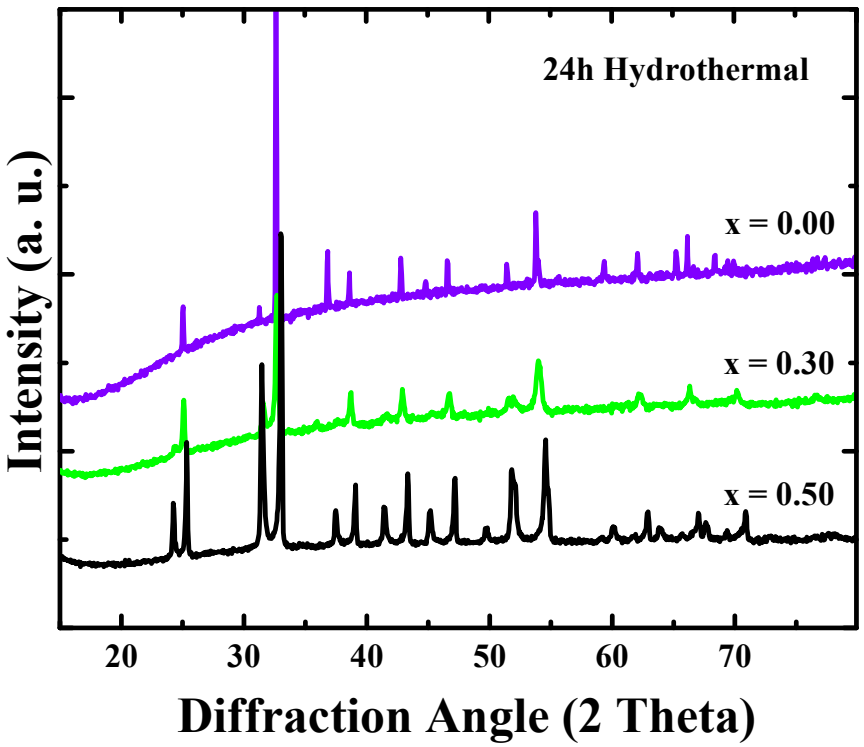


***Figure 4.2:*** *XRD profiles of $Ni_xMn_xCo_{(1-2x)}(OH)_2$ synthesized using the decomposition of urea under hydrothermal conditions for 24 hours.*

In order to aid in the structural identification of the obtained material, a heating step was performed within a thermogravimetric analyzer. Samples were heated to 500 °C within the TGA under a He atmosphere. According to the TGA results (Figure 4.3), the synthesized hydroxides decompose in one stage near 400 °C, independent of the stoichiometry of the hydroxide. Thus, we assume that the water and any intercalated ions are removed at the same time. Figure 4.4

shows the XRD diffraction pattern after the TGA. When $x = 0.00$, there is the formation of a pure CoO phase, as shown in the XRD. As Ni and Mn are introduced into our samples (increasing $x$) and heated to 500°C in He there is a change in the diffraction pattern to what is probably a mixture of CoO, MnO and NiO phases [18, 20-21]. When $x = 0.45$ the diffraction pattern presents a significant change compared to samples with $x < 0.45$ and its main peaks are related to the formation of NiO and MnO. This result is expected as the molar ratio of Co in sample with $x >= 0.45$ is very small and will only result in a small amount of CoO. Dixit *et al.* observed similar diffraction patterns for nickel hydroxide heated in He atmosphere as that presented here [18]. It is interesting to note that the weight loss increases with the amount of Ni and Mn in the sample (Figure 4.3), while the temperature of decomposition is only slightly affected. This demonstrates that hydroxides with a higher content of Ni and Mn have a higher content of intercalated ions or molecules. Only two samples are presented in Figure 4.3 for simplicity, but the other samples do not deviate from the trend shown.

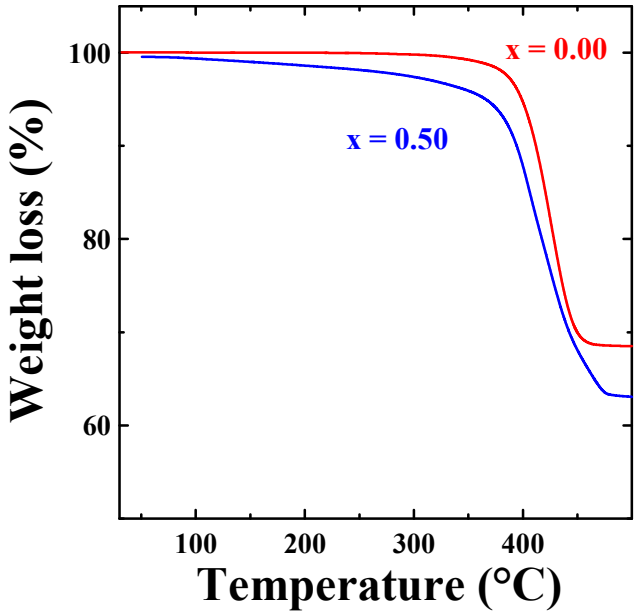


***Figure 4.3:*** *TGA measurements (15 °C/ min) for $Ni_xMn_xCo_{(1-2x)}(OH)_2$ synthesized using the decomposition of urea via the hydrothermal method (top red line x = 0.00; bottom blue line x = 0.50).*

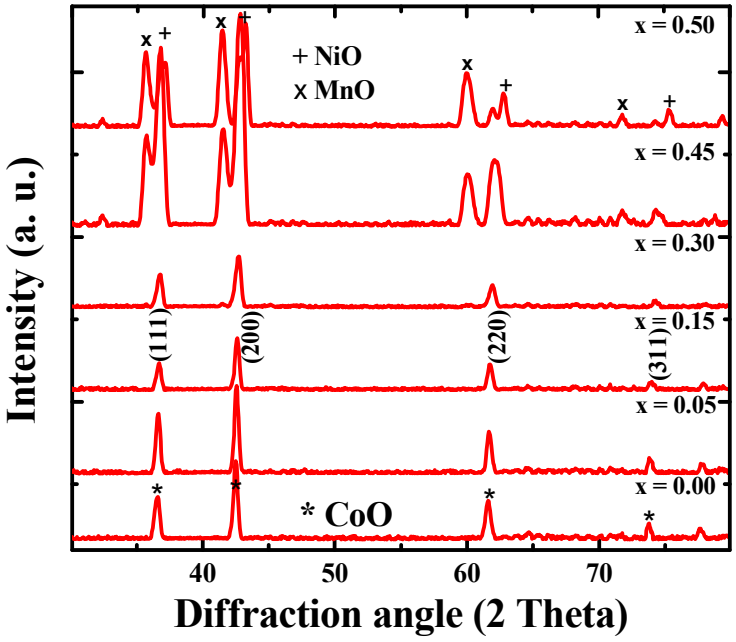


***Figure 4.4:*** *XRD profiles of $Ni_xMn_xCo_{(1-2x)}(OH)_2$ synthesized using the decomposition of urea via hydrothermal conditions after heating to 500°C in He.*

A comparison between the TGA profiles of the hydroxides prepared by the traditional co-precipitation method and that based on the thermal decomposition of urea (hydrothermal) is shown in Figure 4.5 (for $x = 0.00$). The weight loss is significantly increased for the sample originating from the urea precipitation compared to the traditional co-precipitation method. This is due to the larger amount of intercalated water and/or ions within the sample synthesized using the decomposition of urea. According to the TGA results, samples prepared with urea decompose at ~ 400 °C (Figure 4.5a) while samples prepared by the traditional co-precipitation method decompose at ~ 200 °C. The weight loss in both samples is associated with the release of absorbed water, conversion of the hydroxides into oxides and decomposition of ions and/or molecules intercalated within the hydroxides layers. The interlayer species are more tightly bound within the hydroxides layers of the samples precipitated from the thermal decomposition of urea resulting in improved thermal stability for these samples. This increase in thermal stability with the binding of interlayer species in hydroxides is common and has been described before [22-24].

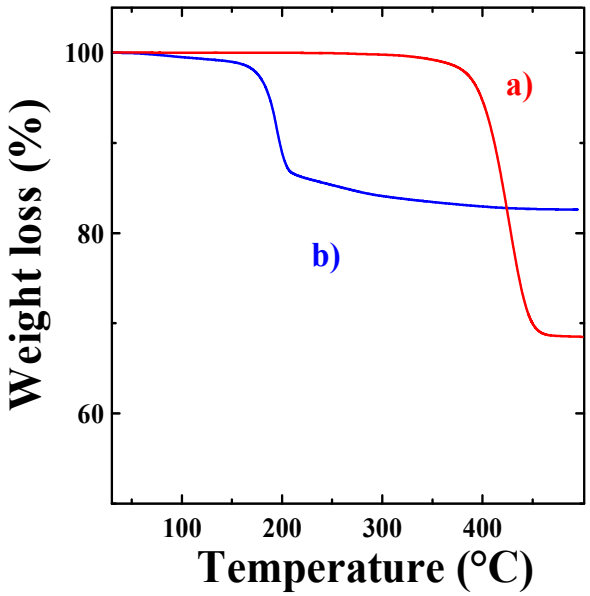


***Figure 4.5:*** *TGA measurements (15 °C/ min) for $Ni_xMn_xCo_{(1-2x)}(OH)_2$ synthesized using the decomposition of urea via the hydrothermal method (top red line); and synthesized by the traditional co-precipitation method (bottom blue line) (x = 0.00).*

Table 4.1 shows the results of the elemental analysis on the hydrothermally precipitated hydroxide samples to demonstrate the presence of intercalated ions and/or molecules within the layered hydroxide. The presence of $NH_3$ within similar materials has been reported previously in the literature [18]. The amount of nitrogen within these hydroxides increases as *x* increases to 0.50, which is in agreement with the increase in weight loss as observed in the TGA experiments when *x* increases to 0.50. Hydroxides prepared through the traditional co-precipitation method have a smaller content of nitrogen when compared to the hydroxides, of the same composition, prepared through the thermal decomposition of urea. The presence of nitrogen is even smaller if we

compare them to the samples prepared by the traditional co-precipitation method using a hydrothermal post-synthetic treatment. The nitrogen present in the sample prepared by the traditional method comes from the nitrate in the precursor metal salts. Thus, we can consider that the increase in nitrogen content of samples from urea decomposition compared to traditional method is due to the presence of $NH_3$ generated by the decomposition of urea. The carbon content was also analyzed. The difference between the carbon content for samples prepared by the traditional method compared to the urea based samples is even more pronounced than with nitrogen. If we consider samples with a stoichiometry of $x = 0.50$, a carbon content of 8.6% is obtained for the sample prepared with urea compared to 0.02% (detection limit of our machine) for the samples prepared by a traditional co-precipitation method followed by a hydrothermal post-synthetic treatment. The higher amount of carbon likely originates from ions and molecules intercalated into the hydroxides (*ex.*: $CO_2$, $HCO_3^-$ , NHCO and $NCO^-$) that are produced during the decomposition of urea. The elemental analysis provides valuable information about the possible ions and molecules intercalated within the hydroxides, however it is not possible to determine the exact composition of these species. Numerous different ions and molecules can be intercalated within the numerous samples prepared here and this is a likely reason as to why the amount of N, C and H measured for these samples are not increasing homogenously with increasing values of *x*.

***Tableau 4.1:*** *Amount (%) of nitrogen, carbon and hydrogen in samples prepared by hydrothermal precipitation.*

| | $x$ in $Ni_xMn_xCo_{(1-2x)}(OH)_2$ | N (%) | C (%) | H (%) |
|---|---|---|---|---|
| Urea decomposition under hydrothermal conditions | 0.00 | 0.02 | 7.10 | 0.62 |
| | 0.05 | 0.04 | 6.41 | 0.76 |
| | 0.15 | 0.05 | 9.93 | 0.19 |
| | 0.30 | 0.07 | 9.71 | 0.22 |
| | 0.45 | 0.14 | 8.78 | 0.58 |
| | 0.50 | 0.14 | 8.62 | 0.64 |
| Traditional co-precipitation | 0.50 | 0.06 | 0.00 | 0.36 |
| Traditional + hydrothermally treated | 0.50 | 0.01 | 0.02 | 1.24 |

Scanning electron microscopy (SEM) was used to determine the morphology of the samples. Figure 4.6 shows images of hydroxides obtained with the hydrothermal/urea technique. When $x$ = 0.00 and 0.05 a clear layered morphology is visible. This trend tends to change to larger square particles when $x$ = 0.30 and 0.45 and finally at $x$ = 0.50, the square particles become covered by fine needle like particles in a pattern that can suggest a biphasic material, however, more detailed analysis would be necessary to clarify this point. All the hydroxides shown in Figure 4.6 have a larger particle size when compared to the samples prepared by the traditional co-precipitation method without any post-synthetic treatment [8, 14].

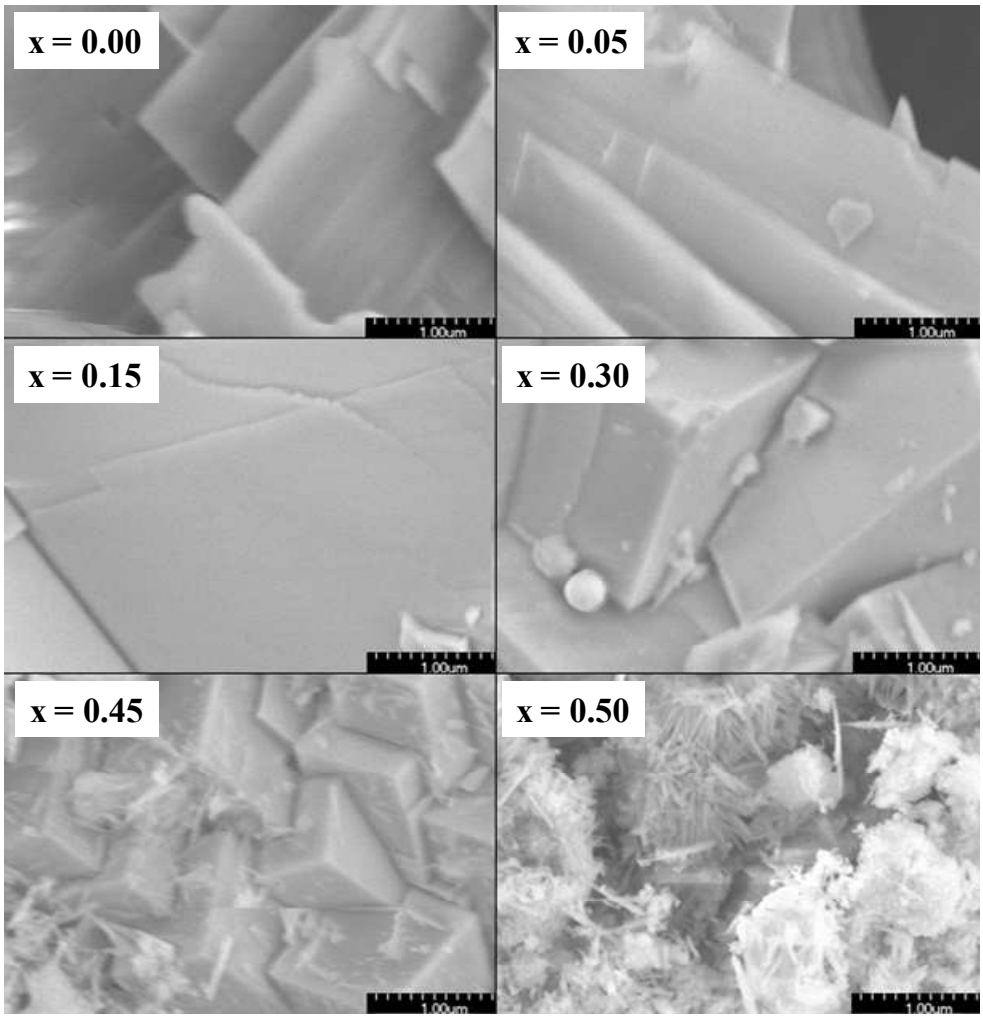


***Figure 4.6:*** *SEM images of $Ni_xMn_xCo_{(1-2x)}(OH)_2$ synthesized using the decomposition of urea via the hydrothermal method.*

Figures 4.7 and 4.8 show the SEM images of the samples prepared with the microwave assisted hydrothermal and reflux techniques, respectively.

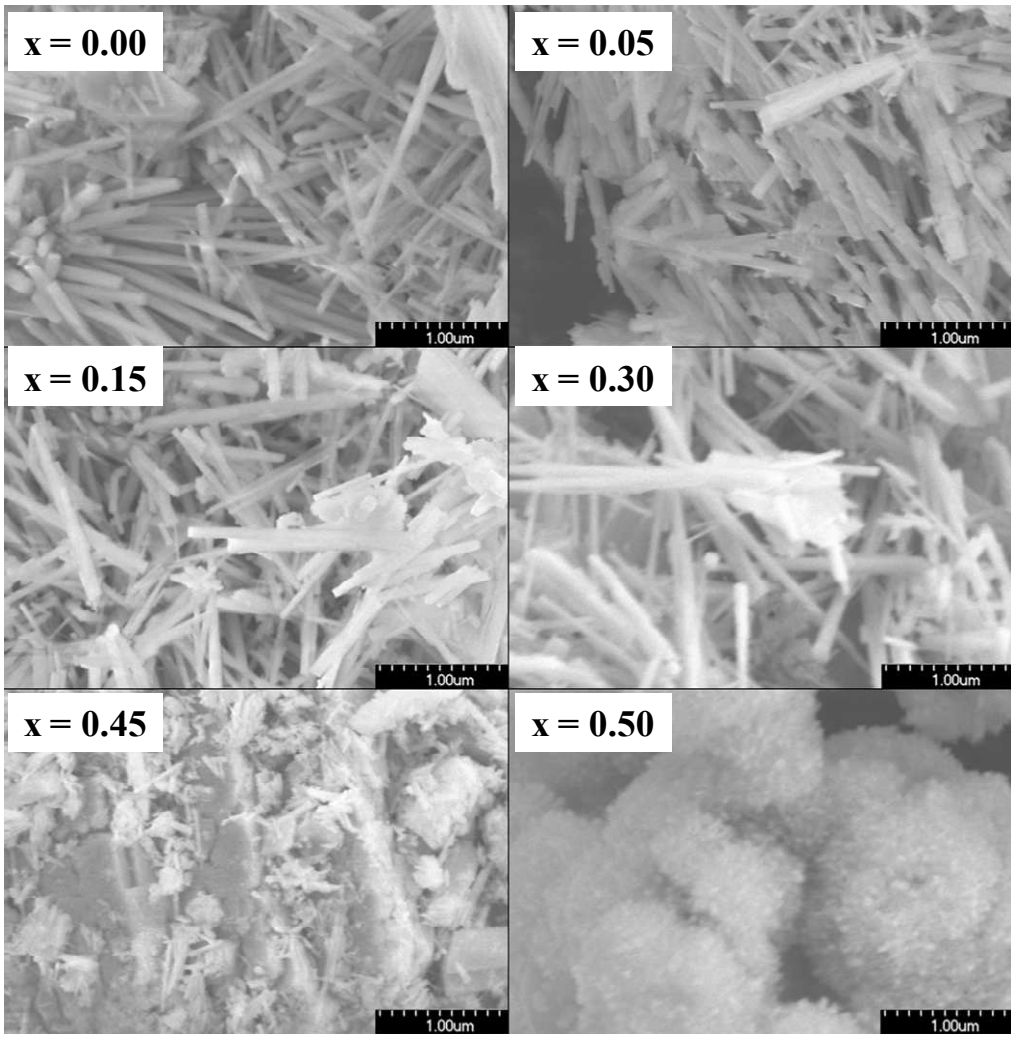


***Figure 4.7:*** *SEM images of $Ni_xMn_xCo_{(1-2x)}(OH)_2$ synthesized using the decomposition of urea under microwave assisted hydrothermal conditions.*

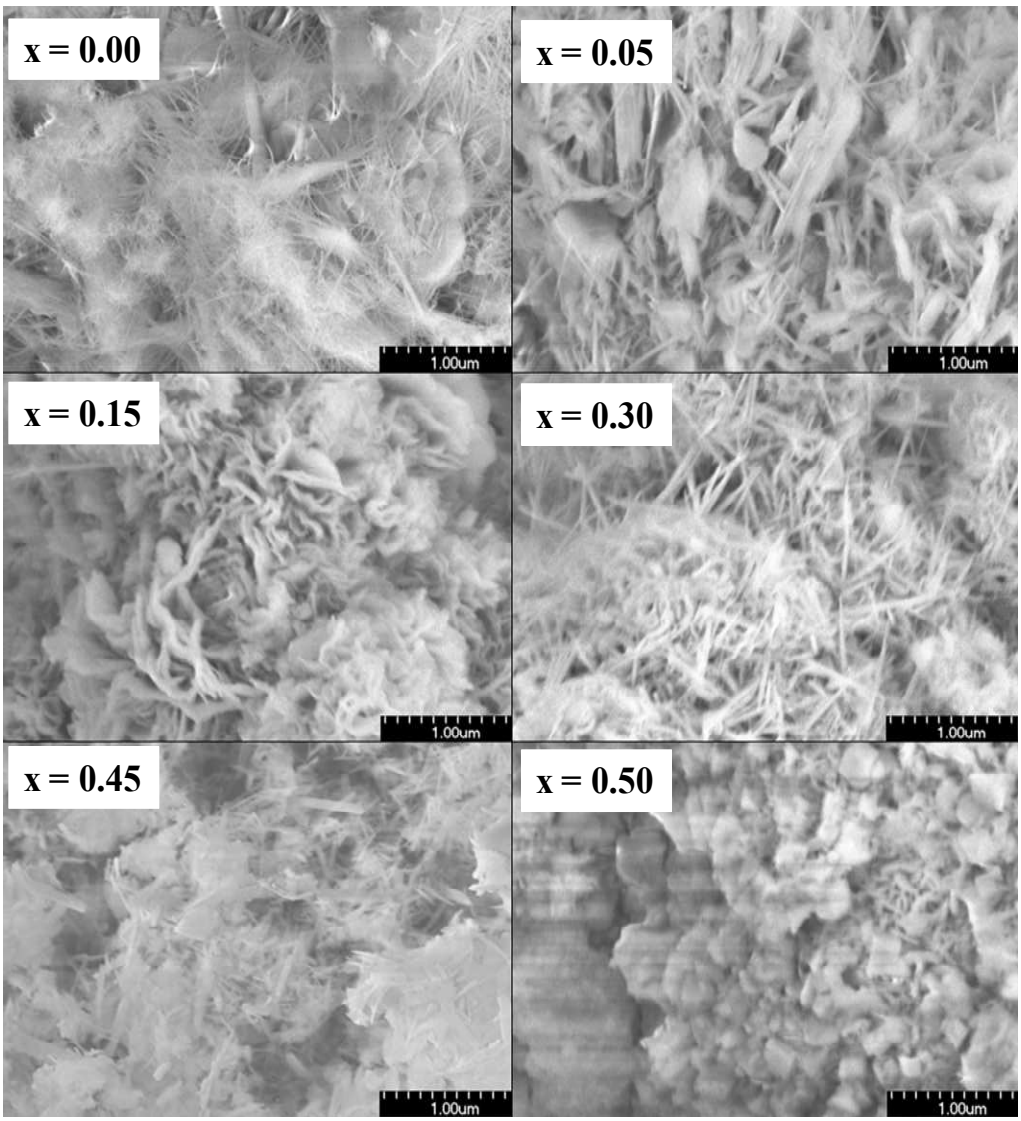


***Figure 4.8:*** *SEM images of $Ni_xMn_xCo_{(1-2x)}(OH)_2$ synthesized using the decomposition of urea under reflux conditions.*

The hydroxides synthesized from these methods have a much smaller particle size than those presented in Figure 4.6. The samples from the microwave assisted synthesis (Figure 4.7) from $x$ = 0.00 to 0.30 have a very well formed needle morphology while at $x$ = 0.45 and 0.50 the needles disappear and a more random morphology is observed. The hydroxides synthesized under

reflux conditions (Figure 4.8) do not present a well formed morphology. The lack of well formed particles, is directly related to the XRD results presented in Figure 4.1 where a well formed crystallized product is observed for the hydrothermal samples but there is a loss in crystallinity for the samples synthesized using either the microwave or reflux methods.

In Figure 4.9, we compare the images of the samples ($x$ = 0.30) from the three different heating techniques at two different magnification. Particles obtained from the hydrothermally prepared samples (Figure 4.9a) are much larger when compared to either the microwave (Figure 4.9b) or reflux (Figure 4.9c) method. The increase in particle size is due to the increase in time at high temperature. The time at higher temperature also plays an important role in the crystallinity of the final material, as observed in Figure 4.1. On the right side of the Figure 4.9a we present a smaller magnification level to provide a better view of the general morphology of the agglomerates. We can see that all hydroxides, regardless of preparative method, present a spherical global morphology. The microwave and reflux techniques generate a cotton ball morphology formed by the agglomeration of many fine needle like particles while the large spherical morphology from the hydrothermal method is formed by the agglomeration of the much larger square particles.

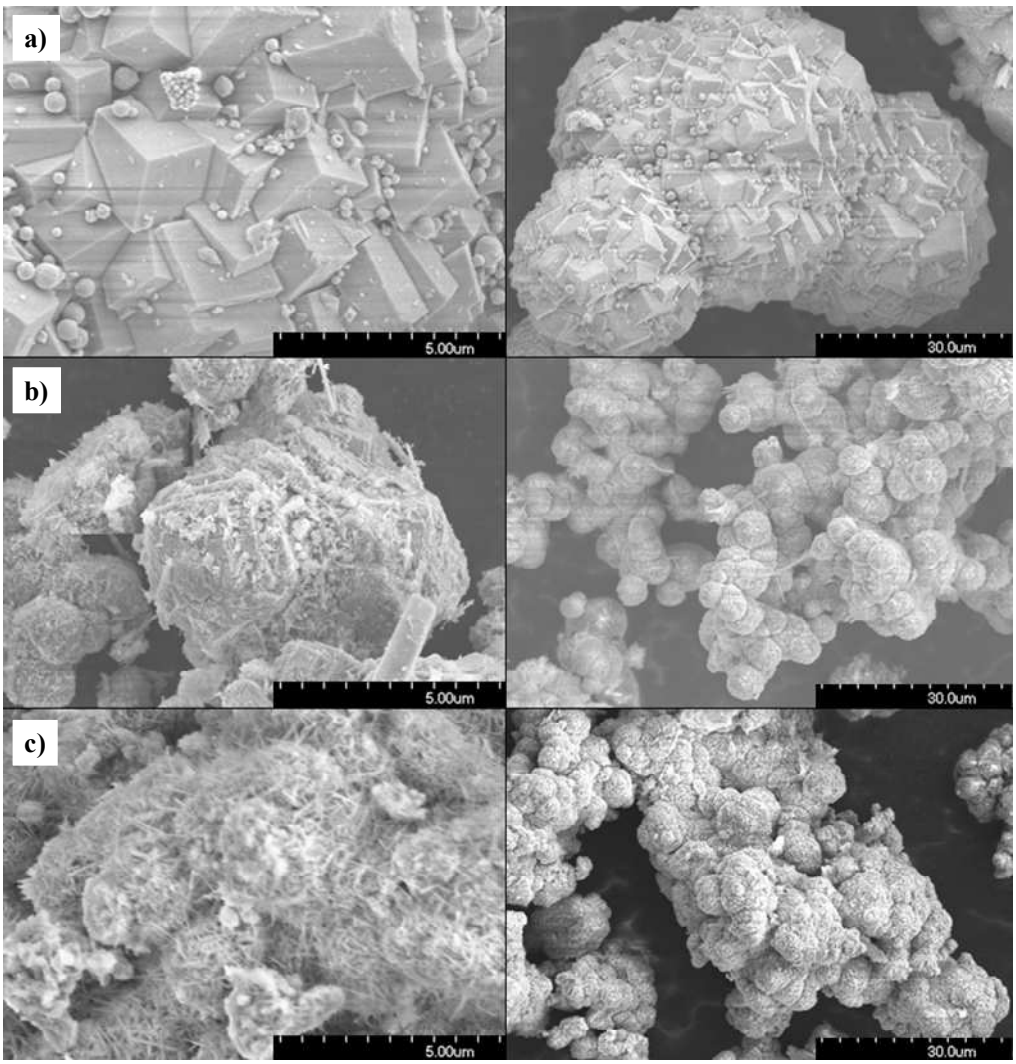


***Figure 4.9:*** *Comparison of particle size and morphology for* $Ni_xMn_xCo_{(1-2x)}(OH)_2$. *(a) Prepared under hydrothermal conditions; (b) microwave assisted hydrothermal conditions and (c) reflux conditions. Left column scale bar of 5 μm and right column of 30 μm, x = 0.30.*

Previous work on hydroxides prepared by the traditional co-precipitation method demonstrated how the stoichiometry of the sample has an important impact on the oxidation degree of the material [27]. The oxidation of the hydroxides occurs upon exposure to air (either during or after synthesis). During

the oxidation process the color of the samples change to light brown independent of the value of $x$. Figure 4.10a presents a photograph of the hydroxide samples using the decomposition of urea assisted by reflux conditions. Interestingly, many colorful samples are obtained after rinsing, in contrast with samples prepared by the traditional co-precipitation. This is likely due to the intercalation of a number of species within the sample that affect the absorption of light by the sample. It was previously shown that the oxidative process becomes significant in samples with $x \geq 0.30$. A reduction of the oxidation is possible by controlling the atmosphere during reflux. In Figure 4.10b, a photograph of a sample ($x = 0.30$) synthesized under conditions using an overflow of Ar is shown. The sample demonstrates a pink colour compared to the blue colour when synthesized under uncontrolled atmospheric conditions.

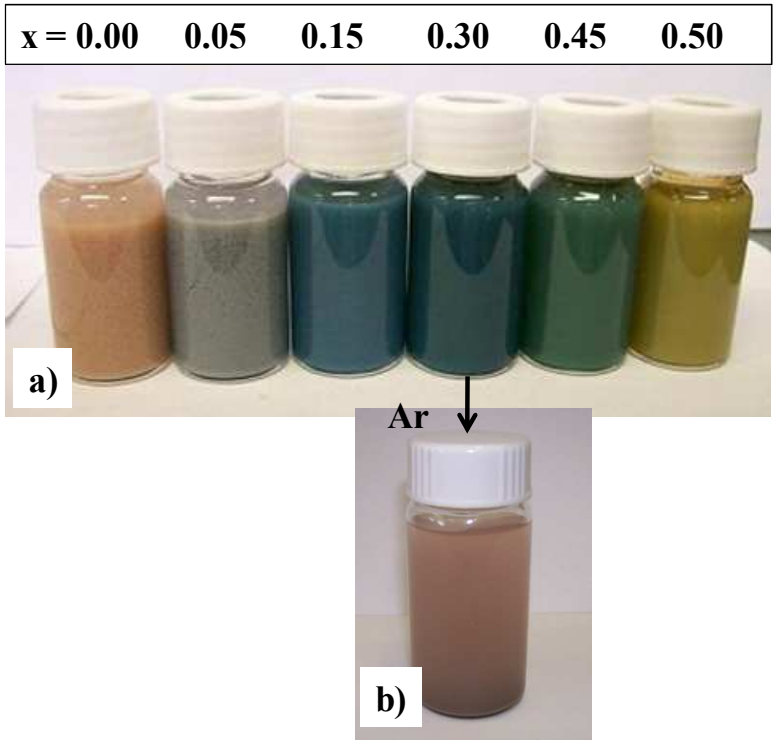


***Figure 4.10:*** *Photograph of the solutions containing $Ni_xMn_xCo_{(1-2x)}(OH)_2$ (x = 0.00 to 0.50) prepared under reflux conditions without any atmospheric controls in a) and in (b) for $Ni_xMn_xCo_{(1-2x)}(OH)_2$ (x = 0.30) synthesized using reflux conditions under a purge of argon.*

### 4.3.2 Lithium mixed metal oxides

For application within lithium-ion batteries, these mixed metal hydroxides need to be oxidized into lithiated oxides. It has been found previously that the morphology of the precursor hydroxide has a significant effect on the ability to produce the optimal dense, spherical lithiated oxides [2, 8-9]. Thus, it is important to fully investigate various synthetic methods for the

synthesis of these hydroxides such that one can obtain dense oxides, which will lead to dense electrodes and higher energy density batteries. The lithiated oxides were prepared by reacting the precursor hydroxides with a slight excess of LiOH (3%) in air at 500 °C for 3 hours followed by re-grinding and heating to 900 °C for 3 hours with a quench cooling step. Figure 4.11 shows the XRD patterns of the oxides produced from the various hydroxide precursors described above.

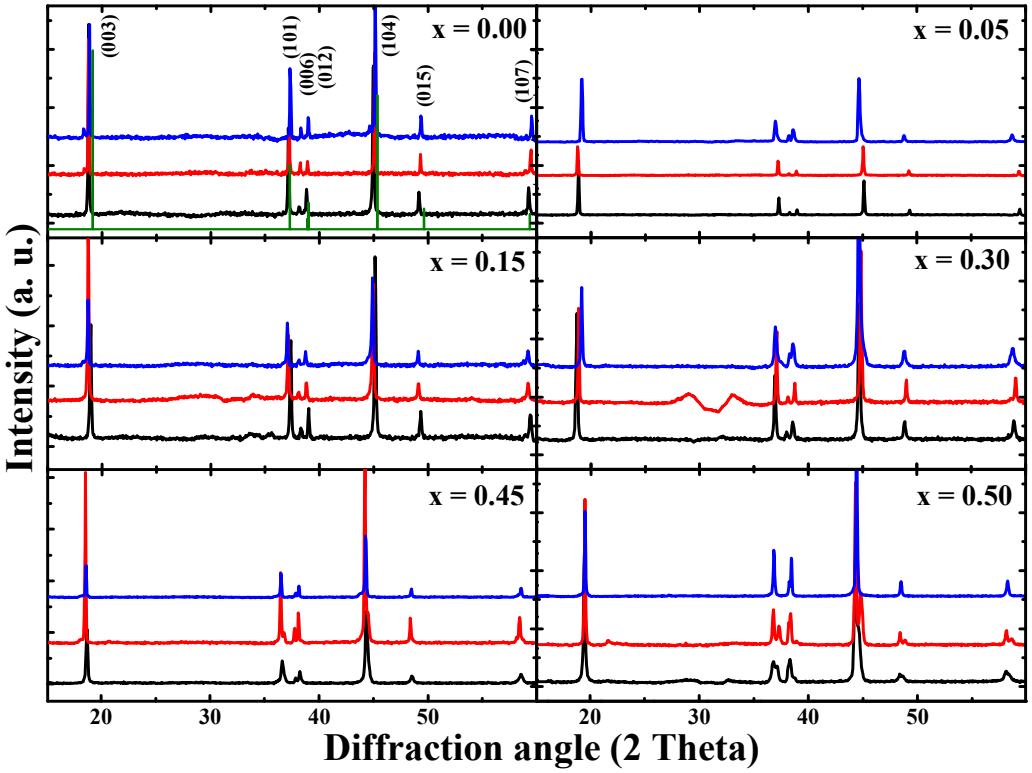


***Figure 4.11:*** *XRD profiles of $LiNi_xMn_xCo_{(1-2x)}O_2$. (bottom black line = from precursor prepared under hydrothermal conditions; middle red line = from precursor prepared under microwave assisted hydrothermal conditions, top blue line = from precursor prepared under reflux conditions and the green lines in the x = 0.00 quadrant is a representation of the Bragg peaks, with indicated Miller indices, for $LiCoO_2$ that can be used as a reference.*

The obtained powder patterns (Figure 4.11) compare well with those quote in the literature for $LiNi_xMn_xCo_{(1-2x)}O_2$ phases. Thus, the novel synthesis approach for the co-precipitation of hydroxides precursors does not seem to affect the structure or crystalinity of the oxides despite the presence of intercalated ions and molecules within our hydroxides. Table 4.2 presents the lattice parameters of all the oxides indexed using the α-$NaFeO_2$ type structure (trigonal $\overline{R3m}$). As expected, with increasing Mn and Ni concentration, the *a* and *c* lattice parameters as well as the unit cell volume V increases with the value of *x* in all cases which is not surprising as the of the ionic radius of the substituted $Ni^{2+}$ (0.69 Å) ions are higher than that of $Co^{3+}$ (0.54 Å) [25-27]. The ionic radius of $Mn^{4+}$ (0.53 Å) is about the same size as that of $Co^{3+}$ and therefore the increase in the lattice parameters of $LiNi_xMn_xCo_{(1-2x)}O_2$ when *x* increases is due to the insertion of $Ni^{2+}$ and $Mn^{4+}$ into the lattice, which was previously reported in the literature [24]. The lattice parameters of oxides, prepared with precursors from the microwave and reflux method, are larger compared to those from the hydrothermally prepared samples. This is in agreement to the increased disorder seen with the precursor hydroxides from the microwave and reflux reactions in Figure 4.1.

Figure 4.12 shows the SEM images of the $LiNi_xMn_xCo_{(1-2x)}O_2$ prepared from hydroxide precursors based on the urea decomposition using the hydrothermal method (Figure 4.12a), microwave assisted hydrothermal (Figure 4.12b) and reflux (Figure 4.12c) methods. Each sample is shown with two

different magnifications (left: scale bar 5 μm and right scale bar 30 μm) ($x$ = 0.30). While the particle size of the precursor hydroxides showed a significant increase for the urea decomposition under hydrothermal conditions with respect to the other methods, the particle size of all oxides, regardless of the particle size of the precursor, are similar, but the particles from the hydrothermal method tend to agglomerate into larger agglomerates.

***Table 4.2:*** *Lattice parameters and cell unit volume of* $LiNi_xMn_xCo_{(1-2x)}O_2$, *indexed using the* $R\bar{3}m$ *space group.*

| | $x$ in $LiNi_xMn_xCo_{(1-2x)}O_2$ | $a$ (Å) | $c$ (Å) | V (Å$^3$) |
|---|---|---|---|---|
| Hydrothermal | 0.00 | 2.859 | 14.230 | 100.7 |
| | 0.05 | 2.864 | 14.258 | 101.3 |
| | 0.15 | 2.867 | 14.274 | 101.6 |
| | 0.30 | 2.870 | 14.277 | 101.8 |
| | 0.45 | 2.876 | 14.279 | 102.3 |
| | 0.50 | 2.893 | 14.284 | 103.5 |
| MW-Hydrothermal | 0.00 | 2.888 | 14.299 | 103.2 |
| | 0.05 | 2.892 | 14.298 | 103.6 |
| | 0.15 | 2.896 | 14.288 | 103.6 |
| | 0.30 | 2.897 | 14.299 | 103.9 |
| | 0.45 | 2.900 | 14.283 | 104.0 |
| | 0.50 | 2.905 | 14.309 | 104.6 |
| Reflux | 0.00 | 2.886 | 14.256 | 102.8 |
| | 0.05 | 2.886 | 14. 259 | 103.0 |
| | 0.15 | 2.890 | 14.269 | 103.2 |
| | 0.30 | 2.898 | 14.274 | 103.8 |
| | 0.45 | 2.908 | 14.285 | 102.2 |
| | 0.50 | 2.910 | 14.294 | 104.6 |

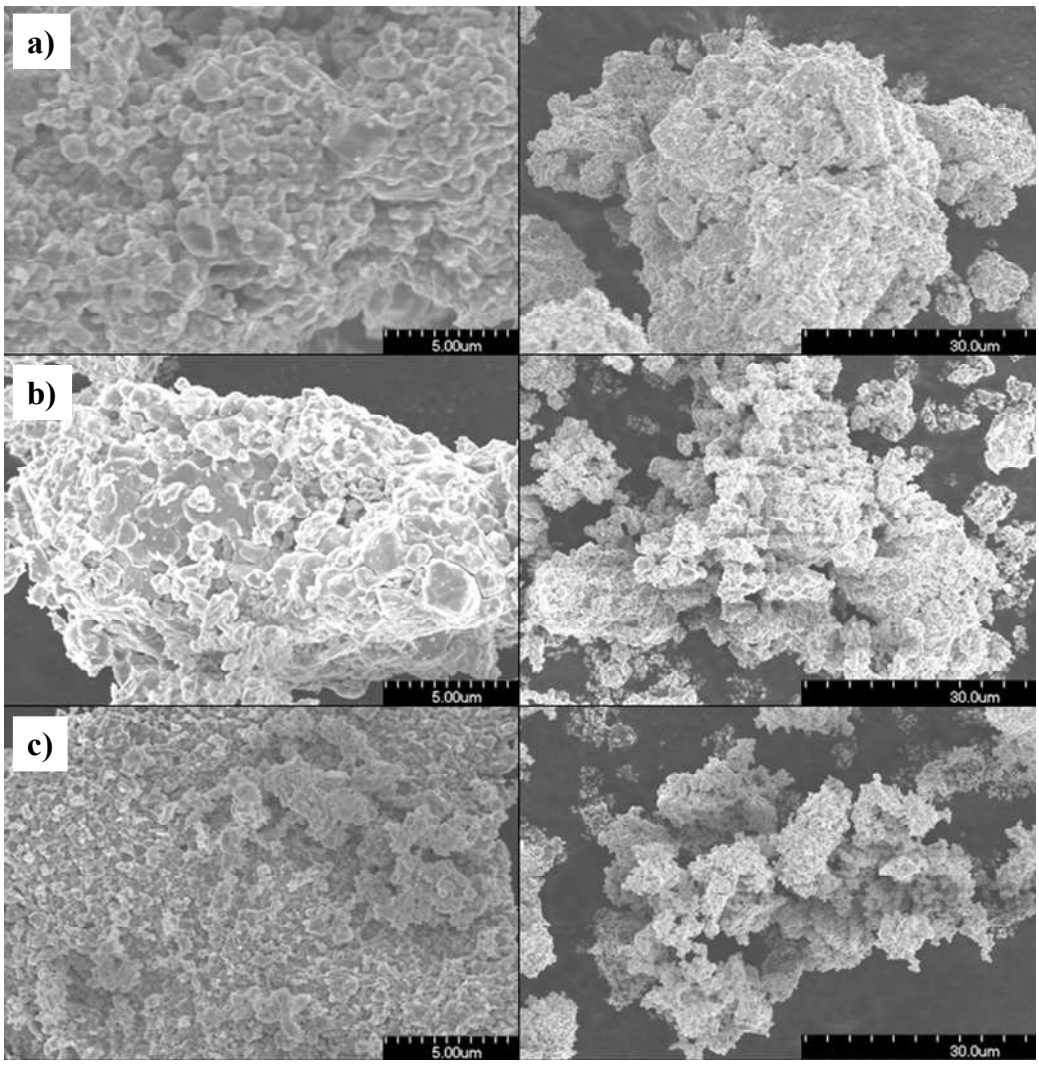


***Figure 4.12:*** *SEM images of $LiNi_xMn_xCo_{(1-2x)}O_2$ (x = 0.30) prepared with hydroxide precursors (a) prepared under hydrothermal conditions, (b) microwave assisted hydrothermal conditions and (c) reflux conditions. Left column scale bar of 5 µm and right column of 30 µm.*

The capacity retention (capacity *versus* cycle number), for the electrodes of oxides from precursors hydroxide based on urea decomposition for the three different heating techniques, is shown in Figure 4.13 for $x$ = 0.30 in $LiNi_xMn_xCo_{(1-2x)}O_2$: hydrothermal (black squares), microwave assisted

hydrothermal (red crosses) and reflux (blue *x*'s). The positive cathode material is cycled at 30 °C between 2.2 and 4.2 V. The first five cycles were charged at a rate of 5 mA $g^{-1}$, while the remaining cycles were charged at a rate of 30 mA $g^{-1}$. Electrodes prepared with oxides from precursors synthesized using the hydrothermal technique have higher capacity than the other heating methods. The same trend was found for all other values of *x*.

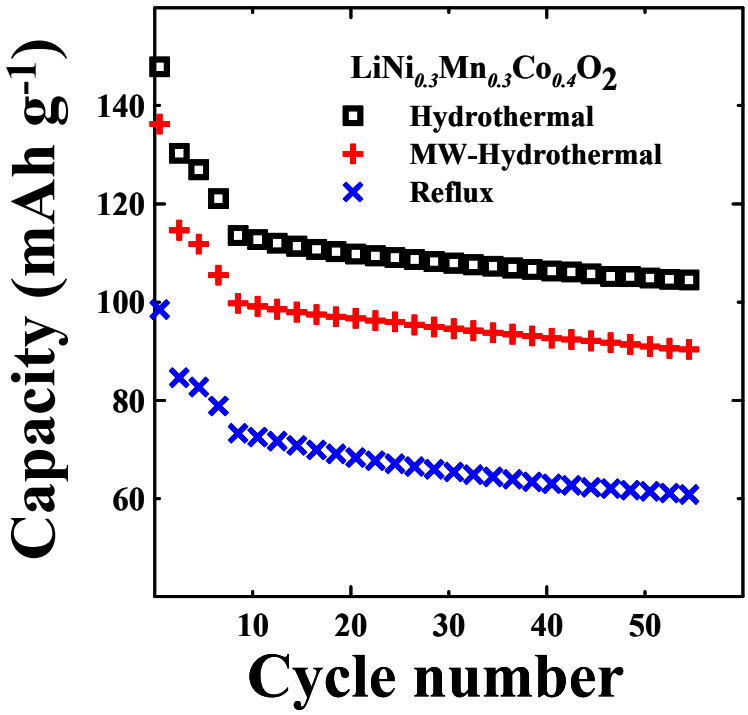


***Figure 4.13:*** *Capacity vs cycle number for $LiNi_xMn_xCo_{(1-2x)}O_2$ (x = 0.15) charged to 4.2V. Comparison of different methods used to achieve the required temperature to decompose urea. Hydrothermal condition (□ black); microwave assisted hydrothermal (+ red) and reflux (x blue). The charge-discharge curves consist of 5 cycles at a rate of 5 mA $g^{-1}$ followed by 50 cycles at 30 mA $g^{-1}$.*

Figure 4.14 presents electrochemical performance of the samples: prepared either by the traditional co-precipitation method or based on urea decomposition (hydrothermally prepared). The oxides prepared from precursors obtained using the decomposition of urea do not result in a large change in electrochemical performance as compared to the traditionally prepared co-precipitation precursors. The electrochemical results of the samples from urea decomposition with $x \geq 0.05$ are very similar to those obtained via the traditional co-precipitation method. Even though the capacity obtained from the urea samples was similar to the oxides prepared with traditional hydroxide precursors, we consider these results as promising as the precipitation based on the thermal decomposition of urea present numerous parameters (such as temperature, pH, time, etc…) that can be explored to improve various electrochemical properties (capacity, cycle life, tap density) of the final oxide. Further research into this reaction scheme will be initiated within our research group. The capacity of $LiCoO_2$ (from the traditional co-precipitation precursor) cycled at 4.2 V decreases drastically with increasing cycle number. This characteristic is typical of this material synthesized using the standard co-precipitation technique; but the synthesis of $LiCoO_2$ using the thermal decomposition of urea provides a significant improvement in capacity retention, but it shows a significant decrease in capacity when compared to commercial $LiCoO_2$ samples [14, 24].

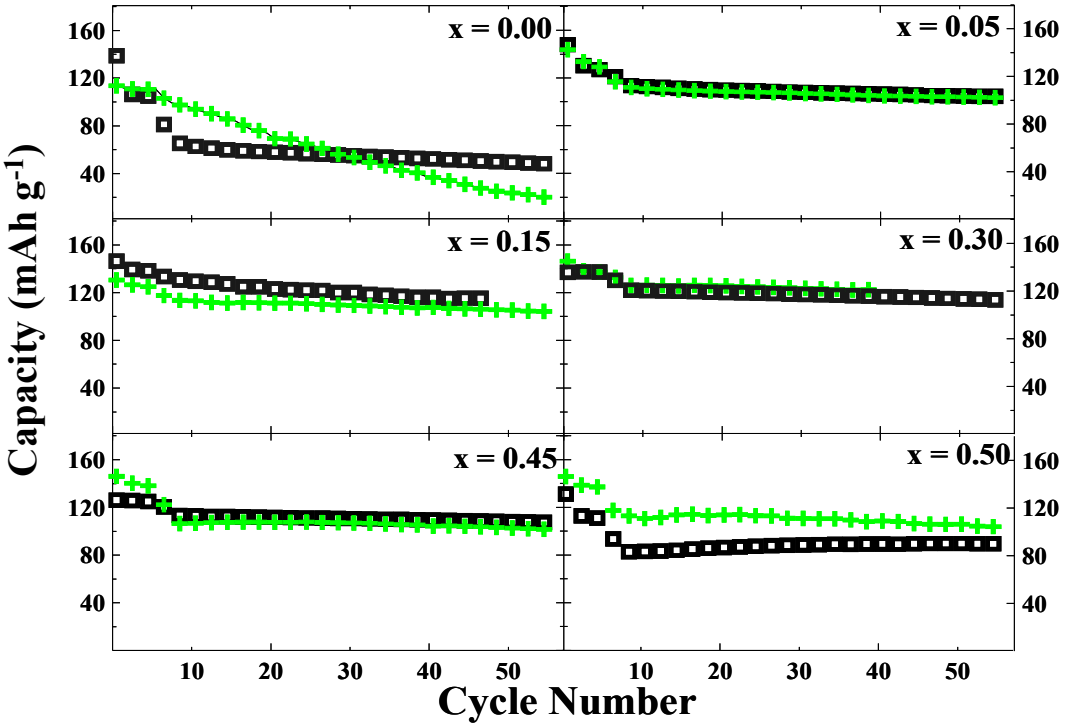


***Figure 4.14:*** *Comparison of the capacity vs cycle number for $LiNi_xCo_{(1-2x)}Mn_xO_2$ charged to 4.2V with hydroxides precursors prepared from the co-precipitation under hydrothermal conditions for the decomposition of urea (● black) to hydroxides prepared using the traditional co-precipitation method (+ green). The charge-discharge curves consist of 5 cycles at a rate of 5 mA $g^{-1}$ followed by 50 cycles at 30 mA $g^{-1}$.*

## *4.4 Conclusion*

$Ni_xMn_xCo_{(1-2x)}(OH)_2$ ($x$ = 0.00 to 0.50) were synthesized using a novel co-precipitation approach based on the thermal decomposition of urea. Three different techniques were used to achieve the required temperature to decompose urea leading to the precipitation of the mixed metal hydroxide: hydrothermal, microwave assisted hydrothermal and reflux. It is the first time that the precursors for mixed metal oxides have been prepared via a latent base. This method can provide an additional control towards the precipitation of the hydroxide and therefore the use of these controls could significantly improve the particle size and morphology of the mixed oxide samples. The controlled precipitation at elevated temperature could lead to a more homogenous precipitation of $Ni_xMn_xCo_{(1-2x)}(OH)_2$ compared to the traditional technique. The elevated temperature and pressure used during the precipitation represent additional parameters not available in the traditional method that could also improve the morphology of the hydroxides and increase the density of the final oxide. The density of hydroxide precursors has already demonstrated to be fundamentally important towards the preparation of denser oxides [11]. Therefore it is important to develop novel synthesis routes and treatments that optimize particle size and morphology.

The time at elevated temperature during synthesis has a significant impact on the crystallinity and morphology of the hydroxides. Samples which

were prepared using hydrothermal heating, show larger particle size and greater crystallinity. At longer reaction time (24 hours) the hydrothermally prepared samples demonstrate a decrease in the number of defects that are readily apparent in samples with reduced exposure time at high temperature. More experiments are needed to define the optimized scenario concerning synthesis parameters. Samples prepared with all methods and within all stoichiometry ranges were successfully used as precursor to electrochemically active lithiated mixed metal oxides ($LiNi_xMn_xCo_{(1-2x)}O_2$). Phase pure oxides, with very similar morphology regardless of the particle size and morphology of precursors, were obtained. The electrochemical properties of these samples presented characteristics similar to literature.

## *4.5 References*


**1.** Jouanneau, S.; Eberman, K. W.; Krause, L. J.; Dahn, J. R. *J. Electrochem. Soc.* **2003**, 150, A1637.

**2.** Zhou, F.; Zhao, X.; van Bommel, A.; Rowe, A. W.; Dahn, J. R. *Chem. Mater.* **2010**, 22, 1015.

**3.** Ohzuku, T.; Makimura, Y. *Chem. Lett.* **2001**, 30, 642.

**4.** Ohzuku, T.; Makimura, Y. *Chem. Lett.* **2001**, 30, 744.

**5.** Liu, Z.; Yu, A.; Lee, J. Y. *J. Power Sources* **1999**, 81-82, 416.

**6.** Lu, Z.; MacNeil, D. D.; Dahn, J. R. *Electrochem. Solid-State Lett.* **2001**, 12, A200.

**7.** Lu, Z.; Dahn, J. R. *J. Electrochem. Soc.* **2001**, 148, A237.

**8.** Barkhouse, D. A. R.; Dahn, J. R. *J. Electrochem. Soc.* **2005**, 152, A746.

**9.** Yabuuchi, N.; Koyama, Y.; Nakayama, N.; Ohzuku, T. *J. Electrochem. Soc.* **2005**, 152, A1434.

**10.** Nagaura, T.; Tozawa, K. *Prog. Batteries Solar Cells* **1990**, 9, 209.

**11.** van Bommel. A.; Dahn, J. R. *J. Electrochem. Soc.* **2009**, 156, A362.

**12.** van Bommel. A.; Dahn, J. R. *Chem. Mater.* **2009**, 21, 1500.

**13.** Zhao, X.; Zhou, F.; Dahn, J. R. *J. Electrochem. Soc.* **2008**,155, A642.

**14.** Rodrigues, I.; Wontcheu, J.; MacNeil, D. D. *submitted article* **2010**.

**15.** Vial, S.; Prevot, V.; Forano, C. *J. Phys. Chem. Solid* **2006**, 67, 1048.

**16.** Marvis, B.; Akinc, M. *J. Am.Ceramic. Soc.* **2006**, 89, 471.

**17.** Shaw, W. R.; Bordeaux, J. J. *J. Am. Chem. So.c* **1955**, 82, 4729.

**18.** Dixit, M.; Subbanna, G. N.; Kamath, P. V. *J. Mater. Chem*. **1996**, 6, 1429.

**19.** Recham, N.; Armand, M.; Laffont, M.; Tarascon, J-M. *Electrochem. Solid-State Lett*. **2009**, 12, A39.

**20.** Kosova, N. V.; Devyatkina, E. T.; Kaichev, V. V. *J. Power Sources* **2007**, 174, 735.

**21.** Kovanda, F.; Grygar, T.; Dornicak, V. *Solid State Sci.* **2003**, 5, 1019.

**22.** Wei, M.; Xu, X. Y.; He, J.; Rao, G. Y.; Yang, H. L. *J. Therm. Anal. Cal.* **2006**, 85, 795.

**23.** del Arco, M.; Carriazo, D.; Martín, C.; Grueso, A. M. P.; Rives, V. *Mater. Sci. Forum* **2006**, 514-516, 1541.

**24.** Barbosa, C. A. S.; Ferreira, A. M. D. C.; Constantino, V. R. L. *Eur. J. Inorg. Chem.* **2005**, 1577.

**25.** MacNeil, D. D.; Lu, Z.; Dahn, J. R. *J. Electrochem. Soc.* **2002**, 149, A1332.

**26.** Shannon, R. D. *Acta Crystallogr.* **1976**, A32, 751.

**27.** Jouanneau, S.; Dahn J. R. *Chem. Matt.* **2003**, 15, 495.

# Chapter 5

# Synthesis of lithium iron phosphate based on the thermal decomposition of urea

## *5.1 Introduction*

Lithium iron phosphate, $LiFePO_4$, was first reported as a positive cathode material for lithium-ion batteries by Padhi *et al*. in 1997 [1]. Since then, it has received a great deal of attention for the replacement of $LiCoO_2$ as the cathode material in lithium-ion batteries [1-3]. One of the main reasons for the large interest in $LiFePO_4$ is its high capacity (~ 170 mAh $g^{-1}$) at moderate current densities [1-4]. In addition, it is environmentally friendly, containing non-toxic and non-expensive elements, and it offers good thermal stability, three important requirements for use in large scale application such as electric vehicles.

The actual capacity obtained electrochemically from $LiFePO_4$ is highly dependent on its synthesis method. The most common synthetic methods are: solid state, hydrothermal and sol-gel [2, 5-6]. Solid state syntheses use high temperature, typically greater that 600 °C, while the sol-gel method is time consuming with costly precursors. The hydrothermal synthesis requires relatively low reaction time and temperatures [6-7]. Wittingham first described the hydrothermal synthesis of $LiFePO_4$ in 2001 [6]. In a typical procedure, a solution containing $FeSO_4$, LiOH and $H_3PO_4$ is heated in an auto-clave under hydrothermal conditions at temperatures greater than 120 °C for several hours. The isolation of the product from solution showed the formation of $LiFePO_4$. After this first report numerous publications have demonstrated the successful synthesis of $LiFePO_4$ using different precursors and reaction conditions [7-10].

The hydrothermal preparation of $LiFePO_4$ using LiOH, $FeSO_4$ and $H_3PO_4$ can lead to the formation of $Fe^{3+}$ impurities in the final product. These impurities lower the capacity of the electrode. In addition, the synthesis uses the costly LiOH in excess as lithium precursor. The development of a synthetic process that overcomes these problems has inspired numerous researches. Recently, Recham *et al.* [11] proposed a synthesis using "latent bases" to precipitate $LiFePO_4$ under hydrothermal conditions. These bases raise the pH of the solution, which is required for the precipitation $LiFePO_4$, upon decomposition during the hydrothermal synthesis. Another major issue with the use of $LiFePO_4$ as a cathode material is its low bulk electronic conductivity.

Today, the most common method to increase the electronic conductivity of $LiFePO_4$ is to form a surface coating of carbon on the $LiFePO_4$ particles. This procedure was first described by Ravet *et al.* [10], where the addition of a carbon source during synthesis increased the conductivity of $LiFePO_4$. Irrespective of the method used to coat the $LiFePO_4$ particles, an adequate conductive coating was only obtained under heating the material to temperatures near 700 °C.

This chapter reports on the hydrothermal synthesis of $LiFePO_4$, concentrating on the use of a new iron precursor and the thermal decomposition of urea, as described in chapter 3. The thermal decomposition of urea (occurring at temperatures higher than 90 °C) initiates the precipitation of $LiFePO_4$ from a reaction between $LiH_2PO_4$ and $FeSO_4$. Hydrothermal and micro-wave assisted hydrothermal conditions were used to achieve the necessary temperature for the thermal decomposition of urea. Motivated by the idea of forming a carbon coating without the addition of an external carbon source, iron gluconate ($(OHCH_2[CH(OH)]_4CO_2)_2Fe.2H_2O$) was used to replace $FeSO_4$ as the iron/carbon precursor.

## *5.2 Results*

### 5.2.1 Hydrothermal synthesis of $LiFePO_4$ – as described in the literature

In figure 5.1, we can see the XRD diffraction pattern of phase pure $LiFePO_4$ synthesized following the hydrothermal procedure described previously in the literature [6]. The method consists of dissolving $FeSO_4$, LiOH and $H_3PO_4$ precursors in water with the addition of ascorbic acid as reducing agent. After mixing, there is the formation of a grayish gel, which is then transferred to the auto-clave and heated to 180 °C for 5 hours. The diffraction pattern of this sample is shown in Figure 5.1, and can be indexed on an orthorhombic olivine-type structure with the *Pnma* space group.

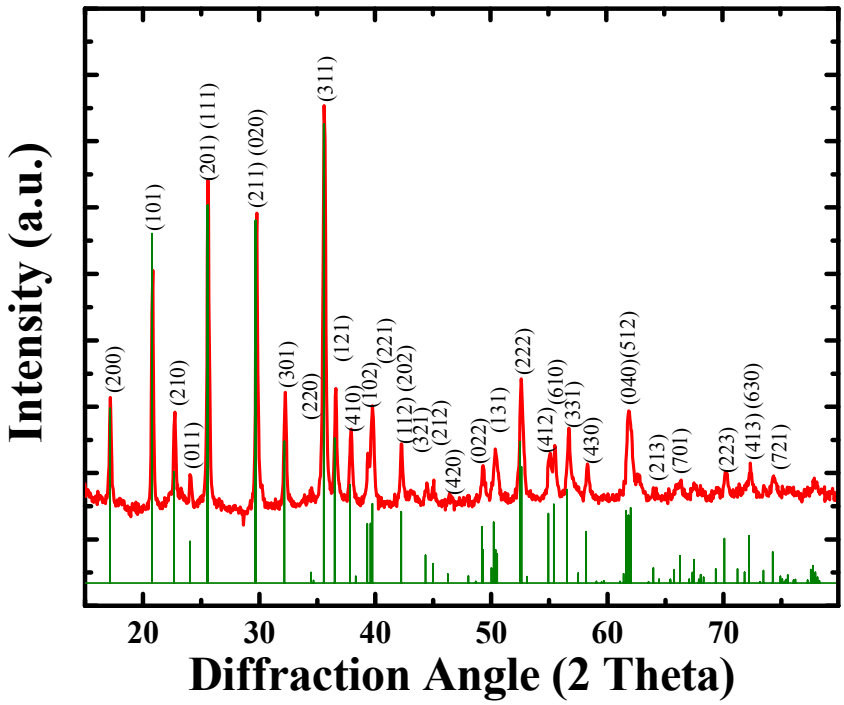


***Figure 5.1:*** *XRD profile of $LiFePO_4$ synthesized by the traditional hydrothermal method (red) and the green lines indicate the reference spectra of $LiFePO_4$.*

### 5.2.2 Hydrothermal synthesis of $LiFePO_4$ – assisted by the thermal decomposition of urea

As mentioned in chapter 4, urea decomposes at temperatures greater than 90 °C yielding $NH_3$, increasing the pH of the solution, and in the presence of $LiH_2PO_4$ and an iron source, it allows the precipitation of $LiFePO_4$,

$$LiH_2PO_4 + FeSO_4 + NH_2CONH_2 + H_2O \rightarrow LiFePO_4 + (NH_4)_2SO_4 + CO_2 .$$

The XRD diffraction pattern of our initial trial using the urea produced a pure olivine crystalline phase (blue line in Figure 5.2), similar to the diffraction pattern obtained using the procedure from the literature (Figure 5.1). The urea synthesis was also performed using the micro-wave assisted hydrothermal technique, which permits a synthesis in a significantly lower amount of time (black line in Figure 5.2). During our investigation, we determined that a reaction time of only 15 minutes was required to produce a phase pure sample of $LiFePO_4$ at 180 °C.

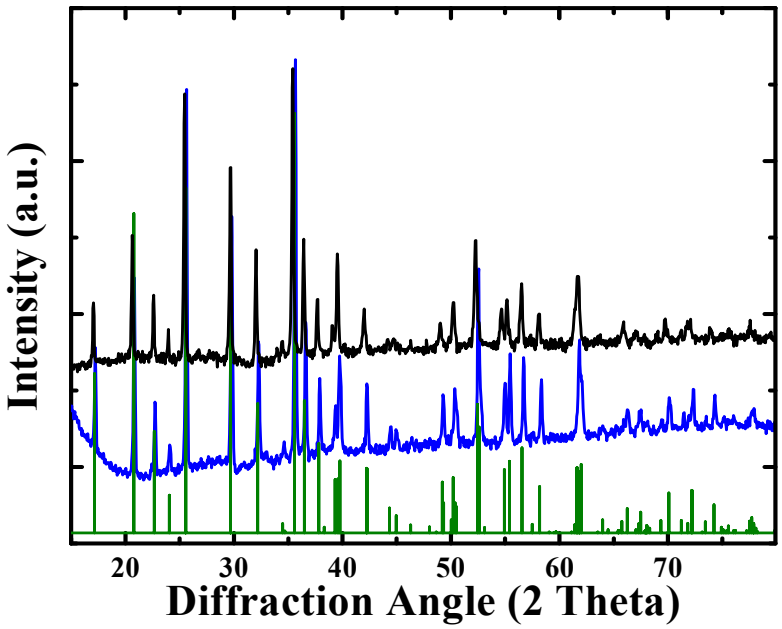


***Figure 5.2:*** *XRD profile of $LiFePO_4$ synthesized under hydrothermal conditions using the thermal decomposition of urea (blue), under micro-wave assisted hydrothermal condition (black) with the green lines indicating the reference spectra of $LiFePO_4$.*

The particle size and morphology of the $LiFePO_4$ obtained was determined by SEM. Figure 5.3 shows the SEM images of the sample prepared with $LiH_2PO_4$ and $FeSO_4$ in a hydrothermal synthesis. As we can see in Figure 5.3, a broad particle size distribution was obtained. The morphology can be described by ~ 10 μm well formed diamond shaped primary particles and larger secondary particles ~ 50 μm in diameter composed of an agglomeration of the primary particles. The image shown in Figure 5.3 represents the general morphology of the sample obtained from the urea reaction. This morphology is consisted even under lower magnifications of the SEM (100 μm).

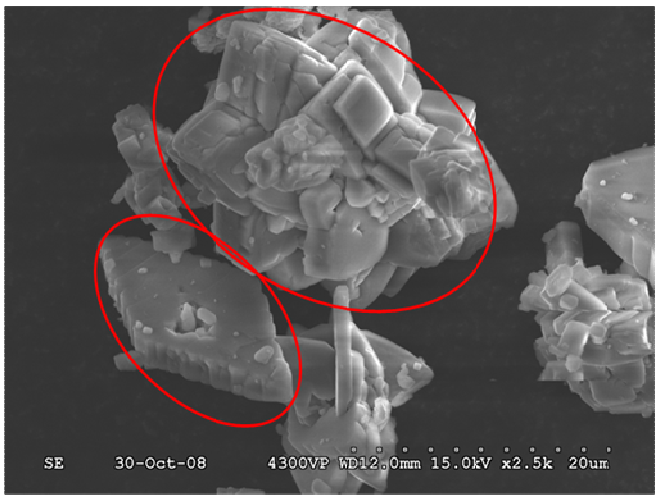


***Figure 5.3:*** *SEM images of $LiFePO_4$ synthesized using the thermal decomposition of urea under hydrothermal conditions.*

To enhance the electronic conductivity and consequently the electrochemical performance of the material, a carbon coating was subsequently placed on all samples before being tested as cathodes in electrochemical cells.

The $LiFePO_4$ was coated with a thin layer of carbon (~ 2 weight %) and could then be tested for electrochemical properties.

### 5.2.3 "*in situ*" carbon coating attempt

The carbon coating is generally achieved by heating $LiFePO_4$ with an external carbon source at temperatures higher than 700 °C. An "*in situ*" carbon coating procedure during the hydrothermal synthesis, if possible, would eliminate the use of a subsequent heating step. This would represent a significant saving in energy costs as well as synthetic complexity. Iron gluconate ($(OHCH_2[CH(OH)]_4CO_2)_2Fe.2H_2O$) was investigated as the iron source for the synthesis of $LiFePO_4$. The use of a molecule that contains carbon within its structure, such as gluconate, could be very interesting for the synthesis of $LiFePO_4$ since this structural carbon could be used as the material to provide the carbon coating. This would eliminate the need for a second subsequent reaction to deposit carbon which would represent a significant technical achievement. The idea here was to try to form the carbon coating directly from the carbon atoms present in iron gluconate molecule while avoiding the use of an external compound as carbon source. A XRD diffraction pattern from the product obtained using iron gluconate as a precursor is shown in Figure 5.4. This diffraction profile demonstrates the successful synthesis of $LiFePO_4$ as the sample can be indexed on the olivine structure.

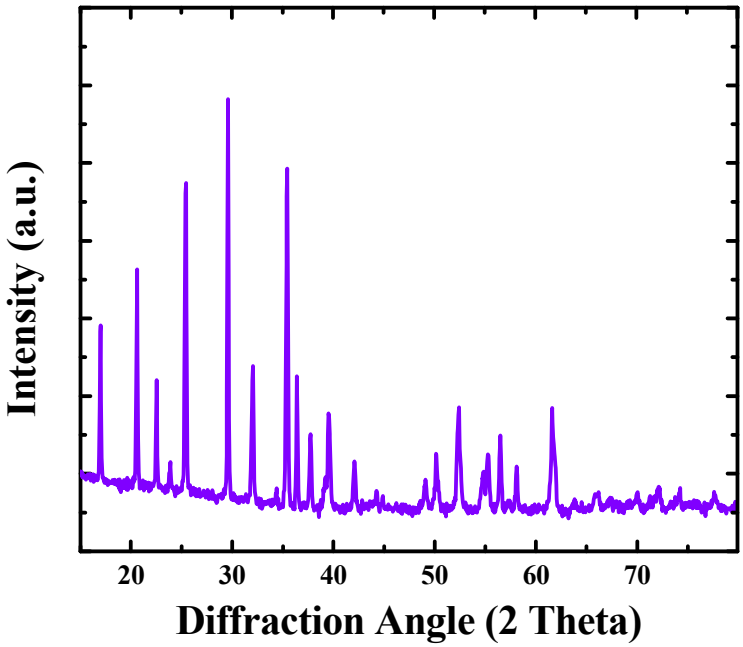


***Figure 5.4:*** *XRD profile of $LiFePO_4$ synthesized using the thermal decomposition of urea and iron gluconate as precursor.*

After isolation the product consisted of two distinct colors, the main sample was green and several well-distributed black spots could be easily identified around the sample. Figure 5.5 shows SEM images of both the green and the black areas of sample. Clearly, the green precipitate sample is composed of cubic particles about 5 μm in diameter, while the black sample is formed of smaller circular particles, roughly 2 μm in diameter.

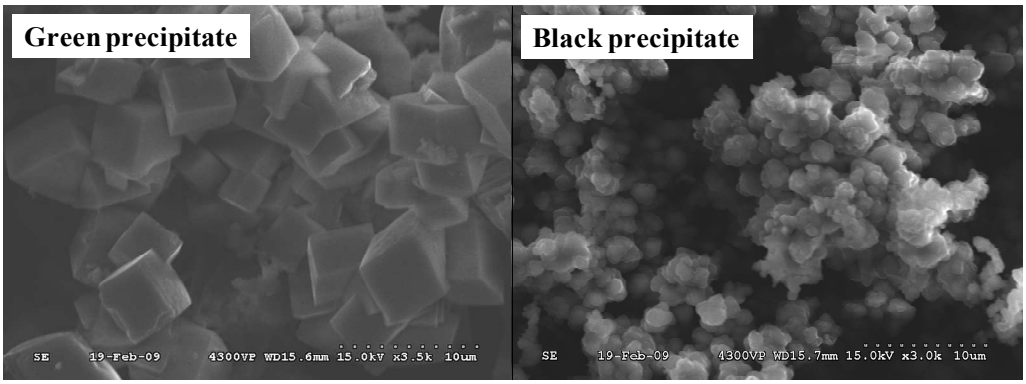


***Figure 5.5:*** *SEM images of $LiFePO_4$ synthesized with iron gluconate. The black precipitate (a) and green precipitate (b).*

Energy Dispersive X-ray micro analyses (EDX) were performed to identify the composition of both precipitates. Table 5.1 shows the elemental composition of each part of the precipitate (green and black). Clearly, the black sample is composed of a higher amount of carbon (~ 41%) while the green sample is formed only of ~ 10% carbon. The result indicates that carbon appears to agglomerate together during synthesis. As we can see in Table 5.1, a significant amount of oxygen, phosphorous and iron were also detected in the black sample. Two hypotheses can explain the presence of these species: some decomposition of the formed $LiFePO_4$ or its precursors during the hydrothermal synthesis; while the second possibility could be due to the difficulty in separating both green and black precipitate during EDX analysis. The separation of each part within the sample was a delicate operation and it is likely that both parts, green and black, are contaminated with the other. More experiments are necessary to further develop the synthesis using iron gluconate to provide a successful surface coating of carbon on $LiFePO_4$.

***Table 5.1:*** *EDX quantitative elemental analyses of both, black and green precipitates obtained during the synthesis of $LiFePO_4$ using iron gluconate precursor.*

| Sample | Element | (%) |
|---|---|---|
| **Green** | C | 10 |
| | O | 46 |
| | P | 18 |
| | Fe | 26 |
| **Black** | C | 41 |
| | O | 20 |
| | P | 09 |
| | Fe | 31 |

### 5.2.4 Electrochemical Analyses of $LiFePO_4$

The electrochemical properties of the as-synthesized $LiFePO_4$ within a lithium-ion battery were tested as described in the experimental section (chapter 2). The analyses were performed by charging and discharging the cell between 2.2 and 4.0 V using a current rate of 14 mA $g^{-1}$. The current rate is determined considering the amount of electrochemical active material in the tested electrode (here the active material is $LiFePO_4$). In theory the cell should perform a complete cycle of charge and discharge in about 24 hours within this current rate. Samples prepared with iron gluconate precursor with the goal of an "*in situ*" carbon coating present an enhanced carbon amount in the final product.

After elemental analysis we observed ~ 25 weight % of carbon. To these materials, the electrochemical tests were performed with a current rate determined considering the carbon amount as a non-active material as this would significantly affect the reported capacity values

As can be seen in Figure 5.6, the measured capacity of this sample was about 110 mAh $g^{-1}$ (65% of the theoretical capacity of $LiFePO_4$) and the complete cycle of charge and discharge was done in ~ 16 hours. Similar capacity values were obtained from material synthesized using $FeSO_4$ as precursor, in spite of the fact that these samples were identified *via* XRD to be very pure. Numerous synthetic experiments and analyses were performed in order to understand the source of the low capacity for this material. Unfortunately, we were not able to determine the reason for the low electrochemical performance of our samples.

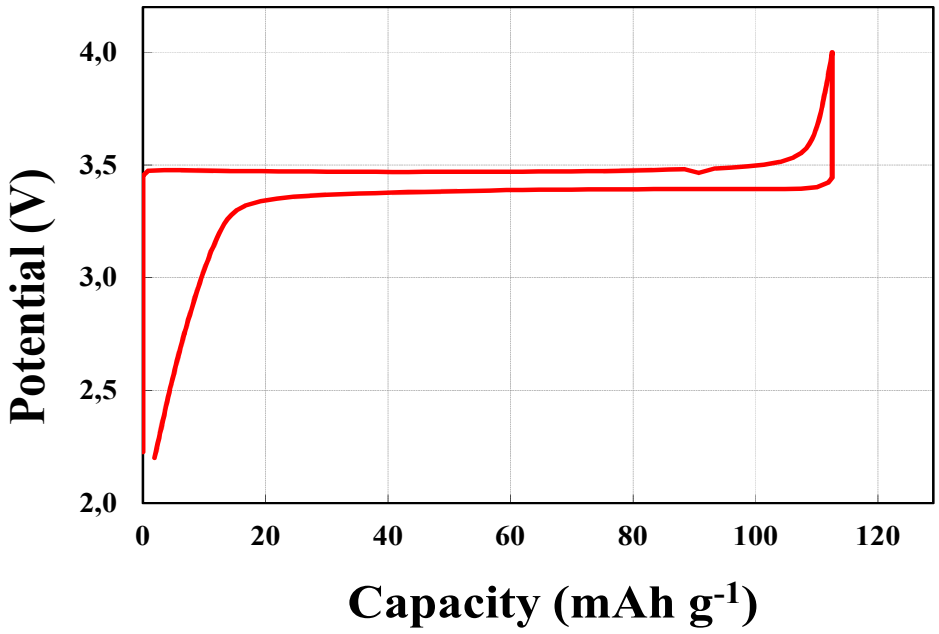


***Figure 5.6:*** *Measured capacity of $LiFePO_4$ synthesized using the thermal decomposition of urea, and iron gluconate.*

## *5.3 Conclusion*

We have demonstrated in this chapter the synthesis of $LiFePO_4$ using the thermal decomposition of urea to initiate its formation at elevated temperature. We have also reported on the use of an interesting precursor for iron in $LiFePO_4$ that attempted to form an "*in situ*" carbon coating. In spite of the fact that our samples present a good purity and acceptable particle size, we were not able to obtain adequate electrochemical performances. Unfortunately as we were performing our investigation, Recham *et al*. [11] reported on the use of "latent bases" for the preparation of $LiFePO_4$. The bases used in that study decompose gradually with an increase in the temperature of the solution. They studied several latent bases for the synthesis of $LiFePO_4$, including urea. They reported an electrochemical capacity near to 160 mAh $g^{-1}$. We immediately started to try and duplicate their results such that we could identify the reasons to the low capacities obtained *via* our synthesis. Unfortunately, with the procedure provided in their article and conference presentations we were not able to reproduce their results. At that time we decided to pursue a different avenue for the synthesis of electrode materials using the thermal decomposition of urea and this work formed the basis of chapter 4.

## *5.4 References:*


**1.** Padhi, A. K.; Nanjundaswamy, K. S.; Goodenough, J. B. *J. Electrochem. Soc.* **1997**, 144, 1188.

**2.** Yamada, A.; Chung, S. C.; Hinokuma, K. *J. Electrochem. Soc.* **2001**,148, A224.

**3.** Zaghib, K.; Striebel, K.; Guerfi, A.; Shim, J.; Armand, M.; Gauthier, M. *Electrochim. Acta* **2004**, 50, 263.

**4.** Yang, J.; Xu, J. J. *Electrochem. Solid-State Lett.* **2004**, 7, A515.

**5.** Yang, S.; Zavalij, P. Y.; Whitthingham, M. S. *Electrochem. Commun.* **2001**, 3, 505.

**6.** Franger, S.; Le Cras, F.; Bourbon, C.; Rouault, H. *J. Power Sources* **2003**, 119–121, 252.

**7.** Chen, J.; Wang, S.; Whittingham, M. S. *J. Power Sources* **2007,** 174, 442.

**8.** Ellis, B.; Wang, H. K.; Makahnouk, W. R. M.; Nazar, L. F. *J. Mater. Chem.* **2007**, 17, 3248.

**9.** Wang, Z. *J. f Power Sources* **2008**, 184, 633.

**10.** Ravet, N.; Chouinard, Y.; Magnan, J.-F.; Besner, S.; Gauthier, M.; Armand, M. *J. Power Sources* **2001**, 97-98, 503.

**11.** Recham, N.; Armand, M.; Laffont, L.; Tarascon, J.-M. *Electrochem. Solid-State Lett.* **2009**, 12, A-39.

**12.** Murugan, V.; Muraliganth, T.; Manthiram, A. *J. Electrochem. Soc.* **2009**, 156, A79.

# Chapter 6

# Conclusion and Perspectives

## *6.1 Conclusion*

The synthesis and treatment of cathode materials for lithium-ion batteries were investigated in this master's thesis. The thermal decomposition of urea was used for the synthesis of precursors to lithium mixed metal oxides ($LiNi_xMn_xCo_{(1-2x)}O_2$) and to the synthesis of $LiFePO_4$. Novel post-synthetic treatments were also developed with the goal to increase the particle size of hydroxides. Both materials studied here, $LiNi_xMn_xCo_{(1-2x)}O_2$ and $LiFePO_4$, have been widely considered for the commercial replacement of $LiCoO_2$ as cathode materials in lithium-ion batteries[1-3].

In Chapter 3 of this master's thesis we demonstrated two different post-synthetic treatments on $Ni_xMn_xCo_{(1-2x)}(OH)_2$. Both hydrothermal and microwave assisted hydrothermal methods were used, with the goal of producing more dense hydroxides particle. Samples with a large range of stoichiometry ($x$ = 0.00 to 0.50) were synthesized and subjected to various treatments. These treatments were performed in solution right after the co-precipitation step and have been found to increase the crystallinity and particle size of the samples as compared to

the non-treated samples. A significant increase in particle size was obtained when the treatment time was extended to 24 hours. With this hydrothermal treatment we obtained particles with a much larger particle size than those obtained by treating dried powder as reported previously in the literature. Post-synthetic heat treatments of hydroxides have previously shown an increase in the particle size [4]. However, our procedure was the first time that a post-synthetic treatment on the hydroxide was performed in solution right after co-precipitation. The procedure that was proposed here eliminates the necessity of isolating the precipitate before the heat treatment. Another advantage of the hydrothermal and micro-wave hydrothermal techniques may be due to the combination of pressure and temperature, rather than temperature alone. It was also found that the hydroxides containing larger concentration of Ni and Mn demonstrated an increase in the amount of oxyhydroxide phase present within the sample compared to sample with lower Ni content. In addition the extent of oxidation to an oxyhydroxide phase increased with exposure time at high temperature (180 °C). For application within lithium-ion batteries, the mixed metal hydroxides were oxidized into electrochemically-active lithiated oxides ($LiNi_xMn_xCo_{(1-2x)}O_2$). Generally, both the capacity and capacity retention of these oxides were similar to those reported previously in the literature [5-6]. Interestingly, $LiCoO_2$ prepared from the treated $Co(OH)_2$ samples show improved capacity retention as compared to those prepared by traditional co-precipitation methods.

Secondly, in Chapter 4, we developed a novel co-precipitation approach to the preparation of mixed metal hydroxides. The approach was based on the thermal decomposition of urea under different heating conditions. Three different techniques were used to achieve the temperature required to decompose urea, which lead to the precipitation of the mixed metal hydroxide: 1) hydrothermal, 2) microwave assisted hydrothermal and 3) reflux. All samples prepared by these methods were then successfully used as precursors for the preparation of electrochemically active lithiated mixed metal oxides. The time at elevated temperature during the synthesis of the hydroxide had a significant impact on its crystalinity and morphology. Samples prepared using a traditional hydrothermal heat treatment showed larger particle size and greater crystallinity than those at lower temperature or time. The electrochemical properties of these resulting oxides presented characteristics similar those obtained in the literature [5-6].

Chapter 5 reports on the results obtained for the synthesis of $LiFePO_4$ using hydrothermal techniques. The novel approach was based on the thermal decomposition of urea to raise the pH of a hydrothermal reaction at elevated temperature. One of the areas that I investigated was the possibility of producing a carbon coating on the surface of LiFePO4 using iron gluconate as the iron source for the reaction. Iron gluconate contains carbon within its structure such that a carbon coated $LiFePO_4$ molecule may be possible without adding an external carbon source. Unfortunately, EDX analysis demonstrated that the experiments using iron gluconate resulted in a biphasic material. One phase was

primarily iron based, while the other phase was primarily carbon based. In the carbon phase we also detected some Fe, P and O that can suggest some residual $LiFePO_4$ or possibly some of the precursors from the hydrothermal synthesis. We obtained $LiFePO_4$ samples with good purity, *via* XRD, and acceptable particle sizes, but the electrochemical performance of these cathodes were poor. In 2009, before we were able to overcome the issues with our samples, Recham *et al.* [8] reported on the synthesis of $LiFePO_4$, using what they called "latent bases", or molecules that decompose gradually with the increase of the solution's temperature. Several bases were used, including urea. They showed cathode capacities near 160 mAh $g^{-1}$.

## *6.2 Perspectives*

The post-synthetic treatments performed to increase the particle size of the hydroxides showed promising results when we extended the reaction time to 24 hours under hydrothermal conditions. It would be valuable to pursue further the time variable to find the best conditions to obtain increased particle size.

The synthesis of hydroxides by the thermal decomposition of urea demonstrated in Chapter 4 needs improvement in terms of synthetic conditions. The method developed has several parameters that can be tuned to provide a route for the precipitation of denser hydroxides. Samples prepared in this work

showed a very interesting change in morphology when compared to the traditional co-precipitation. The particle size obtained with the hydrothermal technique was larger than previous reports. The concentration of precursors, pH of solution, time, temperature and pressure are some of the parameters that need to be studied more deeply to generate pure products with larger particle sizes.

It was previously demonstrated in the literature that the electrochemical performance of lithiated oxides is highly dependent on the precursor hydroxide's morphology and particle size [9]. Thus, it would be interesting to prepare electrochemical active lithiated oxides using as precursors, hydroxides obtained from both the post-synthetic treatment and synthesis based on the thermal decomposition of urea after the optimization of parameters to obtain larger particle size.

The formation of an "*in situ*" surface carbon coating for $LiFePO_4$ produced during a hydrothermal synthesis can save both energy and time. We have introduced the use of iron gluconate, which can be at the same time the iron source and the carbon source for $LiFePO_4$. As reported in Chapter 5, we have observed mainly the formation of two separated products, $LiFePO_4$ and carbon. Although we did not obtain a carbon coated $LiFePO_4$, carbon-containing precursors should continue to be studied with the goal of generating a carbon coated product *via* hydrothermal reactions.

## *6.3 References*


**1.** Amatucci, G. G.; Tarascon, J.-M.; Klein, L. C. *Solid State lonics* **1996,** 83, 167.

**2.** Numata, K.; Sakaki, C.; Yamanaka, S. *Chem. Lett.* **1997**, 26, 725.

**3.** Liu, Z.; Yu, A.; Lee, J. Y. *J Power Sources* **1999,** 81-82, 416.

**4.** Barkhouse, D. A. R.; Dahn, J. R. *J. Electrochem. Soc.* **2005**, 152, A746.

**5.** MacNeil, D. D.; Lu, Z.; Dahn, J. R. *J. Electrochem. Soc*. **2002**, 149, A1332.

**6.** Ohzuku, T.; Makimura, Y. *Chem. Lett.* **2001**, 30, 642.

**7.** Ravet, N.; Chouinard, Y.; Magnan, J.-F.; Besner, S.; Gauthier, M.; Armand, M. *J. Power Sources* **2001**, 97-98, 503.

**8.** Recham, N.; Armand, M.; Laffont, L.; Tarascon, J.-M. *Electrochem. Solid-State Lett.* **2009**, 12, A-39.

**9.** van Bommel. A.; Dahn, J. R. *J. Electrochem. Soc.* **2009**, 156, A362.

# Appendix

## *A. Rietveld analysis for $Ni_xMn_xCo_{(1-2x)}(OH)_2$ prepared by the traditional co-precipitation method and hydrothermal treated for 5 hours*

Figure A.1 shows the XRD pattern with the Rietveld structure refinement of a sample from the $Ni_xMn_xCo_{(1-2x)}(OH)_2$ series ($x$ = 0.00) prepared by the traditional co-precipitation after it was submitted to a hydrothermal post-synthetic treatment of 5 hours (reported on chapter 3). Careful analysis of the powder pattern revealed the presence of both a hydroxide phase and an oxyhydroxide phase. In Figure A.1 the small peak observed at ~ 35º is related to the development of the oxyhydroxide phase. Therefore a two crystalline phase Rietveld refinement was performed to determine the percentage of each phase within the sample. Table 3.1 provides the results of the refinement as well as the lattice parameters ($a$ and $c$) and the unit cell volume for samples submitted to the hydrothermal treatment of 5 hours from $x$ = 0.00 to 0.50.

The starting values for the atomic positions were those of the $Co(OH)_2$ structure, in space group P3m1 (N° 164) and the CoOOH structure, in the space

group $P6_3/mmc$ (N° 194). The Miller indexes (*hkl*) for he Bragg peaks of both structures $Co(OH)_2$ and CoOOH are listed in Table A.1. The Miller indexes are a three integers representation for the orientation of a specific atomic planes within the unit cell.

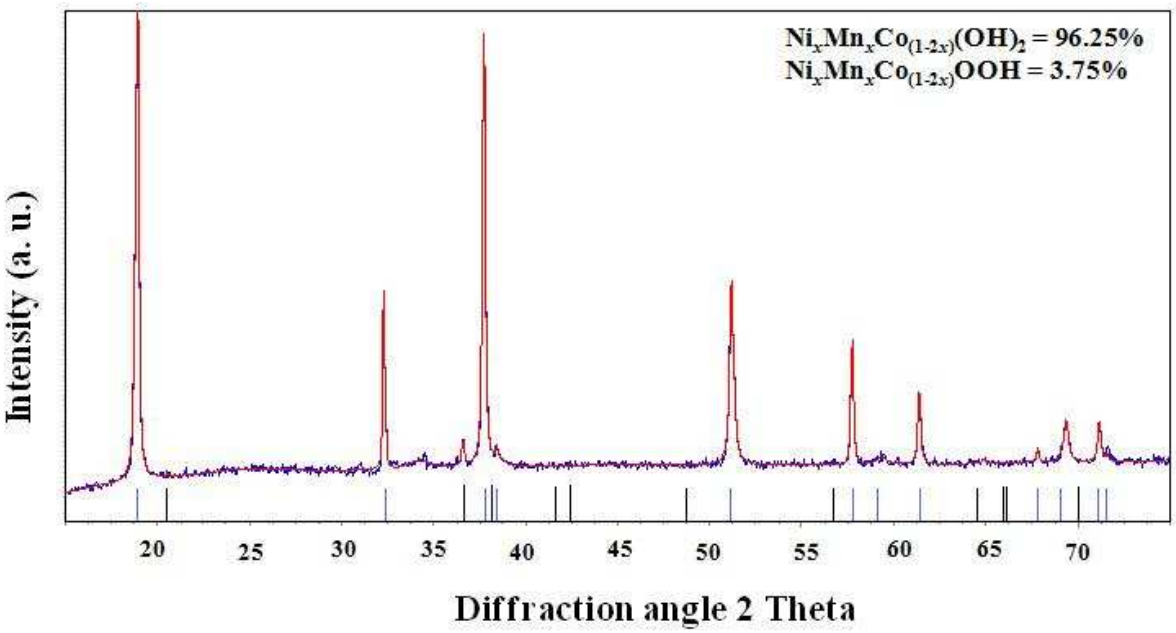


***Figure A.1:*** *Rietveld refinement for $Ni_xMn_xCo_{(1-2x)}(OH)_2$ (x =0.00) obtained after the hydrothermal post-synthetic treatment for 5 hours. Observed intensities: blue line; calculated intensities: red line; blue vertical bars: angular positions of Bragg reflections for $Co(OH)_2$; black vertical bars : angular positions of Bragg reflections for CoOOH.*

***Table A.1:*** *Miller indexes for Bragg peaks for $Co(OH)_2$ and CoOOH.*

| | **2 Theta** | ***h*** | ***k*** | ***l*** |
|---|---|---|---|---|
| $Co(OH)_2$ | 19.154 | 0 | 0 | 1 |
| | 33.019 | 1 | 0 | 0 |
| | 38.452 | 0 | 1 | 1 |
| | 38.871 | 0 | 0 | 2 |
| | 51.899 | 0 | 1 | 2 |
| | 58.971 | 1 | 1 | 0 |
| | 59.883 | 0 | 0 | 3 |
| | 62.606 | 1 | 1 | 1 |
| | 69.270 | 2 | 0 | 0 |
| | 70.108 | 1 | 0 | 3 |
| | 72.626 | 2 | 0 | 1 |
| | 72.900 | 1 | 1 | 2 |
| *CoOOH* | 28.379 | 1 | 1 | 0 |
| | 35.273 | 1 | 2 | 0 |
| | 44.768 | 1 | 3 | 0 |
| | 46.972 | 0 | 2 | 1 |
| | 48.607 | 0 | 4 | 0 |
| | 49.619 | 1 | 1 | 1 |
| | 52.803 | 2 | 0 | 0 |
| | 54.254 | 1 | 2 | 1 |
| | 55.851 | 1 | 4 | 0 |
| | 61.438 | 1 | 3 | 1 |
| | 68.184 | 1 | 5 | 0 |
| | 69.467 | 2 | 1 | 1 |
| | 73.336 | 2 | 2 | 1 |
| | 74.623 | 2 | 4 | 0 |
| | 79.554 | 2 | 3 | 1 |
| | 82.634 | 1 | 5 | 1 |
| | 85.954 | 0 | 0 | 2 |

## *B. Rietveld analysis for $LiNi_xMn_xCo_{(1-2x)}O_2$ prepared from hydroxides synthesized using the traditional co-precipitation reaction and post-synthetic treatments*

Figure A.2 shows the XRD pattern with the Rietveld structure refinement of a sample from the $LiNi_xMn_xCo_{(1-2x)}O_2$ series obtained from the traditional co-precipitation method after hydrothermal post-synthetic treatments for 5 hours ($x$ = 0.05) (reported on chapter 3). Table 3.2 provides the lattice parameters ($a$ and $c$) and unit cell volume of $LiNi_xMn_xCo_{(1-2x)}O_2$. All peaks are indexed on the $\alpha$-$NaFeO_2$ structure (space group $R\overline{3}m$, N°. 166) and Rietveld refinement was performed to all samples (all results are presented in chapter 3) using the same structure. The Miller indexes for Bragg peaks are listed in Table A.2.

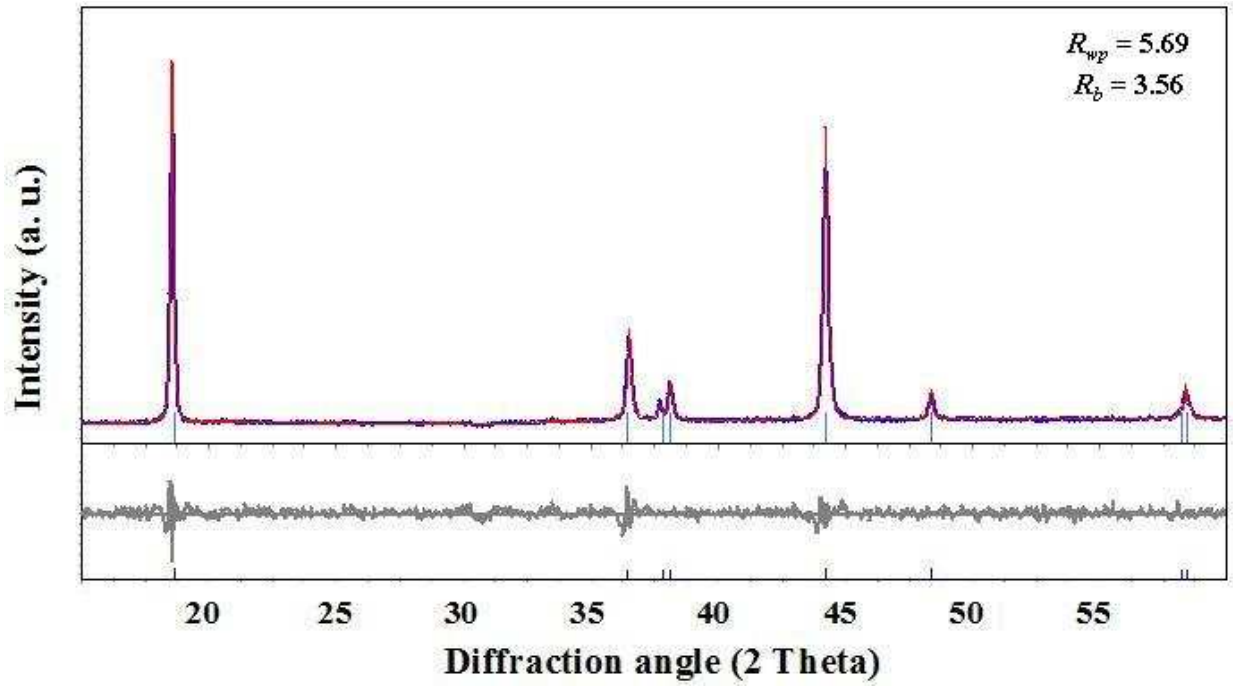


***Figure A.2:*** *Rietveld refinement plots for $LiNi_xMn_xCo_{(1-2x)}O_2$ (x = 0.30): blue line for observed reflections, red line for calculated reflections based on the $LiCoO_2$ structure, grey line is the difference between the observed and the calculated reflections, and blue vertical lines are the Bragg positions for reference $LiCoO_2$.*

***Table A.2:*** Miller indexes for Bragg peaks for $LiCoO_2$.

| **2 Theta** | ***h*** | ***k*** | ***l*** |
|---|---|---|---|
| 19.157 | 0 | 0 | 3 |
| 37.003 | 1 | 0 | 1 |
| 38.876 | 0 | 0 | 6 |
| 39.015 | 0 | 1 | 2 |
| 45.320 | 1 | 0 | 4 |
| 49.626 | 0 | 1 | 5 |
| 59.993 | 1 | 0 | 7 |

## *C. Rietveld analysis for $LiNi_xMn_xCo_{(1-2x)}O_2$ prepared from the hydroxide synthesized using the thermal decomposition of urea*

Figure A.3 shows the XRD pattern with the Rietveld structure refinement of a sample from the $LiNi_xMn_xCo_{(1-2x)}O_2$ series ($x$ = 0.05) obtained from the hydroxides synthesized using the thermal decomposition of urea (reported in chapter 4). Table 4.2 provides the lattice parameters ($a$ and $c$) and unit cell volume of $LiNi_xMn_xCo_{(1-2x)}O_2$. All peaks are indexed on the $\alpha$-$NaFeO_2$ structure (space group $R\bar{3}m$, N°. 166) and a Rietveld refinement was performed on all samples (presented in chapter 4) using the same structure. The Miller indexes for Bragg peaks are listed in Table A.2 of the appendix B.

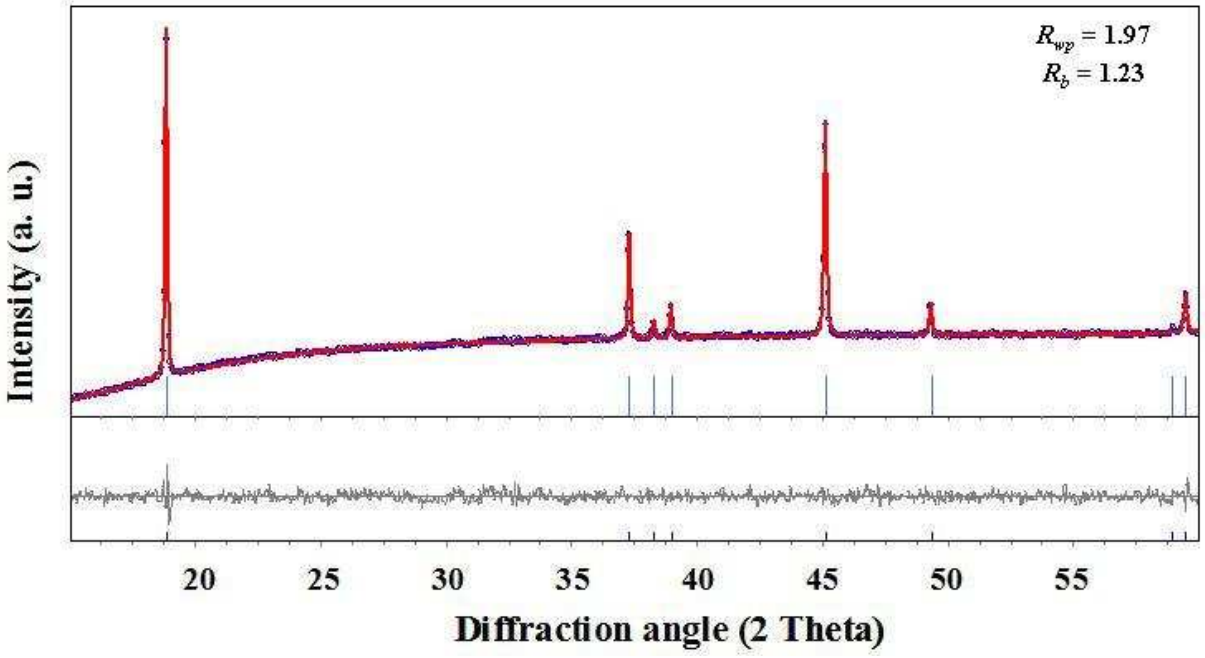


***Figure A.3:*** *Rietveld refinement plots for $LiNi_xMn_xCo_{(1-2x)}O_2$ (x = 0.05): blue line for observed reflections, red line for calculated reflections based on the $LiCoO_2$ structure, grey line is the difference between the observed and the calculated reflections, and blue vertical lines are the Bragg positions).*